Colloidal Lanthanide-Based Nanoparticles; From Single Nanoparticle Analysis to New Applications in Lasing and Cancer Therapy

by

Stephanie Bonvicini
B.Sc., University of Calgary, 2013

A Thesis Submitted in Partial Fulfillment
of the Requirements for the Degree of

MASTER OF SCIENCE

in the Department of Chemistry

Supervisory Committee

Colloidal Lanthanide-Based Nanoparticles; From Single Nanoparticle Analysis to New Applications in Lasing and Cancer Therapy

by

Stephanie Bonvicini
B.Sc., University of Calgary, 2013

Supervisory Committee

Dr. ir. Franciscus C. J. M. van Veggel (Department of Chemistry)
Supervisor

Dr. Thomas M. Fyles (Department of Chemistry)
Departmental Member

Dr. Dennis K. Hore (Department of Chemistry)
Departmental Member

Abstract

Supervisory Committee
Dr. ir. Franciscus C. J. M. van Veggel (Department of Chemistry)
Supervisor
Dr. Thomas M. Fyles (Department of Chemistry)
Departmental Member
Dr. Dennis K. Hore (Department of Chemistry)
Departmental Member

Lanthanide-based nanoparticles can be used in a variety of applications, including biomedical work such as imaging and cancer therapies, and in solar cells. This thesis presents two different potential applications for lanthanide-based nanoparticles and a possible new method for single nanoparticle analysis. Each of the projects presented in this thesis starts from the colloidal synthesis of the nanoparticles and then explores their varying properties, such as size and size distribution, crystallinity, elemental composition, and optical properties.

Chapter 1 presents a short introduction to lanthanides and explores their ability to luminesce and upconvert. These optical properties make lanthanide-based nanoparticles attractive in both the visible and near-infrared (NIR) range. Chapter 2 explores the possibility of using β-LaF_3:Nd^{3+} (5%) nanoparticles in a colloidal laser to overcome some issues that solid state lasers face due to thermal effects. A colloidal laser requires small nanoparticles that can emit a useful wavelength and that are dispersed in a high boiling point liquid. In Chapter 3, a cation exchange of ytterbium for yttrium and erbium in water-dispersible β-$NaYF_4$:Er^{3+} nanoparticles across a polyvinylpyrrolidone (PVP) surface coating was tested as a possible synthesis route for radioactive nanoparticles. Incorporating radioactive materials at the end of a therapy preparation would limit the number of synthesis steps in an isotope laboratory. Chapter 4 presents single-particle

analysis of β-$NaYF_4$:Er^{3+} (50%) nanoparticles using X-ray absorption spectroscopy (XAS) at the Canadian Light Source (CLS). Electron beams in scanning electron transmission microscopes (STEM) can damage the samples, making quantification of nanoparticles challenging. Finally, Chapter 5 discusses some conclusions and suggests possible future work.

Table of Contents

List of Tables

List of Figures

List of Abbreviations

CLS	Canadian Light Source
CD	compact disk
CN	coordination number
DMDCS	dimethyldichlorosilane
DMSO	dimethyl sulfoxide
DVD	digital versatile disc/digital video disc
DI	deionized
EDX (EDS)	energy-dispersive X-ray spectroscopy
EELS	electron energy loss spectroscopy
ESA	excited state absorption
EXAFS	extended X-ray absorption fine structure
FESEM	field emission scanning electron microscope
FWHM	full width at half maximum
GSA	ground state absorption
HAADF	high-angle annular dark-field
HDPE	high-density polyethylene
HDR	high dose radiation
HPLC	high-performance liquid chromatography
ICP-MS	inductively coupled plasma mass spectrometry
JCPDS	Joint Committee on Powder Diffraction Standards
LASER	light amplification by stimulated emission of radiation

LDR	low dose radiation
MRI	magnetic resonance imaging
MWCO	molecular weight cut-off
NEXAFS	near-edge X-ray absorption fine structure
NIR	near-infrared
OD	optical density
PMT	photomultiplier tube
PVP	polyvinylpyrrolidone
SD	standard deviation
SM	spectromicroscopy
SMA connectorized	subminiature version A connectorized
SPECT	single-photon emission computed tomography
STEHM	scanning transmission electron holography microscopy
STEM	scanning transmission electron microscopy
STXM	scanning transmission X-ray microscopy
TEM	transmission electron microscopy
UV	ultraviolet
Vis	visible
XANES	X-ray absorption near-edge structure
XAS	X-ray absorption spectroscopy
XRD	X-ray diffraction
YAG	yttrium aluminium garnet

Acknowledgements

I would like to thank my supervisor, Dr. ir. Frank C. J. M. van Veggel, for all of his guidance and support throughout my time at the University of Victoria.

I would also like to thank my committee members, Dr. Tom Fyles and Dr. Dennis Hore. I would also like to thank Dr. Patrick Nahirney for acting as my external committee member and for the generous access to his TEM.

Thank you to our collaborators, Chana Goren from the SRQ in Israel and Jay Dynes from the Canadian Light Source in Saskatoon.

I would like to thank the members of the van Veggel group, both past and present, for teaching me the details of the syntheses and for all of the help through the lab work and for making my time here so enjoyable.

I would like to thank Dr. Jody Spence for his wonderful work with the ICP-MS analysis. Thank you also to Dr. Elaine Humphrey for her help with the STEHM and to Dr. Stefano Rubino for his discussion about single-particle elemental analysis.

I also would like to thank Andrew Macdonald for all of his help fixing everything that went wrong with the fluorimeter.

Thank you to the staff from Science Stores, the chemistry administrative staff, and to everyone else that helped me during my time here.

Thank you all very much!

Dedication

To my wonderful family
for all their love and continued support
♥

Chapter 1: General Introduction

1.1. A brief overview of lanthanides

When we look at the periodic table, we see two groups of elements, the lanthanides and the actinides, that have been separated out from the main table due to spacing issues and gives us the distinctive appearance that we know and love. The first row of these lonely elements, ranging from lanthanum to lutetium, makes up the lanthanides. In 1787, Lieutenant C. A. Arrhenius first discovered a black mineral specimen which was later named "Gadolinite".[1] This turned out to be a mixture of several lanthanides. Much effort was put into trying to separate these elements, however, it was not until after the Second World War that the problems involved in purifying the lanthanides were resolved.[2]

The lanthanides are hard to separate from each other because of their similar chemical properties.[2] The 4*f* orbitals of the lanthanides, ranging from not filled to partially and completely filled, are shielded from the nucleus by the filled 5*s* and 5*p* orbitals. The overlap of the 5*s* and 5*p* orbitals into the 4*f* orbitals leads to a decrease in the atomic and ionic radii from lanthanum across to lutetium. This is known as the lanthanide contraction.[3]

Yttrium is often considered to be part of the lanthanide series because of its chemical similarities. The ionic radius of yttrium places it between erbium and holmium (**Table 1.1**).[4]

Although the lanthanides are often referred to as "rare earth" elements, this is a misnomer. The lanthanides are as abundant in the Earth's crust as many more common

elements.[1] In the past they were ultimately considered rare because of how hard they were to isolate and purify. They are also not "earths", as this is an archaic term for the modern "oxides".[1]

Table 1.1—Ionic radii and electron configurations of the trivalent lanthanide cations when the coordination number is 8.[4] Elements important to this thesis have been bolded.

Element	Symbol	Atomic number	Ionic radius (Å) CN=8	Ln^{3+} electron configuration
Lanthanum	**La**	**57**	**1.18**	**[Xe]4*f*^{0}**
Cerium	Ce	58	1.14	[Xe]4*f*^{1}
Praseodymium	Pr	59	1.14	[Xe]4*f*^{2}
Neodymium	**Nd**	**60**	**1.12**	**[Xe]4*f*^{3}**
Promethium	Pm	61	1.10	[Xe]4*f*^{4}
Samarium	Sm	62	1.09	[Xe]4*f*^{5}
Europium	Eu	63	1.07	[Xe]4*f*^{6}
Gadolinium	Gd	64	1.06	[Xe]4*f*^{7}
Terbium	Tb	65	1.04	[Xe]4*f*^{8}
Dysprosium	Dy	66	1.03	[Xe]4*f*^{9}
Holmium	Ho	67	1.02	[Xe]4*f*^{10}
Yttrium	**Y**	**39**	**1.015**	**[Kr]**
Erbium	**Er**	**68**	**1.00**	**[Xe]4*f*^{11}**
Thulium	Tm	69	0.99	[Xe]4*f*^{12}
Ytterbium	**Yb**	**70**	**0.98**	**[Xe]4*f*^{13}**
Lutetium	Lu	71	0.97	[Xe]4*f*^{14}

The lanthanides can be found all around us in modern society. Lanthanides are used everywhere from hard magnets to flat screen televisions,[5] and from contrast enhancement agents in magnetic resonance imaging (MRI) to catalysis in refineries.[6]

Most of the lanthanides can typically be found in the 3+ oxidation state. With the exception for La^{3+} which has empty 4*f* orbitals and Lu^{3+} which has full 4*f* orbitals, all of the lanthanides have unpaired 4*f* electrons. These 4*f* energy levels can be seen in **Figure 1.1**.[7] Although *f-f* transitions are Laporte-forbidden,[8] *f-d* transitions are not. Mixing the forbidden *f-f* transitions with allowed *f-d* transitions allows for lanthanide ion

luminescence. This is beneficial because, when compared with organic molecules, there are no bonds that can be broken which would lead to a loss of luminescence. This loss is called photobleaching and it often hampers the use of organic dyes in many applications.[9]

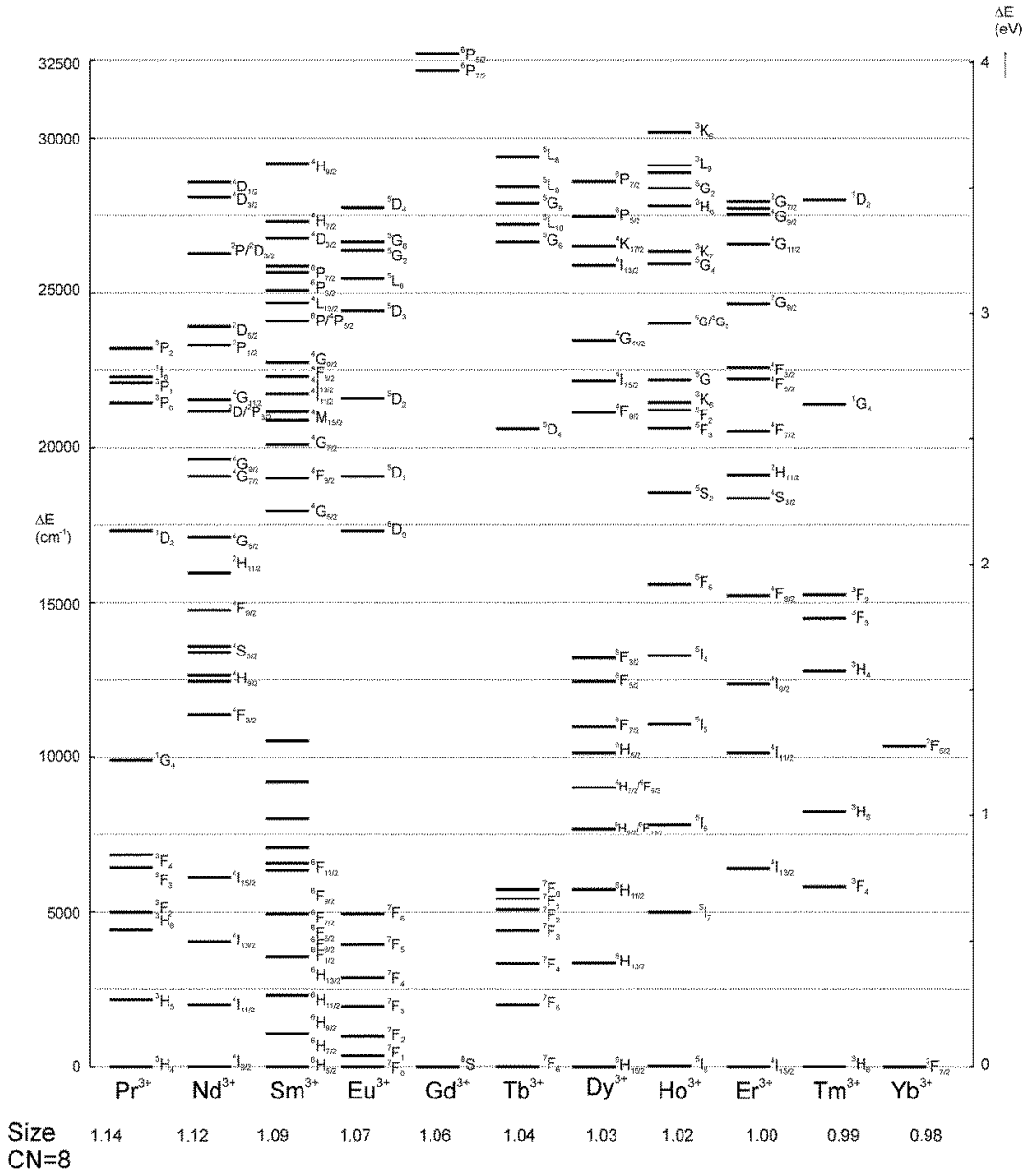

Figure 1.1—4*f* energy levels and sizes of trivalent lanthanide ion in aqueous solution.[7] La^{3+} and Lu^{3+} were excluded from this figure as they have empty and full 4*f* orbitals, respectively. Ce^{3+} was excluded as the presence of only one valence electron and one excited state very close to the ground state limits its optical usefulness.

Once an electron is excited within the 4*f* orbitals, its decay to the ground state is very slow because of the forbidden *f-f* transitions. This results in long lifetimes, often as long as tens of milliseconds.[10] This is much longer than the lifetimes observed for organic molecules and semiconductors, which are often at the nanosecond timescale. As the decay from the excited state to the ground state is forbidden, the reverse process of being excited from the ground state to the excited state and the excited state absorption process are also forbidden. This means that the extinction coefficients for absorption are very small. The lanthanides have extinction coefficients that can be up to 10 M^{-1} cm^{-1}, which is quite low when compared to the 100,000 M^{-1} cm^{-1} extinction coefficients for some organic dyes.[11]

The luminescence of lanthanides can be exploited to make materials that emit in specific ranges, simply by adjusting the concentration of lanthanides in a material. For example, the neodymium-doped yttrium aluminium garnet (Nd:YAG) rod is a very common solid state lasing material that emits at a wavelength of 1064 nm. Typically, only 1.0% of the yttrium in the YAG crystal is substituted with neodymium cations,[12] but this small amount of neodymium is enough to create an efficient lasing material that is one of the most common solid state lasing mediums today.[13]

It is possible to dope small amounts of different lanthanides into a lattice already containing lanthanides because of their similar sizes. The $NaLnF_4$ lattice, where Ln represents any lanthanide, is quite flexible in terms of exchanging one lanthanide for another. This doping can lead to upconversion or simply to "regular" emission, and can be carried out during the initial synthesis of the nanoparticles. Nanoparticles can also be doped after they have been formed through the use of a cation exchange process,[14] or the

cation exchange method can be used to grow lanthanide shells onto the surface of already formed nanoparticles.[15] Shells can also be added by adding small amounts of the desired shell material onto pre-grown cores. Depending on which lanthanides are used for the shell and for the original nanoparticles, the lattice can experience either compressive or tensile strain, thereby affecting the growth of subsequent shells.[16]

Another reason that lanthanide emission is of interest is that lanthanides can participate in a process called upconversion. Upconversion is a non-linear multiphoton absorption process where an excitation wavelength with a longer wavelength (lower energy) leads to the emission of a photon with a shorter wavelength (higher energy). This is the opposite of regular luminescence, where the excitation wavelength with a shorter wavelength (higher energy) leads to the emission of a photon with a longer wavelength (lower energy). In upconversion of lanthanide-based (nano)materials, this multiphoton absorption is generally a multi-step process. Upconversion is similar to two-photon absorption followed by luminescence, but this process requires high photon fluxes because the two excitation photons have to arrive basically at the same time. It should be noted that upconversion differs from second harmonic generation, where photons with the same frequency are combined to generate new photons with half the wavelength and twice the frequency of the initial photons. The mechanisms of upconversion in lanthanides will be discussed in detail in Chapter 3.

Regardless of whether lanthanide nanoparticles upconvert or exhibit regular luminescence, it is necessary to quantify the composition of the nanoparticles, specifically the concentrations of (different) dopant ions in the host material. This quantification is important because changing the amount of a dopant ion can alter the

amount of emission or upconversion by the nanoparticles. Many techniques exist for characterizing ensembles of nanoparticles, such as inductively coupled plasma mass spectrometry (ICP-MS), electron energy-loss spectroscopy (EELS), and energy-dispersive X-ray spectroscopy (EDX).[17] The latter two techniques are often performed in a scanning transmission electron microscopy (STEM) and can give single-particle analysis as well as ensemble measurements.

1.2. An overview of nanoparticles

Nanoparticles are small particles that are typically between 1-100 nm,[18] and are of interest because their properties (optical, electrical, physical, magnetic, etc.) are typically vastly different from those of the bulk material.[19]

Nanoparticles of an almost endless variety can now be synthesized in the laboratory.[20] However, humans have been interacting with nanoparticles long before they were even called "nanoparticles". Some nanoparticles, such as iron oxyhydrides and aluminosilicates, are produced naturally through volcano eruptions, wildfires, and weathering of bulk materials.[21] Podoconiosis, a disease producing lymphedema, and endemic Kaposi sarcoma, a cancer of the blood and lymph nodes, are both a result of nanoparticles from volcanic ash being absorbed through the skin.[21c] The use of nanoparticles by humans is not new either. While the existence of nanoparticles was unknown, nanoparticles were actually used to colour ceramics as early as the 9th century[21a] and different sizes of silver and gold nanoparticles were used to create beautiful stained glass masterpieces.[21a, 22]

The beginnings of modern colloidal chemistry can be traced back to 1857, when Michael Faraday prepared gold nanoparticles by reacting an aqueous solution of gold salt

with an organic phosphorus solution.[23] From there, much work was done with respect to synthesizing metal and semi-conducting nanoparticles to exploit their specific properties. In the 1980s, colloidal cadmium sulfide, a semi-conductor with photocatalytic properties, was one of the first materials to be studied systematically.[24] It was found that the electronic and optical properties of metal and semiconducting nanoparticles had very different properties than those of the bulk,[25] and that those properties were very much dependent on the size and shape of the nanoparticles.[26] In order to optimize the properties of these nanoparticles, their size and shape must be controlled.

Lanthanide-based nanoparticles are especially interesting because their optical properties depend less on size and shape and more on the dopant ion concentrations and the host material.[27] Therefore, their properties can be quite similar to their bulk phase properties. However, as the size of the nanoparticles decreases, structure disordering within the host material lattice and surface defects begin to have a bigger influence over the properties. In order to maintain reproducibility, it is still important to have good control over the size and shape of the nanoparticles.

$NaLnF_4$ nanoparticles come in two different lattice phases. At room temperature and standard pressure, the cubic (α) phase is the kinetically stable product, while the hexagonal (β) phase is the thermodynamically stable product. The hexagonal phase has been found to be the best host for upconversion thus far.[28] One of the first colloidal syntheses to produce monodisperse β-$NaLnF_4$ (Ln=Pr to Lu, Y) nanoparticles was presented in 2006 by Yan *et al*.[29] and monodisperse α-$NaYF_4$:Er^{3+}/Yb^{3+} and α-$NaYF_4$:Tm^{3+}/Yb^{3+} nanoparticles were made using colloidal synthesis in 2007 by Capobianco *et al*.[30]

Bare nanoparticles, that is nanoparticles with no surface coating, typically do not disperse well in solvents unless they are charge stabilized. Therefore, nanoparticles are coated with a well-chosen ligand in order to allow their dispersability in a desired solvent. The standard synthesis of the nanoparticles that are the focus of this thesis yield nanoparticles that can be represented by the cartoon seen in **Figure 1.2**. The purple sphere represents the $NaLnF_4$ or LnF_3 core. The orange spheres with squiggly tails represent the ligand on the surface of the nanoparticles. It is necessary to keep in mind that this representation is only a simple cartoon.

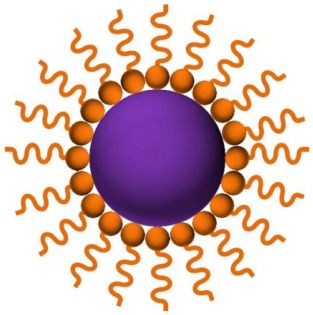

Figure 1.2—Cartoon depiction of the lanthanide-based nanoparticles featured in this thesis. The purple sphere represents the $NaLnF_4$ or LnF_3 core and the orange spheres with squiggly tails represent the surface ligand that coats the nanoparticles.

1.3. Summary of each chapter

The goal of this thesis is to highlight the versatility of these lanthanide-based nanoparticles by demonstrating their potential in a variety of applications.

Current solid state lasers suffer from overheating due to thermal effects. The cooling of a solid lasing source provides significant challenges, and alternative lasing set ups are being explored. In Chapter 2, the possibility of lanthanum fluoride nanoparticles doped with neodymium for eventual use in a nanoparticle dispersion laser is explored. Ideally, a colloidal laser would have very small nanoparticles dispersed in a high boiling point liquid that emit at a wavelength used by solid state lasers. This emission would be long-

lived enough to create a population inversion. Neodymium is an appropriate choice for these nanoparticles as it emits at 1064 nm which is the same as that used by many solid state lasers. The small nanoparticles are necessary to avoid scattering the emitted photons that would be used as the lasing source and a high boiling point liquid would allow for the dissipation of heat from the excited nanoparticles without evaporating the solution which could forfeit the stability of the liquid lasing material. It was found that 5 nm diameter β-LaF_3:Nd^{3+} (5%) nanoparticles dispersed in 1-octadecene exhibit lifetimes of approximately 96 μs, making them a suitable candidate for use in a colloidal laser.

In Chapter 3, a potential synthesis route for radioactive nanoparticles for use as a potential radiative cancer therapy was investigated by testing whether a cation exchange of ytterbium for yttrium and erbium in water-dispersible β-$NaYF_4$:Er^{3+} nanoparticles across a polyvinylpyrrolidone (PVP) surface coating was possible. The use of ytterbium and erbium is purely to act as a possible optical confirmation of whether the cation exchange took place. After performing the cation exchange process, it has been determined that the exchange of ytterbium for yttrium and erbium across a PVP surface coating is possible.

Finally, Chapter 4 presents the use of X-ray Absorption Spectroscopy (XAS) for single-particle analysis of the quantification of erbium in $NaYF_4$:Er^{3+} (50%) nanoparticles. As electron beams tend to cause beam damage over time, a new technique that is highly sensitive and can be used for single nanoparticles is needed. Nanoparticles that were larger than the best resolution of the XAS beam were made and were sent to the

Canadian Light Source (CLS) in Saskatoon. Preliminary data strongly suggest that single nanoparticle elemental analysis is possible.

Chapter 5 discusses the conclusions of each project and mentions some possible future directions.

Chapter 2: Nd^{3+}-doped Nanoparticles for Use in a Nanoparticle Dispersion Laser

2.1. Introduction

2.1.1. Laser background

Light Amplification by Stimulated Emission of Radiation (LASER) is commonly used in laboratories for many types of measurements and is also used for many applications in society, such as laser work in industrial settings,[31] medical procedures,[32] and in common technologies such as in CD and DVD players.[31] Lasers function by using stimulated emission.[32] Stimulated emission occurs when an incident photon of the right energy interacts with an excited species, forcing the latter to undergo a radiative decay. This interaction creates a "copy" photon that has the same phase, frequency, polarization, and direction as the incident photon and hence the signal is amplified. If this process occurs over and over, an avalanche of excited photons could occur. This would result in a very intense light source, assuming there are more species in the lasing excited state than there are in the lower lasing level (e.g. the ground state).

In order for a laser to lase successfully, a population inversion needs to be established. A population inversion occurs when there is a build-up of excited states with more species in the excited state than in a lower energy state, often the ground state. If these electrons in the excited state are stimulated by a photon with the same energy as that of the energy gap between the ground and excited state, they can transition from the excited state to a lower energy state and emit a "copy" photon that has the same direction, phase, frequency, and polarization. This leads to an amplification of the signal and results in a more powerful laser beam. Without this inversion, there is more absorption than there is stimulated emission which thus does not lead to lasing.

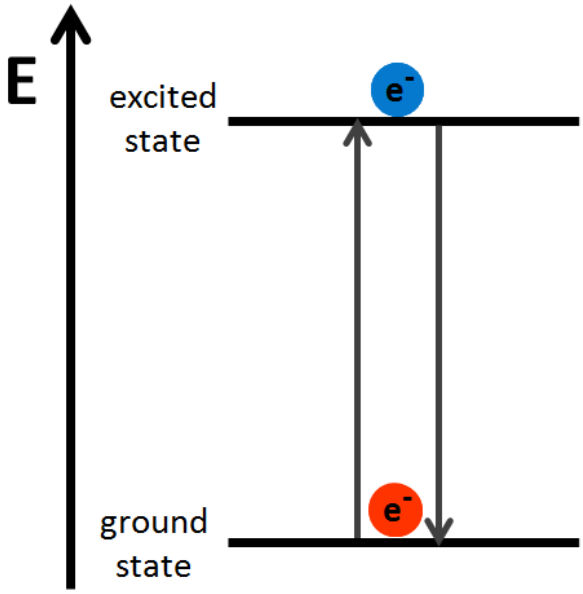

Figure 2.1—Two-level system.

In a 2-level system (**Figure 2.1**), electrons in the ground state are promoted to an excited state with a certain wavelength that matches the difference in energy, ΔE, between the ground state and the excited state (**Equation 2.1**)

$$\Delta E = h\nu \qquad \textbf{Equation 2.1}$$

where h is Plank's constant and ν is the frequency of the incident/emitted photon. From here, the electron in the excited state can follow one of three paths. The first path is spontaneous emission, where the electron spontaneously decays to the ground state, typically after 10^{-8} seconds,[33] and emits a photon in a random direction. The second path would be for the electron in the excited state to undergo non-radiative decay. In the third path, the electron in the excited state could also interact with an incident photon with the right energy to create a "copy" photon. This latter process is called stimulated emission. Once the electron has been promoted to the excited state, the probability that an incident photon of the right energy will interact with the electron in the excited state to give

stimulated emission is the exact same as the probability that the incident photon of the right energy will be absorbed by an electron in the ground state.[33] Therefore, the electrons are basically returning to the ground state via stimulated emission as fast as they can be excited out of the ground state, making a population inversion impossible. Hence, a true two-level laser does not exist.

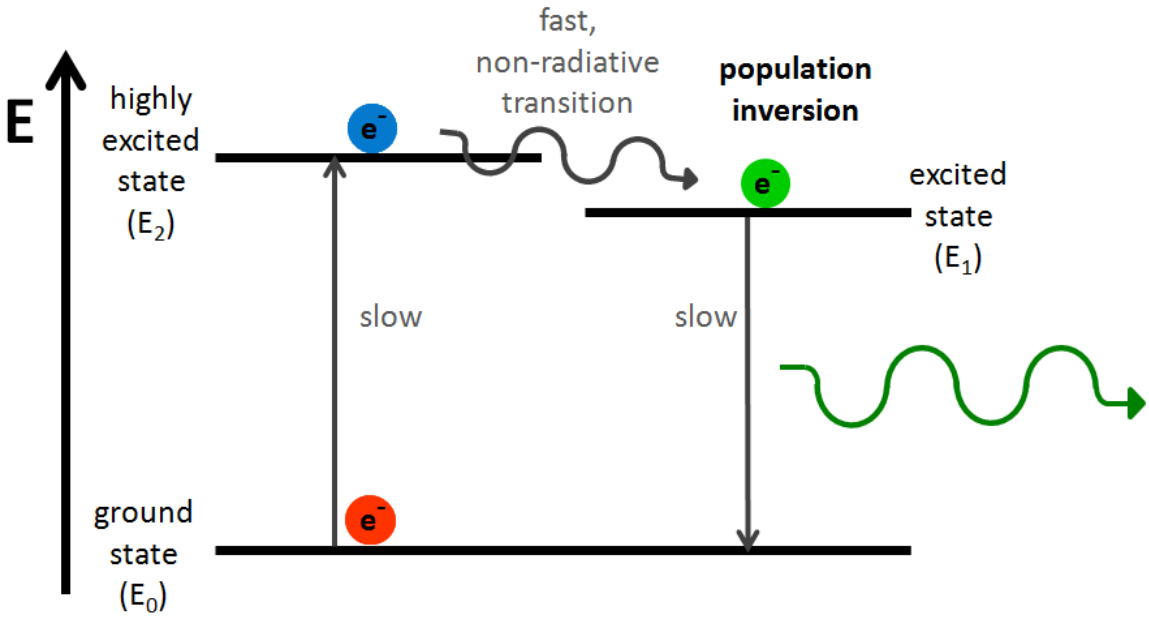

Figure 2.2—Three-level laser.

In order to create a population inversion, there needs to be at least three energy levels. (**Figure 2.2**). In this case, electrons in the ground state (E_0) are pumped up to an excited state (E_2), where they undergo a very fast, non-radiative transition to an excited state (E_1). This excited state (E_1) is much longer lived than the highly excited state (E_2). If the material is pumped sufficiently hard, there will be a build-up of these excited states (E_1) with respect to the ground state (E_0), creating a population inversion. Electrons in the excited state (E_1) can then undergo spontaneous emission to the ground state (E_0), and this transition is the lasing transition. The photon that is emitted can interact with other

electrons in the excited state (E_1) to create the "copy" photons which allows for signal amplification, and lasing is achieved.

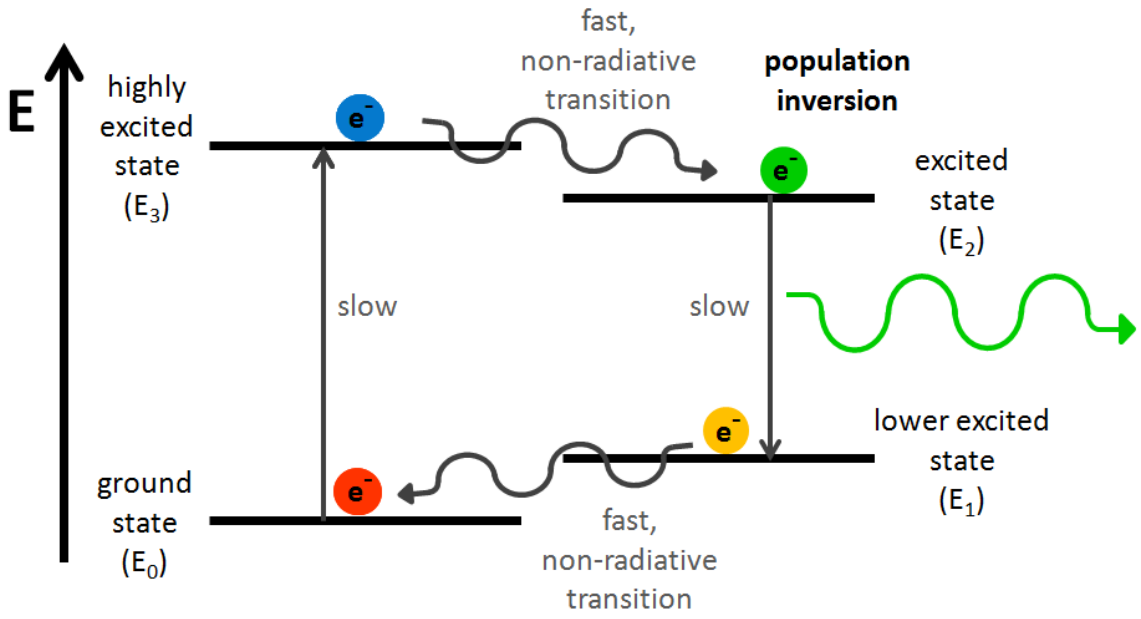

Figure 2.3—Four-level laser.

4-level lasers (**Figure 2.3**) can achieve a population inversion more easily than the previously-mentioned 3-level lasers. Electrons in the ground state (E_0) are excited up to a highly excited state (E_3) with the appropriate wavelength. As in the case of the 3-level laser, there is then a fast, non-radiative transition from the highly excited state (E_3) to a long-lived excited state (E_2). However, instead of decaying directly to the ground state (E_0), the lasing transition occurs as electrons in the excited state (E_2) decay radiatively to a lower excited state (E_1). From there, the electrons then undergo a fast, non-radiative transition back to the ground state (E_0), thus depopulating the lower lasing level (E_1) which would prevent the absorption of the laser light if this non-radiative rate is fast enough. This leads to a population inversion in the excited state (E_2) with respect to the lower excited state (E_1). While there will almost always be some electrons in the ground

state (E_0) of a 3-level laser, there are virtually no electrons in the lower excited state (E_1) of a 4-level laser. As a result, a population inversion is much more easily achieved in a 4-level laser. The photon that is emitted from the excited state (E_2) to the lower excited state (E_1) transition can interact with other electrons in the excited state to create the "copy" photons that allow for signal amplification. This amplification is further augmented by the optical cavity of the laser. This cavity is a chamber with a mirror at each end, which allows the "copy" photons to reflect back and forth until they escape; either through a small opening in one of the mirrors or through a mirror with a reflection efficiency that is just below 100%, thereby forming the laser beam.

2.1.2. Dispersion lasers

Thermal effects are a major concern for solid state lasers. When the lasing material in a solid state laser is pumped, a significant amount of the pump power is turned into heat inside the lasing material.[34] Traditionally, neodymium-doped yttrium aluminium garnet (Nd:YAG) lasers are pumped with white flashlights. This heat may distribute unevenly over the length of the lasing material, leading to uneven heating and therefore thermal stress along the boundaries of the hotter and cooler areas. This stress can cause the refractive index of the material to change and can lead to different focal lengths for the radial and tangential polarization which results in birefringence. It could also be possible for this heating to change the Boltzmann distribution of the lasing material, thereby changing the lasing frequency. These thermal effects can be very difficult, if not impossible, to correct for.

Considering the troubles that thermal effects cause in solid state lasers, it is surprising that not very much work has been done with respect to creating a colloidal laser. Many

different nanoparticles, such as β-LaF_3 doped with erbium, neodymium, and holmium,[35] CaF_2 doped with ytterbium and erbium,[36] and LaOF doped with europium,[37] have been synthesized and their photoluminescent properties have been characterized for possible use in a colloidal laser.

The increase in optical power resulting from the process by which lasing material transfers its energy into emission is called the optical gain. The optical gain coefficient can be defined as the increase in energy in a beam of light per unit of distance travelled.[38] Some work has been done in measuring optical gain coefficients for colloidal solutions of erbium and ytterbium.[39] Optimizing the optical gain coefficient could improve the efficiency of the laser by providing the most powerful laser beam possible for the material.

Tzuk *et al*. first demonstrated a nanoparticle dispersion laser in 2012.[40] By comparing the photoluminescent properties of a solution of pre-purchased Nd_2O_3 nanoparticles modified with dimethyldichlorosilane (DMDCS) dispersed in dimethyl sulfoxide (DMSO) to those of a neodymium-doped phosphate glass disk with approximately half the concentration of neodymium cations, it was found that the performance of the two lasers was similar. Earlier this year, the same group presented the first flashlamp-pumped nanoparticle dispersion laser,[41] again using Nd_2O_3 nanoparticles dispersed in DMSO. The group reported a lifetime of 16.6 μs for the Nd_2O_3 nanoparticles dispersed in deuterated DMSO with a molecular sieve added to absorb any water. While their results are promising, longer lifetimes that are closer to those of their solid state counterparts are required to make these colloidal lasers competitive.

2.1.3. Project goals

In order to achieve a suitable material for a liquid lasing medium, several requirements must be met. First, the nanoparticles need to be small enough to avoid scattering the laser beam that is being created. Ideally, the nanoparticles should be 5 nm in diameter or less. Next, the nanoparticles should emit a wavelength that is preferably one that is currently used in solid state lasers. The Nd:YAG rod emits at a wavelength of 1064 nm and is the most widely used solid state lasing medium that is lanthanide-doped.[13] Therefore, the nanoparticles would need to have enough neodymium to emit an intense beam of the desired 1064 nm wavelength. However, it is important to note that if too much neodymium is loaded into the nanoparticles, they could self-quench their photoluminescence through a cross-relaxation process, thereby decreasing the efficiency of the laser (**Figure 2.4**)[10]. An excited neodymium cation in the $^4F_{3/2}$ excited state (**Figure 2.4**, cation A) can transfer its energy to a nearby neodymium cation in the $^4I_{9/2}$ ground state (**Figure 2.4**, cation B), which will then be promoted to the upper Stark level of the $^4I_{11/2}$ state.[42] The Stark levels seen in **Figure 2.4** are a result of the splitting of the spectral lines seen in **Figure 1.1** due to the presence of an external electric field.

Since the nanoparticles need to be very small, it was suggested by our collaborator that doping the β-LaF_3:Nd^{3+} nanoparticles with 5 at% neodymium would result in an appropriate balance between too much and too little neodymium. In order to be competitive with solid state lasers using a neodymium source, such as a Nd:YAG rod, and to have an efficient laser beam, the emission lifetime of the nanoparticles would need to be greater than 100 μs. The Nd:YAG rod has a radiative lifetime of 240 ±10 μs.[13] A lifetime of about 100 μs would be long enough to establish a population inversion. As this lifetime of the emitting neodymium ions would be longer than the pulse rate of the

pumping laser, there would be a continuous stream of emission, thereby creating a stable, lasting laser beam. Additionally, the nanoparticles need to be dispersed in a liquid with a high boiling point. This is important because as the lasing medium heats up, it should not evaporate before it can be cooled down again as this could lead to more severe measurement problems than those experienced by solid state lasers. Finally, the concentration of the nanoparticle solution should be close to 5 wt% to achieve similar concentrations of neodymium ions as in solid state lasers.

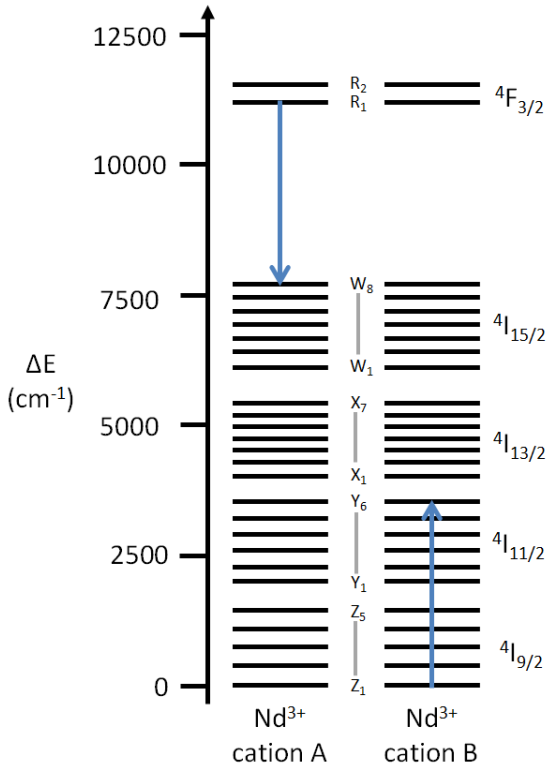

Figure 2.4—Schematic of photoluminescence self-quenching via cross-relaxation between two neodymium ions, labeled A and B.[42]

2.2. Results and Discussion

2.2.1. Synthesis of oleate-stabilized β-LaF_3:Nd^{3+} (5%) nanoparticles

β-LaF_3:Nd^{3+} (5%) nanoparticles were synthesized by dissolving lanthanum and neodymium chloride salts in a mixture of oleic acid and 1-octadecene.[43] This solution was then mixed with a solution of sodium hydroxide and ammonium fluoride in methanol and was then heated with a heating mantle to 300 °C for 1 h. The resulting nanoparticles were dispersed in hexanes and can be seen in **Figure 2.5**.

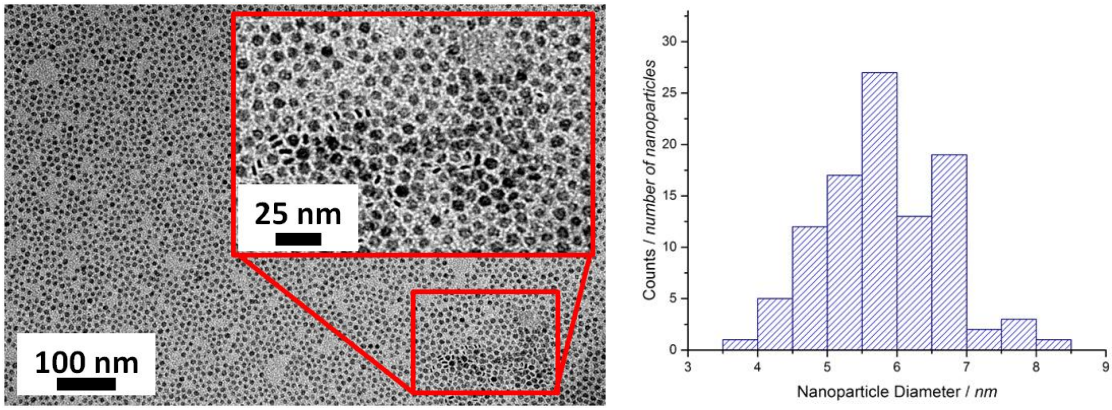

Figure 2.5—TEM image of β-LaF_3:Nd^{3+} (5%) nanoparticles dispersed in hexanes **(left)** with inset. The size distribution **(right)** shows that nanoparticles are ~5-6 nm in diameter, excluding nanoparticles stacked on their sides.

The size distribution is quite narrow with nanoparticles measuring 5.8 nm in diameter on average and a standard deviation of 0.9 nm. From the inset in **Figure 2.5** and from results presented in Chapter 4 of this thesis, it can be seen that the nanoparticles are actually plates instead of spheres. These nanoparticles are ~1 nm thick and show stacking on their sides. The stacking pattern that appears here is characteristic of plates, and their presence can be further confirmed by examining the X-ray diffraction (**Figure 2.6**) of the sample.

The nanoparticles were also analyzed using powder X-ray diffraction (**Figure 2.6**). The close matching of the reference peaks (JCPDS #00-032-0483 for bulk β-LaF_3) with the sample peaks confirms that β-LaF_3 was made. The sample peaks have been broadened due to the small size of the nanoparticles. This is expected when the Scherrer equation is considered (**Equation 2.2**)

$$\varepsilon = \frac{K\lambda}{b\cos\theta} \qquad \textbf{Equation 2.2}$$

where $\boldsymbol{\varepsilon}$ is the crystallite size, K is the shape factor, λ is the wavelength of the X-ray, b is the full width of the line broadening of the peak at half of the maximum intensity (FWHM) in radians, and θ is the Bragg angle.[44] While the actual value of ***K*** varies slightly from spheres to cubes and so on, this value is always close to unity.[44] As can be seen, as the size of the nanoparticles decreases, the width of the peaks will increase.

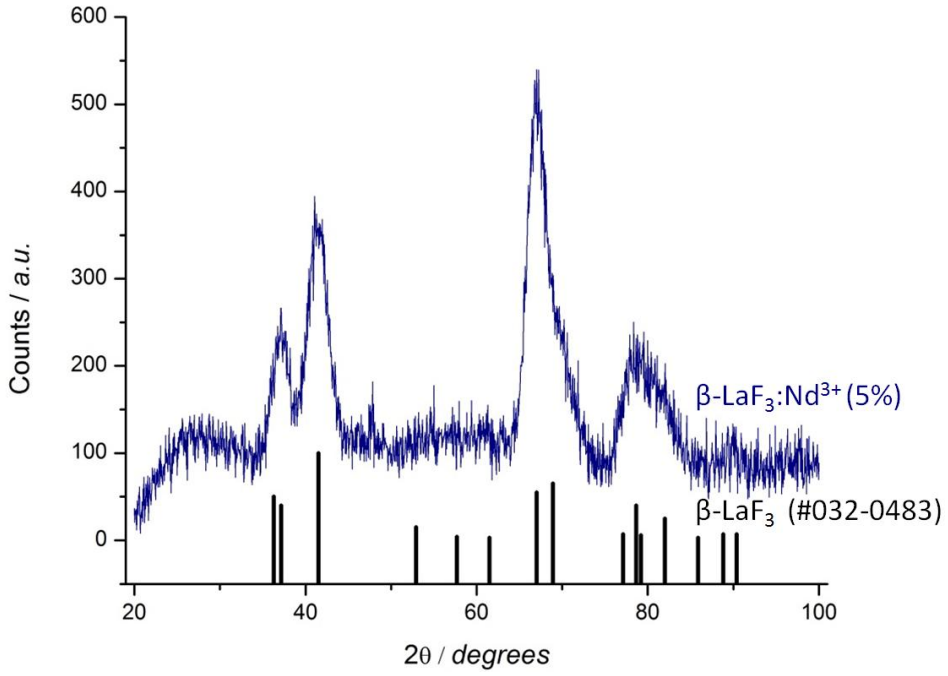

Figure 2.6—XRD of β-LaF_3:Nd^{3+} (5%) nanoparticles with reference β-LaF_3 (reference #00-032-0483).

The average size of the nanoparticles can also be determined from the X-ray diffraction data by measuring the FWHM of a Gaussian fit of the peaks and then using this value in the Scherrer equation (**Table 2.1**).

Table 2.1—Calculated nanoparticle sizes using the Scherrer equation (**Equation 2.2**), where λ = 0.22890 nm and taking the shape factor, K, to be 0.89.[44]

2*θ* (°)	**b** (°)	**ε** (nm)
37.11	2.20	5.59
41.46	2.88	4.32
67.34	3.57	3.91
79.50	4.64	3.25

The values in **Table 2.1** are in good agreement with those measured in the TEM. It appears that the peaks at approximately 67 °and 79 ° are slightly broader than those at 37 °and 42 °, which could support the presence of plate-like nanoparticles. However, **Equation 2.2** can be rearranged to calculate peak width (**Equation 2.3**).

$$b = \frac{K\lambda}{\varepsilon cos\theta} \qquad \textbf{Equation 2.3}$$

It can be seen that as 2θ increases, cosθ decreases. This alone results in an increase in the broadness of the peaks. It is therefore necessary to confirm that the observed broadening is actually due to different dimensions of the nanoparticles and not simply because of higher 2θ values. By comparing the theoretical line width for nanoparticles of a fixed size, in this case ε = 5 nm can be compared to the measured width to determine the cause of the broader peaks (**Table 2.2**).

Table 2.2—Comparison of the calculated width for 5 nm nanoparticles to the measured width, where λ = 0.22890 nm and taking the shape factor, K, to be 0.89.

2*θ* (°)	**ε** (nm)	**Theoretical b** (°)	**Measured b** (°)
37.11	5	2.46	2.20
41.46	5	2.49	2.88
67.34	5	2.80	3.57
79.50	5	3.02	4.64

The theoretical and measured peak widths for the peaks at 37.11 ° and 41.46 ° are quite close. However, the theoretical widths for the peaks at 67.34 ° and 79.50 ° are quite different from the measured widths. Therefore, the broadening of these two peaks is due to the presence of plate-like nanoparticles, and not simply due to higher 2*θ* values.

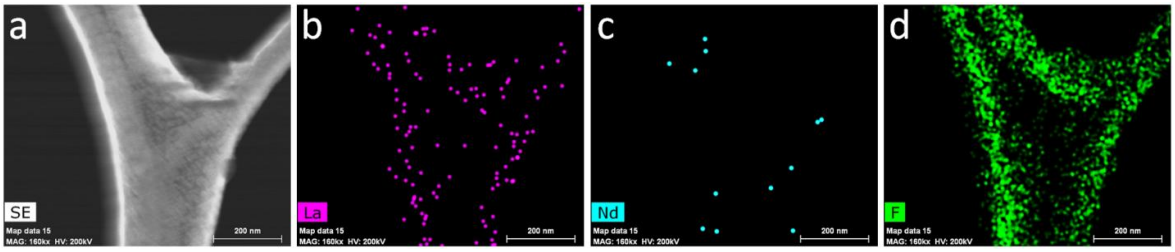

Figure 2.7—a) STEHM image of β-LaF_3:Nd^{3+} (5%) nanoparticles dispersed in hexanes on a lacey carbon grid with an accelerating voltage of 200 kV, an electromagnetic current of 3 μA, and measured in scanning transmission electron microscopy (STEM) mode. **b-d)** Elemental mapping of lanthanum **(b)**, neodymium **(c)**, and fluorine **(d)**. It is important to note that the pixels do not represent individual nanoparticles.

In order to determine the percentage of the lanthanides present in the sample of nanoparticles dispersed in hexanes, elemental maps were obtained by analyzing the sample using a Scanning Transmission Electron Holography Microscope (STEHM) (**Figure 2.7**) equipped with an Energy-Dispersive X-ray (EDX) spectrometer. An electron beam with an accelerating voltage of 200 kV is focused onto a nanometer-sized

spot on the sample. The beam is then scanned across the sample in order to excite the core electrons. The excited atoms emit X-rays with an energy equivalent to the difference in energy between the ground and excited states, thereby rapidly returning to the ground state. These X-rays are characteristic of the different elements, and by collecting the emission of X-rays from a specific sample spot, it is possible to identify the elements in that area. Furthermore, the intensity of the emitted X-rays allows for the quantification of the number of atoms of a specific element in the measured sample area. A full X-ray spectrum is collected for each pixel as the electron beam is raster scanned across the sample. The distribution of the element of interest in the sample can be displayed as an elemental map. The nanoparticles are stuck to the edges of the y-shaped lacey carbon on the grid, as shown in **Figure 2.7a**. Elemental maps were collected over 5 min until 100,000 counts had been collected by the detector. The elemental maps show that lanthanum and neodymium are present in the nanoparticles, and the increase in signal for the lanthanum compared to neodymium confirms that that there is more lanthanum than neodymium. The large amount of signal seen for fluorine is expected, as there should be three fluorines per one lanthanide.

A spectrum was also collected for the same region of the β-LaF_3:Nd^{3+} (5%) nanoparticles (**Figure 2.8**). Lanthanum peaks can be seen at approximately 1, 4.6, 5, and 33 keV. There are also clear neodymium peaks at approximately 1 keV and 5.7 keV. The neodymium peaks at approximately 5.2 keV and 37.5 keV are somewhat hidden as shoulders in the lanthanum peaks at 5 keV and 37.8 keV, respectively. The peaks below 0.5 keV are from carbon and oxygen.

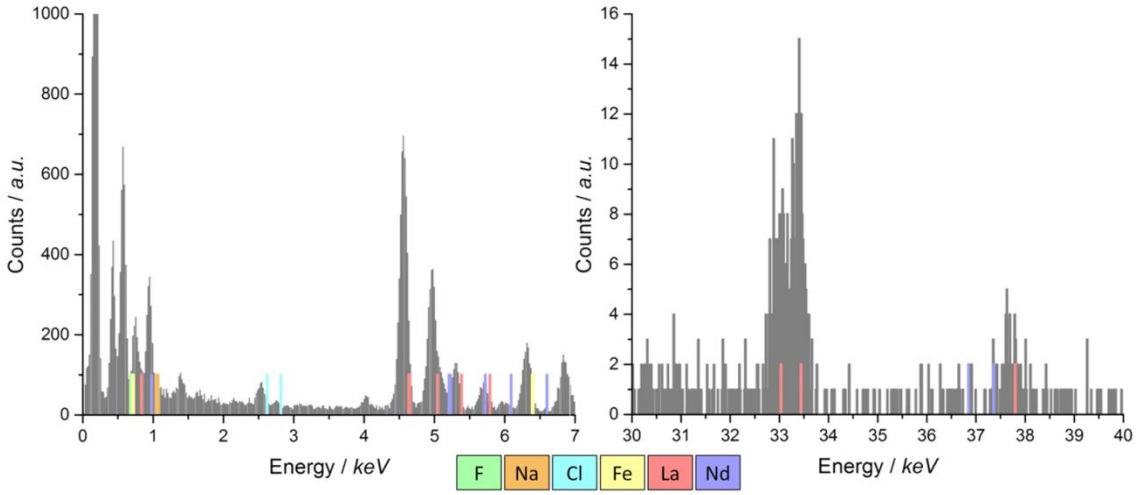

Figure 2.8—Elemental spectrum of β-LaF_3:Nd^{3+} (5%) nanoparticles dispersed in hexanes from 0-7 keV and from 30-40 keV. Nanoparticles are dispersed on a lacey carbon grid and measured with an accelerating voltage of 200 kV, an electromagnetic current of 3 μA, and measured in STEM mode.

2.2.2. Transfer of β-LaF_3:Nd^{3+} (5%) nanoparticles to 1-octadecene

Once these β-LaF_3:Nd^{3+} (5%) nanoparticles are used to make a colloidal laser, the nanoparticle solution must have a high boiling point in order to limit any evaporation as the solution heats up. This heating can be caused by both the pumping laser and by the non-radiative transitions that can occur in the solution. Therefore, the nanoparticles need to be dispersed in a liquid with a high boiling point. 1-Octadecene was chosen as it has a boiling point of 314.4 °C and absorbs very little, if at all, around 860-900 nm and 1020-1070 nm (**Figure 2.9**).

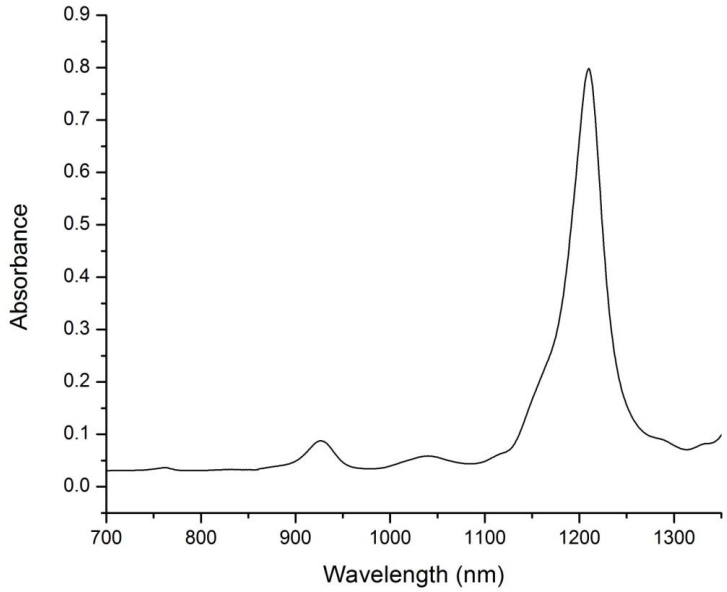

Figure 2.9—Absorption spectrum of 1-octadecene.

In order to transfer the nanoparticles from hexanes to 1-octadecene, an aliquot of the nanoparticles dispersed in hexanes was added to an equal volume of 1-octadecene. The hexanes were then evaporated out under a gentle argon flow, leaving the nanoparticles dispersed in the 1-octadecene (**Figure 2.10**).

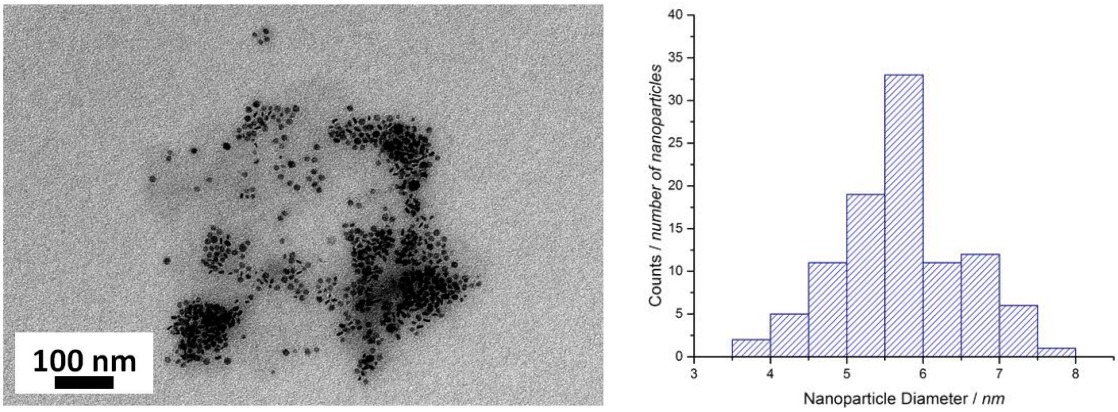

Figure 2.10—TEM image of β-LaF_3:Nd^{3+} (5%) nanoparticles dispersed in 1-octadecene **(left)**. The size distribution **(right)** shows that nanoparticles are ~5-6 nm in diameter.

The average diameter of the nanoparticles in 1-octadecene is 5.7 nm with a standard deviation of 0.8 nm. This size distribution is very similar to that of the nanoparticles dispersed in hexanes.

Inductively–Coupled Plasma Mass Spectrometry (ICP-MS) was used to determine the amounts of lanthanides present in the sample of nanoparticles dispersed in 1-octadecene. Overall, there was found to be 94.5 at%:5.5 at%, which is very close to the desired 95 at%:5 at% ratio of La^{3+}:Nd^{3+}.

2.2.3. Steady State Measurements

The emission spectra of the nanoparticles dispersed in hexanes and in 1-octadecene were measured using a Edinburgh Instruments FLS920 fluorimeter with an excitation wavelength of 785 nm (**Figure 2.11**). The peaks at 895 nm are from the $^4F_{3/2} \rightarrow {}^4I_{9/2}$ transitions and the peaks at 1064 nm are from the $^4F_{3/2} \rightarrow {}^4I_{11/2}$ transitions. The weak broad peaks around 1330 nm is from the $^4F_{3/2} \rightarrow {}^4I_{13/2}$ transitions. All of these peaks are characteristic of neodymium.

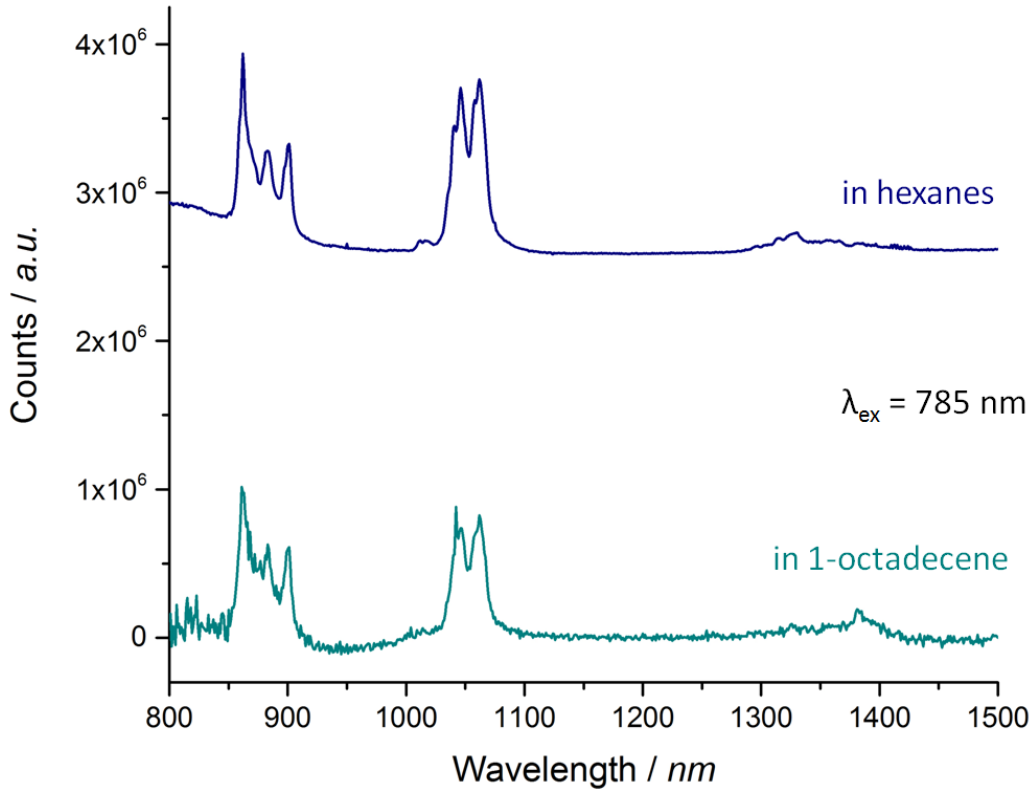

Figure 2.11—Emission spectra of β-LaF_3:Nd^{3+} (5%) nanoparticles dispersed in hexanes and in 1-octadecene.

2.2.4. Lifetime Measurements

Lifetime measurements were also performed on the solutions of the nanoparticles dispersed in hexanes and in 1-octadecene (**Figure 2.12**). Measurements were carried out over a 1 ms time scale, with an excitation wavelength of 532 nm and an emission wavelength of 1064 nm. The decay curves were fit using a multi-exponential decay function (**Equation 2.4**)

$$y = A + \sum B_i e^{(-t/\tau_i)} \qquad \textbf{Equation 2.4}$$

where A is the background, B_i is the amplitude of the i^{th} decay component, and τ_i is the lifetime of the i^{th} component.

Average lifetimes, τ_m, were calculated using the equation below (**Equation 2.5**)

$$\tau_m = \frac{\sum \alpha_i \tau_i^2}{\sum \alpha_i \tau_i} \qquad \textbf{Equation 2.5}$$

where the τ_i values are the measured lifetime values and the α_i values are the relative percentages of the corresponding lifetime components.

Table 2.3—Measured multi-component lifetimes and the calculated average lifetime data for the β-LaF_3:Nd^{3+} (5%) nanoparticles dispersed in hexanes and in 1-octadecene.

β-LaF_3:Nd^{3+} (5%)	τ_1	α_1	τ_2	α_2	τ_3	α_3	τ_m **(μs)**
in hexanes	106.65	59.97	26.41	27.88	5.35	12.15	**98**
in 1-octadecene	107.78	51.80	27.94	22.43	11.08	25.77	**96**

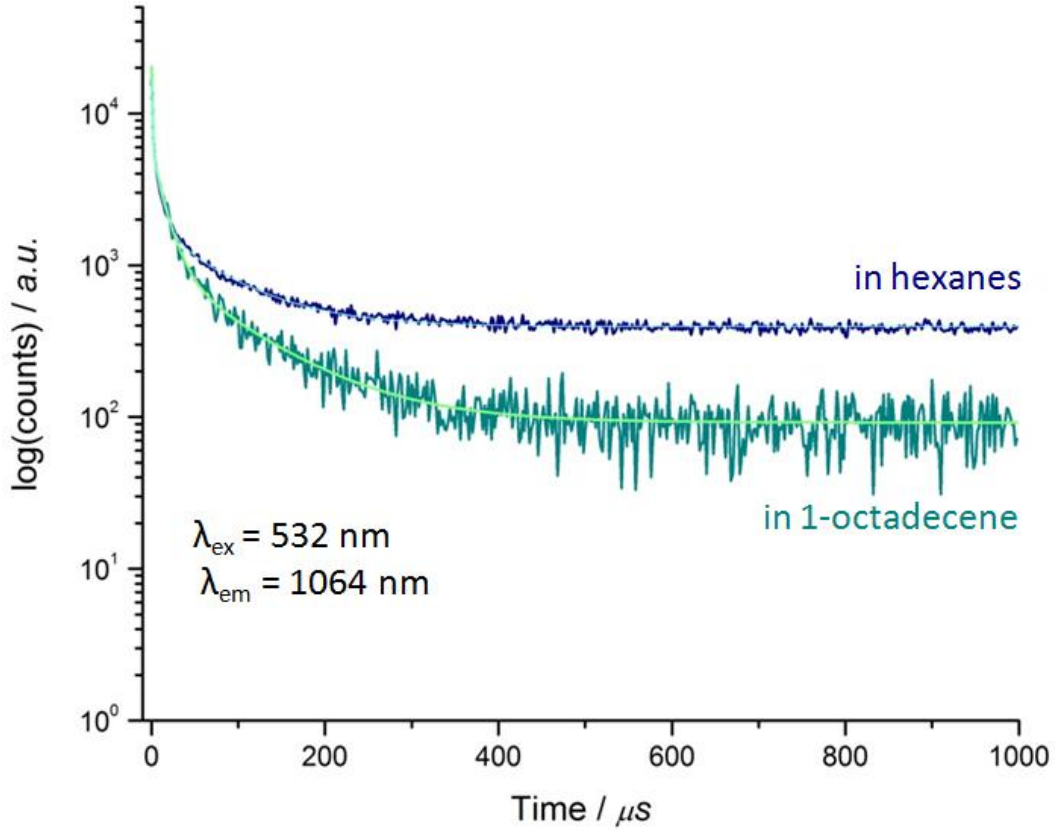

Figure 2.12—Lifetime measurements for β-LaF_3:Nd^{3+} (5%) nanoparticles dispersed in hexanes and in 1-octadecene with a line of best fit for both curves.

The average lifetime of the nanoparticles dispersed in hexanes was found to be 98 μs. From triplicate measurements, the standard deviation was found to be ±5 μs. This is extremely close to the desired 100 μs goal. When the nanoparticles were transferred to 1-octadecene, the average lifetime of the nanoparticles was found to be 96 μs. This good agreement of the average lifetimes suggests that the 1-octadecene has no negative impact on the fluorescent properties of the nanoparticles. When the lifetimes were fit with an exponential decay fit, the adjusted R-Square values were found to be 0.999 for the nanoparticles in hexanes and 0.998 for the nanoparticles in 1-octadecene.

2.3. Conclusions

The initial goals of this project were to achieve nanoparticles that were smaller than or equal to 5 nm in diameter with a 5 at% neodymium doping, that the nanoparticles were dispersed in a high boiling point liquid, and that the nanoparticles would exhibit lifetimes that were 100 μs or longer. As 98 ± 5 μs is very close to 100 μs, all of these initial goals were met.

As the current solution has a concentration of 2.3 wt% and is already becoming slightly cloudy due to the relatively high concentration of nanoparticles, the more recent requirement set by our collaborator that the solution must be close to 5 wt% is a further challenge that will need to be overcome.

One possible way to address this concentration issue could be to transfer the nanoparticles to a different liquid with a high boiling point. A different organic solvent could improve the clarity of the nanoparticle solution while potentially allowing for a higher concentration of nanoparticles in the solution. Many potentially suitable high boiling point solvents, such as dimethyl sulfoxide (DMSO), are polar and this leads to

significant lanthanide emission quenching. Additionally, reported methods for transferring oleate-stabilized nanoparticles to DMSO[45] are quite harsh towards the surface of the nanoparticles as they strip the oleates from the surface and replace them with BF_4^-. Growing a thin shell around the β-LaF_3:Nd^{3+} (5%) core could protect the nanoparticles from solution quenching as well as from harsh transfer conditions. However, it would be necessary to maintain the small size of the nanoparticles, and growing such a thin shell, even on smaller nanoparticles, could be difficult. If this concentration problem can be solved, these nanoparticles could eventually be used in a colloidal laser set-up.

2.4. Experimental Procedure

2.4.1. Chemicals

Lanthanum(III) chloride heptahydrate (99.9%, A.C.S. reagent), neodymium(III) chloride hexahydrate (99.99%), oleic acid (technical grade, 90%), 1-octadecene (technical grade, 90%), ammonium fluoride (≥99.99%), and hexanes (mixture of isomers, ≥98.5%) were purchased from Sigma-Aldrich. Sodium hydroxide was purchased from Caledon. Methanol (HPLC grade) was purchased from EMD. Anhydrous ethyl alcohol was purchased from Commercial Alcohols. All chemicals were used as received.

2.4.2. Synthesis of oleate-stabilized β-LaF_3:Nd^{3+} (5%) nanoparticles

The synthesis of the β-LaF_3:Nd^{3+} nanoparticles was done by modifying a previously reported method.[43] To a 100 ml 3-necked round bottom flask, 1 mmol of lanthanide chlorides (0.95 mmol $LaCl_3 \cdot 7H_2O$ and 0.05 mmol $NdCl_3 \cdot 6H_2O$) was added, along with oleic acid (6 ml) and 1-octadecene (17 ml). The solution was then heated to 150 °C under vacuum with constant magnetic stirring. This temperature was held for 1 h to fully

dissolve the salts and achieve a homogeneous solution. The solution was then cooled to room temperature. A solution of sodium hydroxide (1 mmol) and ammonium fluoride (3 mmol) dissolved in methanol (5 ml) was added to the 3-necked round bottom flask, and this mixture was stirred at room temperature for 1 h. The solution was then heated to 70 °C to allow the methanol to evaporate. A stream of argon was then introduced to the flask and the solution was heated to 300 °C. This temperature was held for 1 h. The solution was then cooled to room temperature. The nanoparticles were precipitated by adding anhydrous ethanol (23 ml) and centrifuging at 2,683 g forces (5,000 rpm, Beckman Coulter Spinchron 15 Series, F0850 rotor) for 5 min. The supernatant was removed and the resulting pellet was dispersed in a small volume of hexanes. Anhydrous ethanol (40 ml) was added, and the solution was centrifuged at the same settings as previously described. This washing step was repeated so that the solution of nanoparticles were centrifuged a total of three times. Finally, the nanoparticles were dispersed in hexanes (10 ml).

2.4.3. Transfer of oleate-stabilized β-LaF_3:Nd^{3+} (5%) nanoparticles to 1-octadecene

An aliquot of the oleate-stabilized β-LaF_3:Nd^{3+} (5%) nanoparticles dispersed in hexanes was placed under a gentle argon stream in order to evaporate the hexanes. When the solution had been concentrated approximately 10 times, a volume of 1-octadecene equal to the volume of hexanes initially present was added. The remaining hexanes were then evaporated out under the argon stream.

2.4.4. Transmission Electron Microscope (TEM) images

A JEOL JEM-1400 microscope was used for all TEM images. An operating voltage of 80 kV was used. In order to prepare a sample for imaging, a diluted solution of the

nanoparticles was drop cast onto the TEM grid (formvar carbon film on 300 mesh copper grids, 3 mm in diameter, from Electron Microscopy Sciences). Grids were dried in air before imaging. The embedded scale bar was calibrated against nanoparticles of a known size. The size distribution of the nanoparticles was measured by counting 100 nanoparticles. Sizes were measured using ImageJ software (version 1.48).

2.4.5. X-ray Diffraction (XRD) measurements

XRD patterns were obtained using a Rigaku Miniflex X-ray diffractometer with a chromium source (K_α λ = 2.2890 Å) operating at 30 kV and 15 mA. A sampling width of 0.05 ° (2θ) and a scan speed of 1 °/minute were used.

2.4.6. Absorption measurements

Absorption measurements were done using a PerkinElmer Lambda 1050 UV/Vis/NIR spectrometer. A quartz cuvette with a path length of 1 cm was used. A sampling width of 1 nm was used.

2.4.7. Steady state and lifetime measurements

All optical measurements were done using an Edinburgh Instruments FLS920 fluorimeter. A quartz cuvette with a path length of 1 cm was used for both steady state and lifetime measurements. All data was collected using Edinburgh Instruments F900 software (version 6.41).

Steady state: The excitation source for these measurements was a Coherent 2-pin SMA connectorized 785 nm diode laser (F2 series) coupled to a 100 µm core fiber. Spectra were collected using a liquid nitrogen-cooled Hamamatsu R5509 photomultiplier tube (PMT) detector. A short band-pass filter (850 nm) was used on the emission side in

order to remove any excitation light that had been scattered. All measurements were collected using a 1 nm resolution. The incident photon flux was kept at ~32 W/cm^2.

Lifetime measurements: All lifetime measurements were collected using 532 nm excitation wavelength from the OPOTEK vibrant IIb. Time traces were collected using a Peltier-cooled Hamamatsu R955 photomultiplier tube (PMT) detector. A 1 ms time range was used along with 500 channels to achieve a 2.0 μs/channel binning, and a stop condition of 5,000 counts was used for bin 2.

2.4.8. Energy dispersive X-ray spectroscopy (EDX)

Energy dispersive X-ray spectroscopy (EDX) analysis was performed using a Bruker system on a Hitachi HF-3300V scanning transmission electron holography microscope (STEHM) operating in scanning transmission electron microscopy (STEM) mode with an accelerating voltage of 200 kV and an emission current of 3 μA. In order to prepare a sample for imaging, 10 μl of a diluted solution of the nanoparticles was drop cast onto a lacey carbon grid. After 1 minute, excess solution was wicked off using a filter paper. Grids were dried in air. Grids were then placed in a Hitachi Zone-TEM UV cleaner to be cleaned for 10 min, before putting them into the STEHM. Elemental analysis was performed using Esprit software (version 1.9).

2.4.9. Inductively–Coupled Plasma Mass Spectrometry (ICP-MS)

Analysis was completed using a Thermo X-Series II (X7) quadrupole ICP-MS to determine the La^{3+} and Nd^{3+} ion concentrations in the nanoparticle solutions.

Samples were prepared by pipetting an aliquot of PVP-stabilized nanoparticles (50 μl) into a pre-weighed Teflon vial along with nitric acid (1 ml, 16 N environmental grade). The final weight was recorded and the solution was then heated to 125 °C for at least

24 h. The cooled solution was quantitatively transferred into a pre-weighed high-density polyethylene (HDPE) bottle which was then filled with deionized (DI) water. The solution was completely mixed by inversion and the final weight was recorded. An aliquot of this diluted solution (1 ml) was then pipetted into a tared autosampler vial and the weight was recorded. Finally, the solution was diluted with nitric acid (10 ml, 2%) and was mixed by inversion.

Each sample was spiked with indium and rhenium to a concentration of ~7 ppb each. This was the internal standard which allows for the correction of signal drift and matrix effects. A standard reference material (SLRS-5) was used to confirm the accuracy of the analysis.

Chapter 3: Introduction of Ytterbium into β-$NaYF_4$:Er^{3+} Nanoparticles Via Cation Exchange

3.1. Introduction

3.1.1. Current radiation therapies

Currently there is a high demand for more effective and less invasive therapies in medicine. In cancer therapy involving tumours, around 50% of therapies involve some method of radiation.[46] Existing radiation therapies can be quite damaging to healthy tissues. It is important to irradiate all of the cancer cells at once and with a sufficient dose, otherwise it is possible for the remaining cells to become resistant to radiation therapy.[46-47] This is especially challenging for irregularly shaped tumours. If a tumour is unevenly shaped, the radiation may not irradiate all parts of the tumour equally.[48] Irradiating all of the cancer cells at once can also be almost impossible if the tumour has metastasised.[48] When cells break away from the tumour and spread throughout the body, they become increasingly hard to detect and therefore cannot be targeted with radiation.

There are several methods of delivering radiation therapy to a tumour.[49] Two of the most common methods of radiation oncology are external beam radiation therapy and brachytherapy. External beam radiation therapy involves moving an external source of radiation around the patient in an attempt to localise the radiation at the tumour. The major disadvantage of this technique is that it typically requires large doses of radiation in order to destroy the tumour but this can be extremely damaging to the surrounding healthy tissue.[47a] Brachytherapy is an internal radiation therapy where a radiation source is inserted near the tumour. The major advantage of brachytherapy is that the delivery of radiation is targeted to the tumour, and as a result, damage to healthy tissue is minimized.[50] Even today, brachytherapy is still relatively invasive. There are two main

methods of treatment. The low dose radiation (LDR) involves permanently implanting radioactive seeds that slowly decay over time. One main disadvantage of the LDR method is that the seeds can migrate away from the tumour site.[51] The treatment becomes decidedly less effective if the radiation is no longer near the tumour. Once the seeds have left the area surrounding the tumour, they can settle in small cavities throughout the body and lead to edema.[51-52] The high dose radiation (HDR) method involves placing thin catheters in the tumour. A small radioactive pellet is pushed into each of the catheters, and patients usually have to stay overnight for multiple rounds of this treatment.[53] While brachytherapy is useful for stationary tumours, it is not practical for tumours that have metastasised and have small pieces or cells that have broken off of the tumour and are travelling throughout the body, as the seeds are not designed to target tumour cells.[54]

3.1.2. Nanoparticles and radiation therapy

In order to improve how radiation is delivered while minimizing the harm caused to healthy tissue, a new method of treatment needs to be developed. Our goal is to incorporate radioactive lanthanides into nanoparticles that have been labeled with antibodies to make the nanoparticles cancer cell specific. Examples of antibodies include anti-PSMA for prostate cancer, anti-HER2 for breast cancer, as well as antibodies for CD133, CD44, and ALDH1 for various other cancers.[55]

In this way, it would be possible to deliver high doses of radiation directly to tumour cells anywhere in the body and would avoid damaging healthy tissues with excess radiation. It would allow for treatment of irregularly shaped tumours and the

nanoparticles would be able to track down individual cancer cells that have metastasized.[56]

There are two lanthanides with specific isotopes that are attractive for this project. One isotope is yttrium-90 (^{90}Y) which emits a β-particle with a kinetic energy of 939 keV.[57] Yttrium-90 is of interest because it is a by-product of nuclear waste from strontium-90.[58] The other lanthanide that could be used for this approach is lutetium-177 (^{177}Lu). Lutetium-177 emits a β-particle with a kinetic energy of 498 keV energy and also emits gamma energies of 113 keV and 208 keV, which are valuable as they are in the appropriate energy range for Single-Photon Emission Computed Tomography (SPECT) imaging.[59] While yttrium-90 would be useful for larger tumours (0.5-1 cm), lutetium-177 would be more suitable for tumours that are a couple of millimeters in size. Both of these lanthanides have long half-lives; yttrium-90 has a half-life of 2.7 days and lutetium-177 has a half-life of 6.73 days.[57, 59] These long half-lives would allow the nanoparticles to be synthesized in one location and then shipped anywhere in the world for treatment, retaining enough radiation to be potent. However, the half-lives are short enough that they would decay before causing any significant long-term damage to the surrounding healthy tissue.[57]

To date, very little work has been done in incorporating yttrium-90 or lutetium-177 into nanoparticles[60]. Non-radioactive lutetium was used as a surrogate for ^{177}Lu in $LuPO_4$-apoferritin core-shell nanoparticles to test their potential applications in cancer radiotherapy.[60a] Yttium-90 albumin microspheres with encapsulated citrate-stabilized magnetite nanoparticles were developed with dual application for radiotherapy and hyperthermia,[60b] a method whereby vibrations of the magnetic nanoparticles induced by

an external magnetic field induce local heating. ^{90}Y was also recently doped into GdF_3 nanoparticles to create nanoparticles suitable for MRI imaging as well as Cerenkov radioluminescence imaging.[57]

3.1.3. Project Goals

Making radioactive nanoparticles that are tumour-cell specific involves many synthetic steps. First, the nanoparticles need to be synthesized. As the as-synthesized nanoparticles are often only dispersible in organic solvents, a phase-transfer would need to be done in order to make the nanoparticles water-dispersible, which is a pre-requisite for their use in biological applications. Finally, the appropriate antibodieswould need to be attached to the surface of the nanoparticles in order to make them tumour-cell specific. Since any work involving radioactive isotopes must be done in an isotope laboratory, a simple method for incorporating the radioactive lanthanides at, or near, the end of the synthesis procedure is desired.

In order to incorporate the radioactive lanthanides into water-dispersed nanoparticles, a cation exchange or core-shell synthesis is necessary. There have been many reports of using a cation exchange process to create or modify nanoparticles. Alivisatos and coworkers have been using cation exchange processes for years, starting with the exchange of Ag^+ for cadmium in CdSe semiconductor nanoparticles,[61] and more recently, for converting CdS nanowires to semiconducting $Cu_{2-x}S$ nanowires.[62] Many core-shell nanoparticles, such as Se-CdSe[63] and PbSe-CdSe[64] have been made. Previously in our group, it has been shown that Gd^{3+} could be exchanged for La^{3+} (and vice versa) in citrate-stabilized β-LaF_3 nanoparticles.[14] It was also shown that this cation exchange process could be used to grow thin shells of $NaGdF_4$ onto $NaYF_4$:Yb^{3+},Tm^{3+}.[15]

Before a cation exchange process could be attempted with radioactive isotopes, it would first be necessary to prove that a cation exchange could be possible through a barrier of ligands on the surface of the water-dispersible nanoparticles. In principle, this could be done using non-radioactive, often called "cold", yttrium or lutetium. However, as it would be extremely challenging to distinguish between the newly incorporated lanthanide cations and the original lanthanide cations in the nanoparticles, confidently confirming the success of a cation exchange for yttrium would essentially be impossible.

To test the possibility of a cation exchange mechanism, the synthesis of upconverting nanoparticles via cation exchange was explored. The goal was to start with $NaYF_4:Er^{3+}$ nanoparticles and then partially exchange some of the erbium cations for ytterbium cations. If the reaction was successful, upconverting nanoparticles may be observed. Upconversion occurs when two lower energy photons are combined to form one higher energy photon.

Lanthanides are suitable candidates for upconversion for a couple of reasons. As transitions within the 4*f* orbitals are forbidden, the lifetime of the decay from the excited state to the ground state is very long and the extinction coefficients for absorption are very low.

While there are many mechanisms for the upconversion process, there are three main upconversion mechanisms that will be discussed here. It is possible to have upconversion by involving only one ion (**Figure 3.1**). In this case, the lanthanide ion absorbs two photons in succession, followed by the emission of one photon that is higher in energy than the incident photons. This process is called ground state absorption/excited state absorption, and it heavily relies on the long lifetime of the Ln^{3+} energy levels.[10]

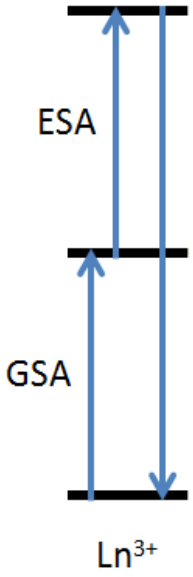

Figure 3.1—Schematic of the ground state absorption (GSA)/excited state absorption (ESA) mechanism, whereby two successive photons are absorbed, followed by emission of one photon with shorter wavelength (higher energy).

The remaining two mechanisms involve more than one lanthanide ion. The first involves a radiative energy transfer (**Figure 3.2**). A donor lanthanide cation absorbs a photon (1) and then re-emits a photon (2). A nearby acceptor cation absorbs that photon and is raised to an excited state (3). Another donor absorbs the energy of incoming excitation (4) and then re-emits a photon (5), which the excited acceptor absorbs before it can relax back to the ground state (6), and is therefore excited to an even higher excited state. The acceptor then relaxes to ground state emitting photon with shorter wavelength (higher energy) than the incident energy (7).

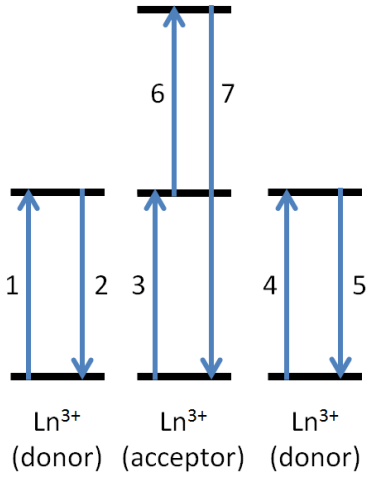

Figure 3.2—Simplified schematic of the *radiative* energy transfer upconversion mechanism.

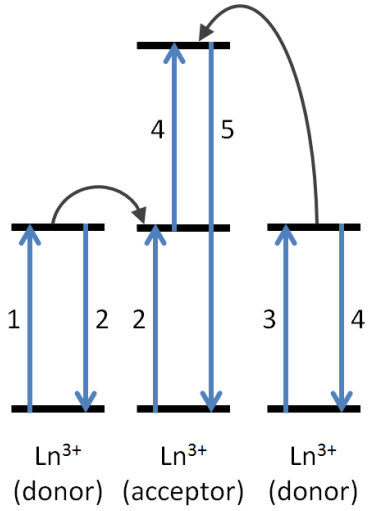

Figure 3.3—Simplified schematic of the *non-radiative* energy transfer upconversion mechanism.

In the third mechanism, the energy transfer is non-radiative (**Figure 3.3**). The donor cation absorbs a photon (1) and transfers its energy to an acceptor cation without emitting light (2). The acceptor is now in excited state (2). Meanwhile, another donor absorbs another photon (3) and transfers its energy to the excited acceptor before it can relax back

to the ground state (4). The acceptor is therefore excited to an even higher excited state. Finally, the acceptor then relaxes to ground state emitting photon with shorter wavelength (higher energy) than the incident energy (5). The length of the lifetimes of the energy levels involved in a specific upconversion process will determine which mechanism dominates.

When doped in the right concentrations, a combination of Yb^{3+} and Er^{3+} results in the emission of green light, as can be seen in the simplified energy level diagram in **Figure 3.4**.[65] Although there is no direct link between the photoluminescent properties of these nanoparticles and their use as a cancer radiation therapy, the optical presence of green emitted light would be a sign of success.

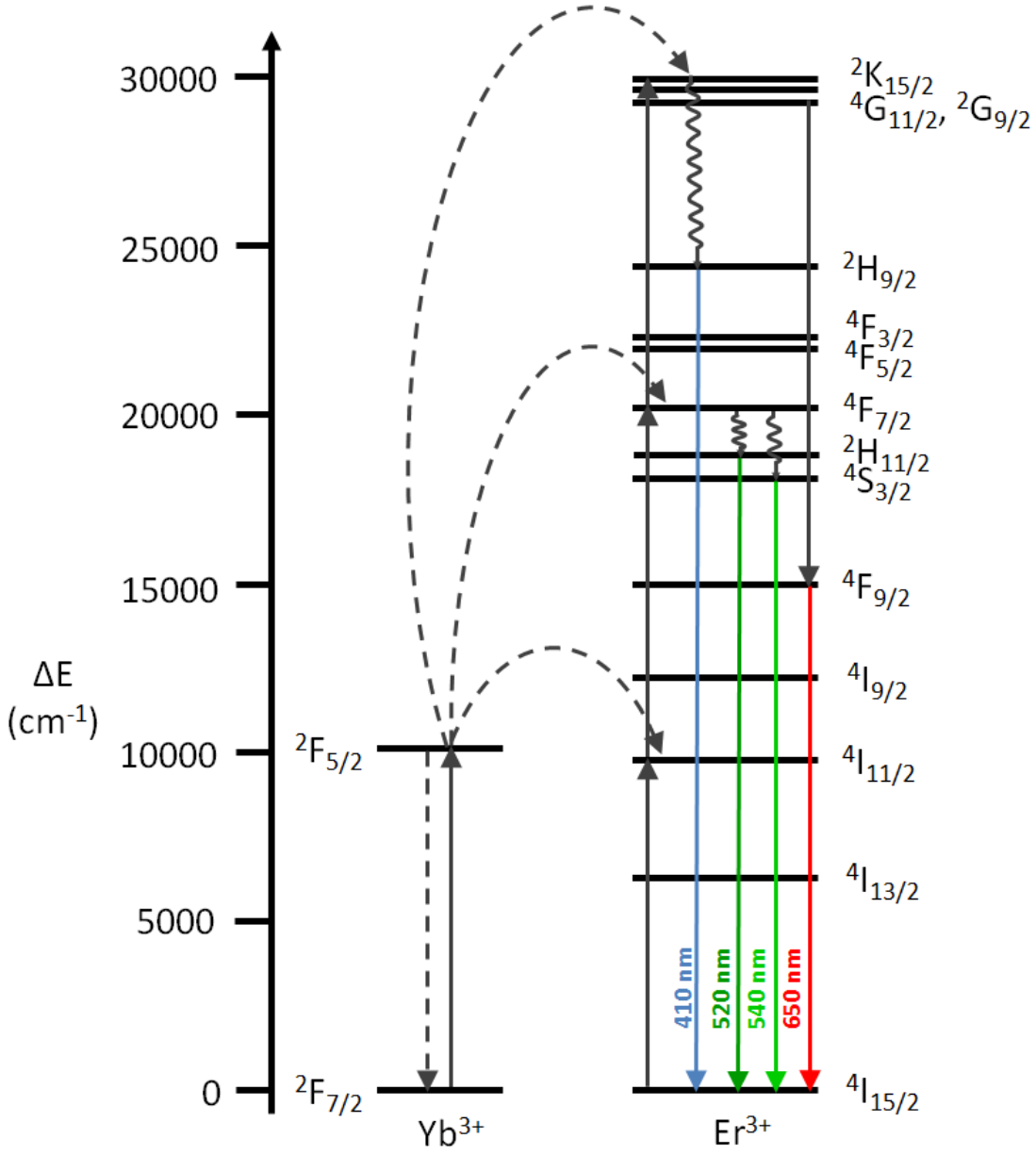

Figure 3.4—Upconversion of ytterbium and erbium with simplified 4*f* energy levels.[65]

3.2. Results and Discussion

3.2.1. Synthesis of oleate-stabilized β-$NaYF_4$:Er^{3+} nanoparticles

The synthesis of oleate-stabilized β-$NaYF_4$:Er^{3+} nanoparticles was carried out by dissolving the appropriate amounts of yttrium and erbium chloride salts in a mixture of

oleic acid and 1-octadecene.[43] This solution was then mixed with a solution of sodium hydroxide and ammonium fluoride in methanol and was then heated with a heating mantle to 300 °C for 1 h. The resulting nanoparticles with varying amounts of erbium (2%, 15%, and 50%) were made (**Figure 3.5**).

Generally during the synthesis of β-$NaYF_4$ nanoparticles, the cubic (kinetic) phase is formed at lower temperatures. As the temperature continues to rise, this product dissolves and nucleates as the hexagonal (thermodynamic) phase. This is then followed by a growth period at a constant temperature, which allows for the formation of uniform β-$NaYF_4$ nanoparticles.[29, 66]

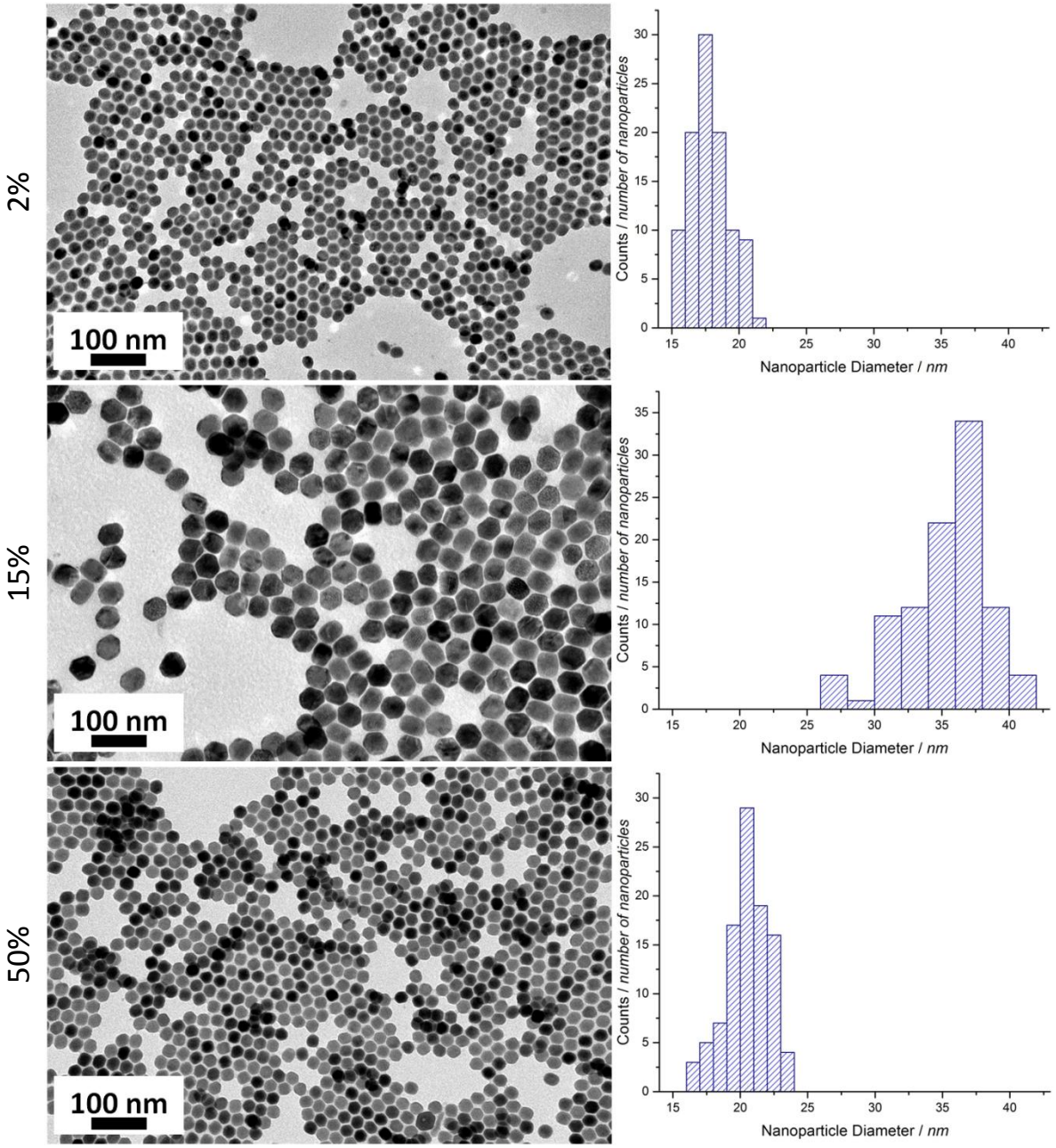

Figure 3.5—TEM images of β-$NaYF_4$:Er^{3+} nanoparticles with 2%, 15, and 50% erbium dispersed in hexanes. The size distribution shows that nanoparticles are ~18 nm, ~35 nm, and ~21 nm in diameter, respectively.

The average diameters of the samples in hexanes are summarized in **Table 3.1**.

Table 3.1—Average diameters and standard deviations for the β-$NaYF_4$:Er^{3+} nanoparticles dispersed in hexanes.

Sample	Average diameter (nm)	Standard deviation (nm)
$NaYF_4$:Er^{3+} (2%)	17.8	1.5
$NaYF_4$:Er^{3+} (15%)	35.3	3.1
$NaYF_4$:Er^{3+} (50%)	20.5	0.8

Analysis using powder X-ray diffraction (**Figure 3.6**) showed that the peaks of both samples are in close agreement with the reference peaks for bulk β-$NaYF_4$ (JCPDS #00-016-0334), which confirms the formation of β-$NaYF_4$. The slight deviation can be attributed to the fact that the reference material is in the bulk phase and the sample is made up of nanoparticles.

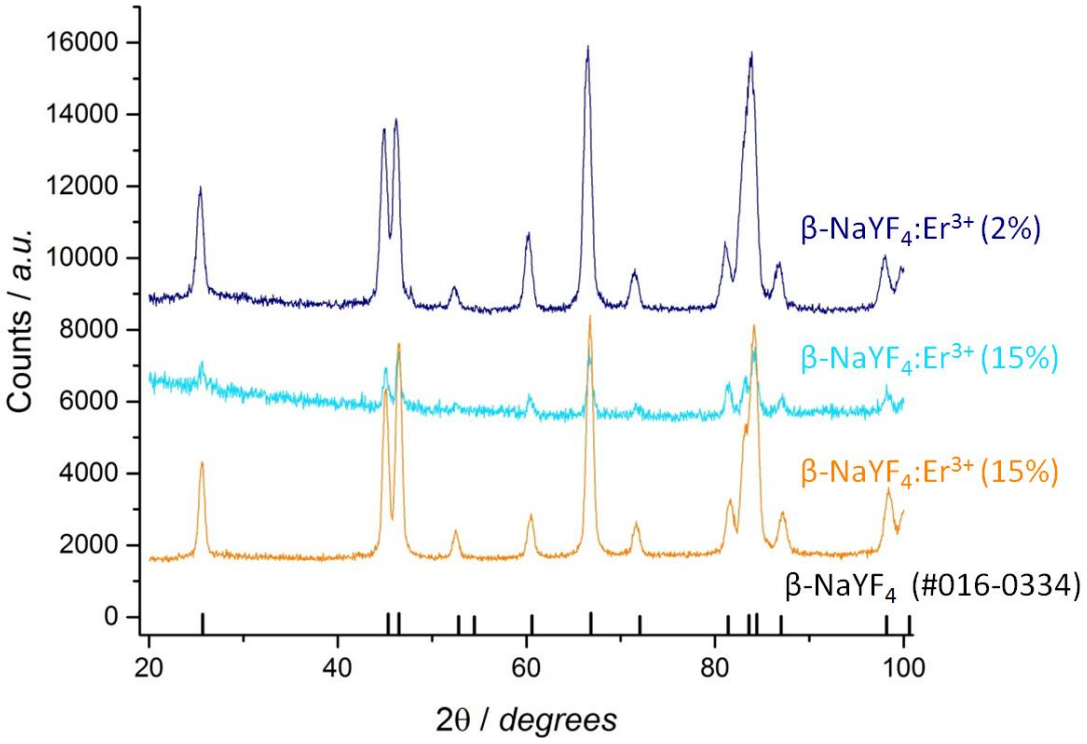

Figure 3.6—XRD of β-$NaYF_4$:Er^{3+} nanoparticles with 2%, 15%, and 50% erbium with reference β-$NaYF_4$ (reference #00-016-0334).

3.2.2. Phase transfer of oleate-stabilized β-$NaYF_4$:Er^{3+} nanoparticles to water using PVP

In order to transfer the nanoparticles from hexanes to water, the nanoparticle solution was mixed with dimethylformamide, dichloromethane, and polyvinylpyrrolidone. The solution was refluxed for 8 h, then the nanoparticles were precipitated using ethyl ether and finally were dispersed in water (**Figure 3.7**). The denser regions on the grid are due to the drying of the nanoparticle solution on the grid and not to possible cross-linking of the PVP, as individual nanoparticles can still clearly be seen.

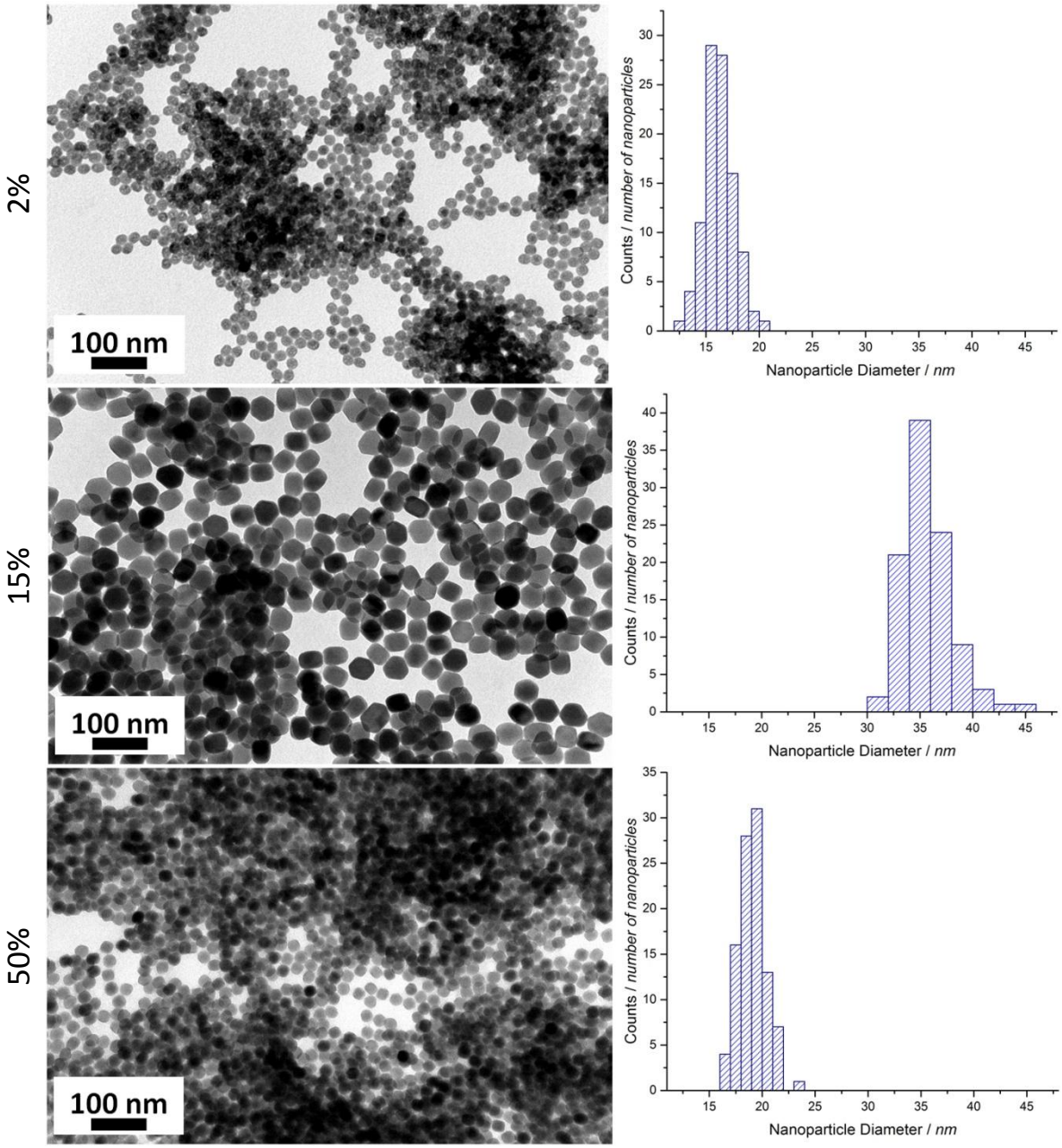

Figure 3.7—TEM images of β-$NaYF_4$:Er^{3+} nanoparticles with 2%, 15, and 50% erbium dispersed in water. The size distribution shows that nanoparticles are ~16 nm, ~36 nm, and ~19 nm in diameter, respectively.

The average diameters of the samples in hexanes are summarized in **Table 3.2**. While the sizes of the samples are not identical, all three of the samples have very good size distributions.

Table 3.2—Average diameters and standard deviations for the β-$NaYF_4:Er^{3+}$ nanoparticles dispersed in water before the cation exchange.

Sample	Average diameter (nm) ± standard deviation (nm)
$NaYF_4:Er^{3+}$ (2%)	16.3 ± 1.4
$NaYF_4:Er^{3+}$ (15%)	35.7 ± 2.4
$NaYF_4:Er^{3+}$ (50%)	19.1 ± 1.3

The sizes of the nanoparticles dispersed in water are very similar to those of the nanoparticles dispersed in hexanes.

ICP-MS was used to quantify the amount of yttrium and erbium in the samples. The results can be seen in **Table 3.3**.

Table 3.3—ICP-MS results of the nanoparticles before the cation exchange.

Sample	%Y	%Er
$NaYF_4:Er^{3+}$ (2%)	98.3	1.7
$NaYF_4:Er^{3+}$ (15%)	82.6	17.3
$NaYF_4:Er^{3+}$ (50%)	44.6	53.9

The percentages seen in **Table 3.3** closely match the desired ratios. There was found to be 0.1% ytterbium in the $NaYF_4:Er^{3+}$ (15%) sample and 1.5% ytterbium in the $NaYF_4:Er^{3+}$ (50%) sample. This is most likely due to a ytterbium contamination in the initial erbium(III) chloride salt.

3.2.3. Cation exchange of PVP-stabilized β-$NaYF_4:Yb^{3+}/Er^{3+}$ nanoparticles

In order to exchange some of the erbium and ytterbium cations in the nanoparticles for ytterbium cations, ytterbium chloride was dissolved in deionized water and mixed with an aliquot of the nanoparticles in water. The solution was then heated to 75 °C for 1 h, was cooled to room temperature, and was then dialyzed for 24, 48, and 72 h to remove any excess cations. All of the samples were also washed 3 times by precipitating the

nanoparticles using acetone, centrifuging the solution, and then dispersing the nanoparticles in water. This was done to remove any cations that might be trapped in the PVP on the surface of the nanoparticles, as opposed to any cations actually incorporated into the nanoparticles.

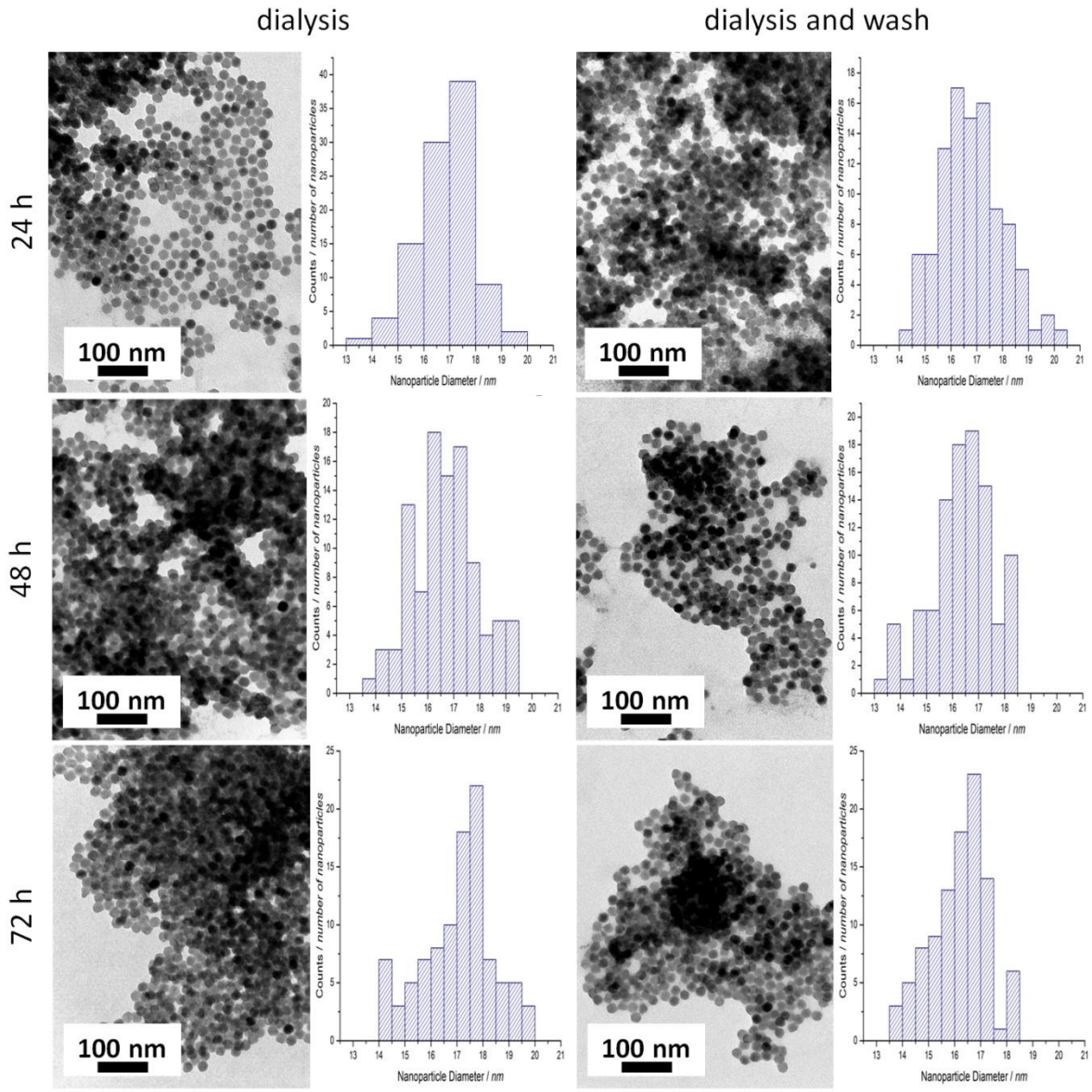

Figure 3.8—TEM images of β-$NaYF_4$:Er^{3+} (2%) nanoparticles after the cation exchange after various amounts of dialysis time and with or without washing. All samples are dispersed in water and imaged. Size distributions are shown to the right of each TEM image.

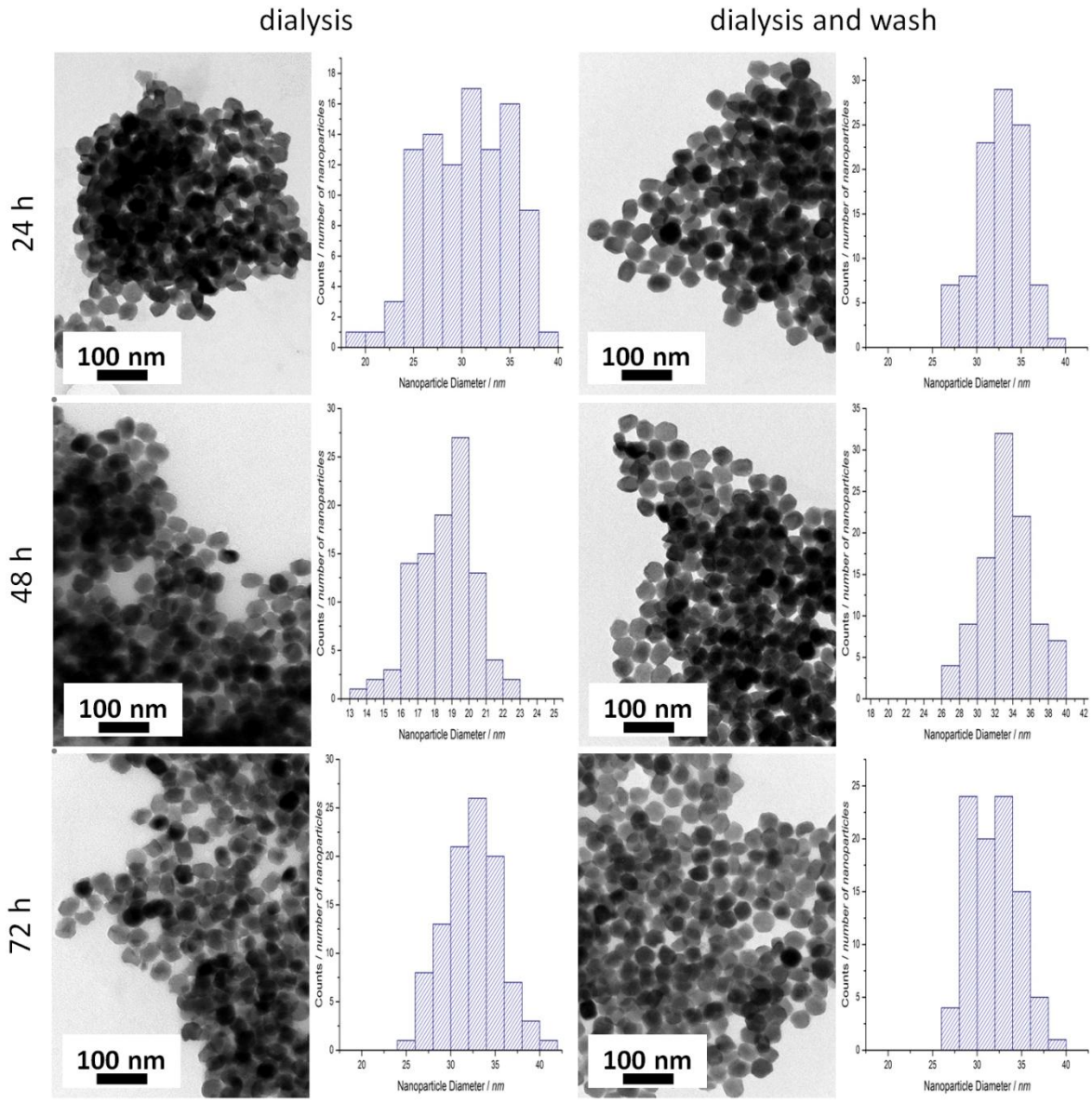

Figure 3.9—TEM images of β-$NaYF_4$:Er^{3+} (15%) nanoparticles after the cation exchange after various amounts of dialysis time and with or without washing. All samples are dispersed in water and imaged. Size distributions are shown to the right of each TEM image.

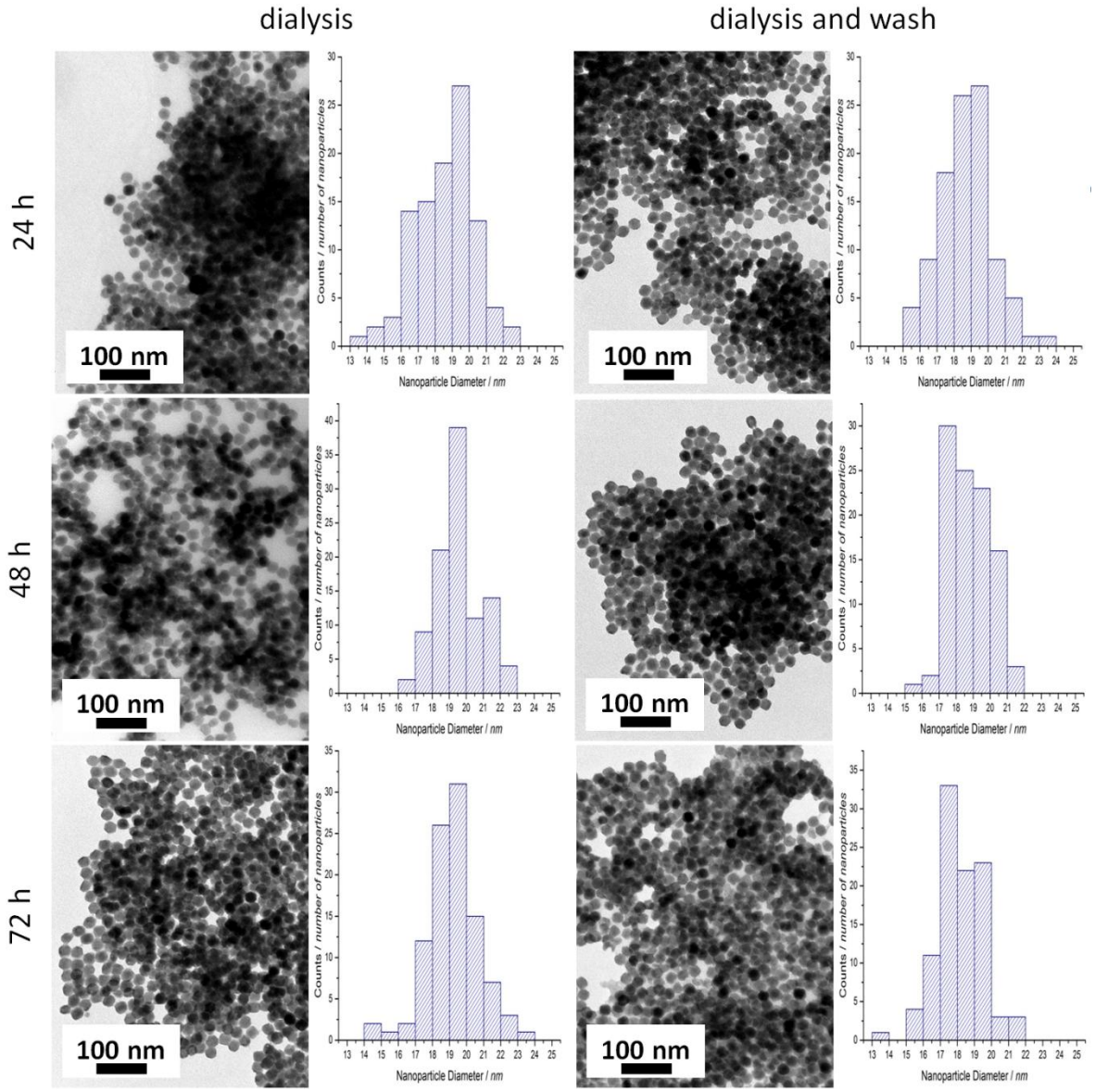

Figure 3.10—TEM images of β-$NaYF_4$:Er^{3+} (50%) nanoparticles after the cation exchange after various amounts of dialysis time and with or without washing. All samples are dispersed in water and imaged. Size distributions are shown to the right of each TEM image.

Table 3.4—Summary of average diameters and standard deviations for the β-$NaYF_4$:Er^{3+} nanoparticles dispersed in water after the cation exchange.

	Average diameter (nm) ± standard deviation (nm)		
% Er^{3+}	**2%**	**15%**	**50%**
24 h dialysis	16.9 ± 1.0	30.6 ± 4.3	18.6 ± 1.7
24 h dialysis, 3 washes	16.8 ± 1.2	32.7 ± 2.6	18.7 ± 1.5
48 h dialysis	16.7 ± 1.2	32.7 ± 3.1	19.6 ± 1.3
48 h dialysis, 3 washes	16.4 ± 1.1	33.3 ± 2.9	18.8 ± 1.3
72 h dialysis	17.1 ± 1.4	32.5 ± 3.2	19.2 ± 1.5
72 h dialysis, 3 washes	16.2 ± 1.0	32.1 ± 2.6	18.1 ± 1.3

The sizes of the nanoparticles dispersed in water before the cation exchange are very similar to those of the nanoparticles dispersed in water directly after the cation exchange (after 24 h of dialysis). The nanoparticles also appear to stay constant in size after longer periods of dialysis and after extra washes by centrifugation. If the ytterbium became trapped in the PVP and formed a layer close to the surface of the nanoparticles, the size of the nanoparticles should have increased directly after the cation exchange, and the nanoparticle diameter should have become smaller as the nanoparticles were washed and dialyzed for longer. This consistency in size suggests that the ytterbium was indeed incorporated into the nanoparticles as opposed to simply being loosely trapped in the PVP near the surface of the nanoparticles.

ICP-MS was then used to quantify the amount of erbium and ytterbium in the samples. The results can be seen in **Table 3.5** and **Figure 3.11**.

Table 3.5—ICP-MS results of the nanoparticles after the cation exchange.

Sample		**%Y**	**%Er**	**%Yb**
$NaYF_4:Er^{3+}$ (2%)	after 24 h dialysis	74.4	1.4	24.2
	after 24 h dialysis and 3 washes	72.9	1.8	25.3
	after 48 h dialysis	82.2	2.0	15.8
	after 48 h dialysis and 3 washes	82.8	2.0	15.2
	after 72 h dialysis	88.5	2.1	9.4
	after 72 h dialysis and 3 washes	88.9	2.1	9.0
$NaYF_4:Er^{3+}$ (15%)	after 24 h dialysis	68.4	17.0	14.6
	after 24 h dialysis and 3 washes	68.7	16.8	14.5
	after 48 h dialysis	68.8	17.3	13.9
	after 48 h dialysis and 3 washes	69.8	17.6	12.6
	after 72 h dialysis	70.2	17.6	12.2
	after 72 h dialysis and 3 washes	70.2	17.7	12.1
$NaYF_4:Er^{3+}$ (50%)	after 24 h dialysis	32.6	43.1	24.3
	after 24 h dialysis and 3 washes	32.6	43.0	24.4
	after 48 h dialysis	33.1	43.8	23.1
	after 48 h dialysis and 3 washes	33.1	43.7	23.2
	after 72 h dialysis	33.3	43.9	22.8
	after 72 h dialysis and 3 washes	33.1	44.0	22.9

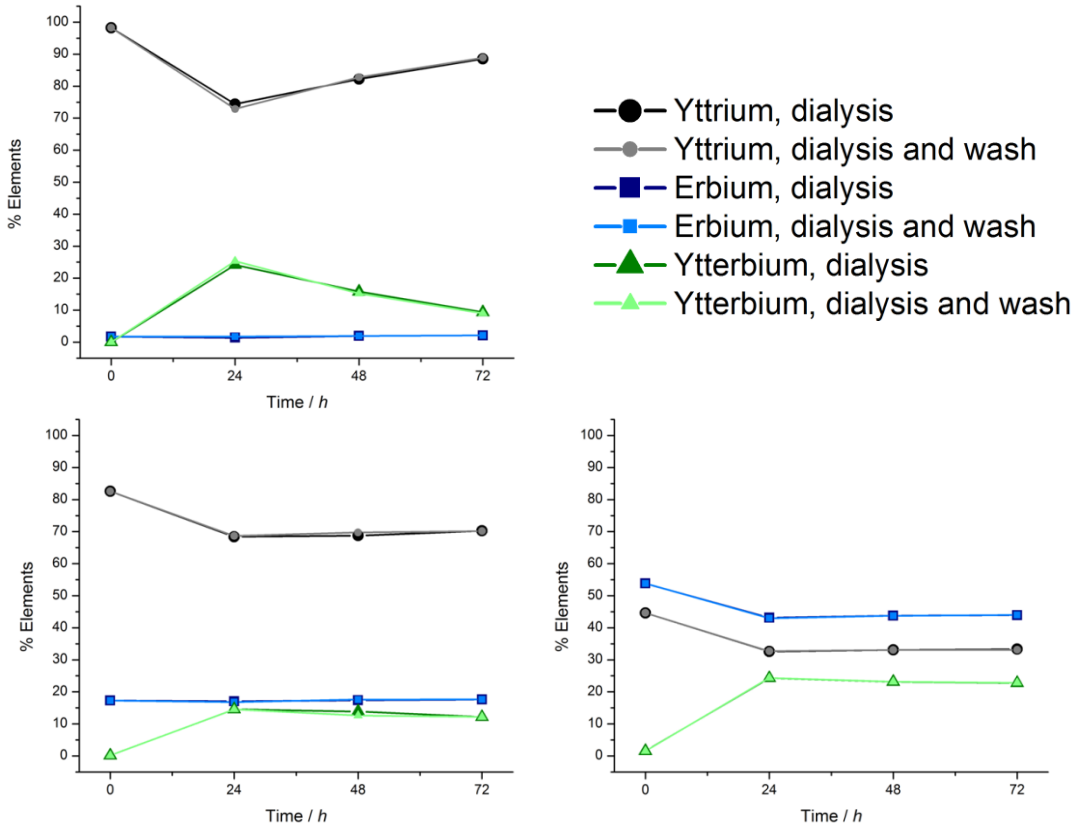

Figure 3.11—ICP-MS results for the β-$NaYF_4$:Er^{3+} (2%) nanoparticles **(top left)**, β-$NaYF_4$:Er^{3+} (15%) nanoparticles **(bottom left)**, and β-$NaYF_4$:Er^{3+} (50%) nanoparticles **(bottom right)** before (t=0 h) and after (t=24, 48, 72 h) the cation exchange.

The percentages reported in **Table 3.5** and plotted **Figure 3.11** are relative percentages: the sum of the yttrium, erbium, and ytterbium is equal to 100% of the lanthanides in the nanoparticles. In the results for the cation exchange reaction performed on the β-$NaYF_4$:Er^{3+} (2%) nanoparticles, the ytterbium does not appear to have successfully incorporated into the nanoparticles, as the % Yb decreases significantly over dialysis time (**Figure 3.11**). This explains the increase in % Y over time. Since the total %lanthanides must be equal to 100%, a relatively constant % Er and a decreasing % Yb will lead to an increasing % Y.

The cation exchange reactions for the β-$NaYF_4$:Er^{3+} (15%) and (50%) nanoparticles do appear to have been a success as there is an almost negligible decrease in the % Yb over dialysis time (**Figure 3.11**). The % Er is relatively constant in the β-$NaYF_4$:Er^{3+} (15%) sample, indicating that only yttrium was exchanged for ytterbium. However, in the β-$NaYF_4$:Er^{3+} (50%) sample, there is a decrease of almost 10% (absolute) in the % Er after the cation exchange when compared to the initial value. This suggests that there may be a minimum doping ion concentration below which only the host cations (in this case, yttrium) and not the doping cations (the erbium) will not be exchanged. The driving force behind the cation exchange is the presence of a concentration gradient between the nanoparticles with a low concentration of ytterbium and the aqueous environment with a high concentration of ytterbium. By introducing an excess of ytterbium cations and providing a small amount of energy in the form of gentle heating of the solution, the ytterbium can exchange for erbium and yttrium. This is facilitated by the small size difference between the lanthanide cations involved in the reaction.

There does not seem to be a significant difference between the samples that underwent only dialysis and the samples that underwent both dialysis and washing. This further confirms that the ytterbium was successfully incorporated into the nanoparticles, as the washing step should have dislodged any excess ytterbium even if the dialysis could not.

3.2.5. Steady State Measurements

The emission spectra of the β-$NaYF_4$:Er^{3+} nanoparticles with 2% (**Figure 3.12**), 15% (**Figure 3.13**), and 50% (**Figure 3.14**) erbium dispersed in water were measured using a Edinburgh Instruments FLS920 fluorimeter with an excitation wavelength of 980 nm. The peaks at ~540 nm are from the $^4S_{3/2} \rightarrow {}^4I_{15/2}$ transitions and the peaks at ~650 nm are

from the $^4F_{9/2} \rightarrow {}^4I_{15/2}$ transitions. These are standard peaks for the upconversion process between ytterbium and erbium. However, these peaks can also be seen from erbium-only emission, and they can be seen in the β-$NaYF_4$:Er^{3+} nanoparticles before the cation exchange (**Figure 3.12-14**). The luminescence for all of the samples is quite low, which is expected as the samples are dispersed in water and water quenches luminescence. The samples are also very dilute which contributes to the low luminescence. Despite the lack of change in the luminescence spectra for the samples, this does not mean that the cation exchange failed. A cation exchange could still have occurred but the combination of low sample concentration and quenching by water could be masking the upconversion.

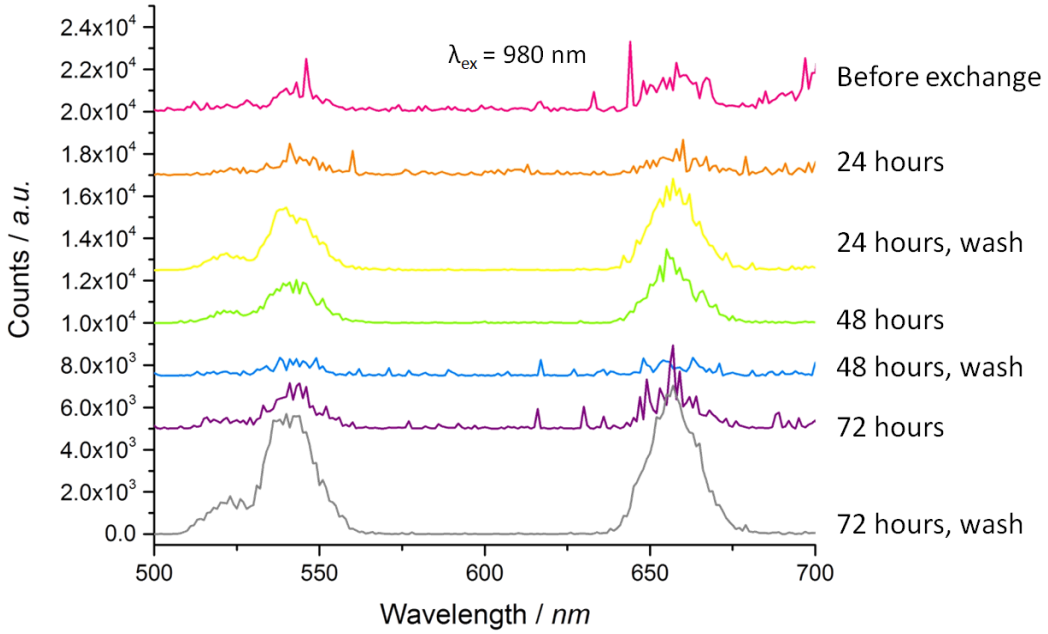

Figure 3.12—Emission spectra of β-$NaYF_4$:Er^{3+} (2%) nanoparticles dispersed in water before and after a cation exchange with Yb^{3+}.

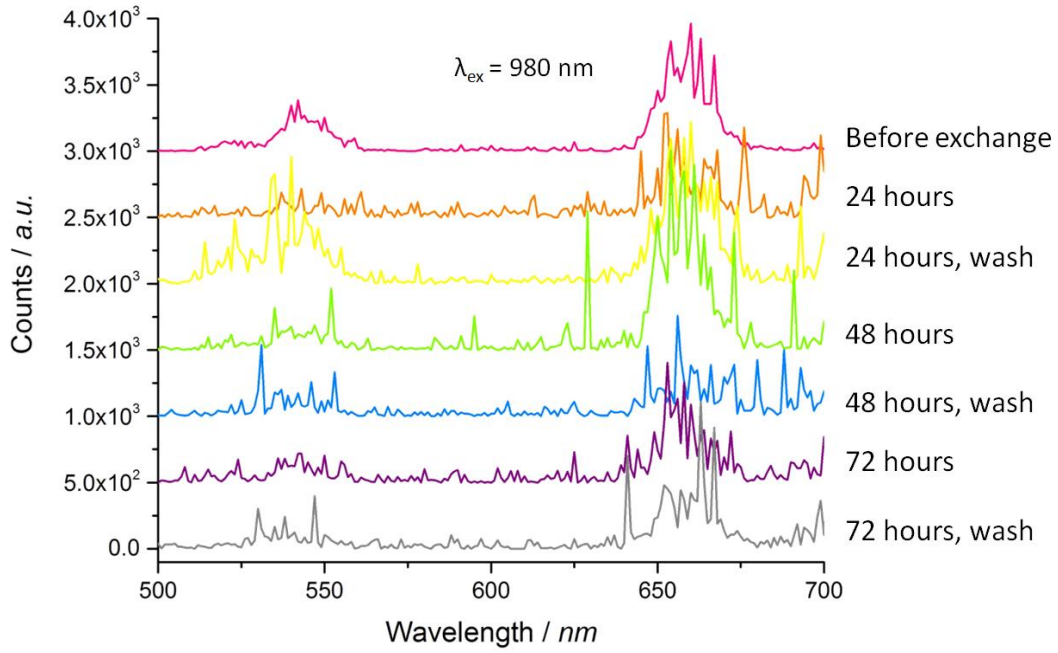

Figure 3.13—Emission spectra of β-$NaYF_4$:Er^{3+} (15%) nanoparticles dispersed in water before and after a cation exchange with Yb^{3+}.

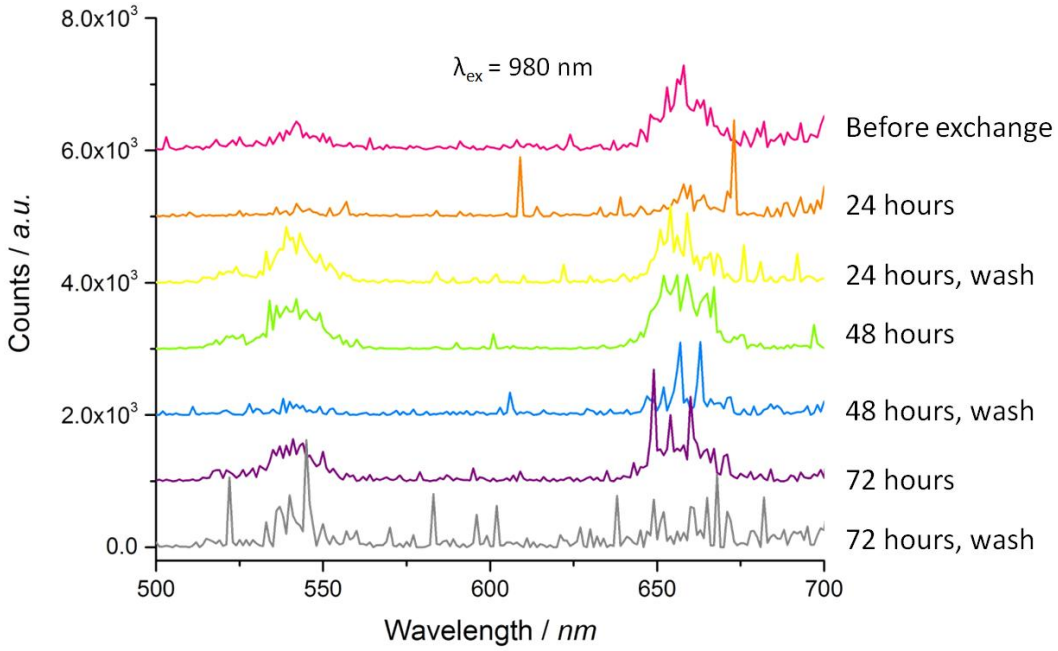

Figure 3.14—Emission spectra of β-$NaYF_4$:Er^{3+} (50%) nanoparticles dispersed in water before and after a cation exchange with Yb^{3+}.

3.3. Conclusions

The ultimate goal of this project was to use a cation exchange method to incorporate radioactive lanthanide cations into nanoparticles for use as a possible alternative to current radiative cancer therapies. Before radioactive materials were used, it was first necessary to prove that the exchange mechanism could take place across a barrier of ligands, such as the polyvinylpyrrolidone that coats the surface of the water dispersible β-$NaYF_3$:Yb^{3+}/Er^{3+} nanoparticles. After testing the cation exchange method on three samples of β-$NaYF_4$:Er^{3+} nanoparticles with 2%, 15%, and 50% erbium, the results indicate that a cation exchange is possible through a surface coating of PVP. The cations that will be exchanged out of the nanoparticles appear to depend on their initial concentrations. More cation exchange reactions of samples with initial erbium concentrations between 15% and 50% should be done to determine where this boundary lies.

3.4. Experimental Procedure

3.4.1. Chemicals

All lanthanide(III) chlorides ($YCl_3 \cdot 6H_2O$, $YbCl_3 \cdot 6H_2O$, $ErCl_3 \cdot 6H_2O$) (all ≥99.99%), oleic acid (90%), 1-octadecene (90%), ammonium fluoride (≥99.99%), polyvinylpyrrolidone (average molecular weight 10,000 g/mol), and hexanes (mixture of isomers, ≥98.5%) were purchased from Sigma-Aldrich. Sodium hydroxide and *N*,*N*-dimethylformamide (reagent grade) were purchased from Caledon. Methanol (HPLC grade) and dichloromethane (reagent grade) were purchased from EMD. Anhydrous ethyl alcohol was purchased from Commercial Alcohols. Ethyl ether was purchased from VWR. All chemicals were used as received.

3.4.2. Synthesis of oleate-stabilized β-$NaYF_4$:Er^{3+} nanoparticles

The synthesis of the $NaYF_3$:Er^{3+} nanoparticles was done as described in Chapter 2 with minimal changes. To a 100 ml 3-necked round bottom flask, 1 mmol of lanthanide chlorides (X mmol $YCl_3 \cdot 6H_2O$ and 1-X mmol $ErCl_3 \cdot 6H_2O$) was added, along with oleic acid (6 ml)and 1-octadecene (17 ml). The solution was then heated to 140 °C under vacuum with constant magnetic stirring. This temperature was held for 1 h to fully dissolve the salts and achieve a homogeneous solution. The solution was then cooled to room temperature. A solution of sodium hydroxide (2.5 mmol) and ammonium fluoride (4 mmol) dissolved in methanol (10 ml) was added to the 3-necked round bottom flask, and this mixture was stirred at room temperature for 1 h. The solution was then heated to 70 °C to allow the methanol to evaporate. A stream of argon was then introduced to the flask and the solution was heated to 300 °C. This temperature was held for 55 min. The solution was then cooled to room temperature. The nanoparticles were precipitated by adding anhydrous ethanol (23 ml) and centrifuging at 2,683 g forces (5,000 rpm, Beckman Coulter Spinchron 15 Series, F0850 rotor) for 5 min. The supernatant was removed and the resulting pellet was dispersed in a small volume of hexanes. Anhydrous ethanol (40 ml) was added, and the solution was centrifuged. The solution of nanoparticles was centrifuged a total of three times. Finally, the nanoparticles were dispersed in hexanes (10 ml).

3.4.3. Phase transfer of oleate-stabilized β-$NaYF_4$:Er^{3+} nanoparticles to water using polyvinylpyrrolidone (PVP)

The phase transfer of the above-made oleate-stabilized nanoparticles was done following a previously used method in the group.[15] To a 50 ml single-neck round bottom flask, PVP (300 mg) was added and dissolved in dichloromethane (5 ml) and *N*,*N*-

dimethylformamide (5 ml). An aliquot of the oleate-stabilized β-$NaYF_4$:Er^{3+} nanoparticles in hexanes (10 mg of nanoparticles) was added and the solution was magnetically stirred. The solution was heated to 80 °C and was allowed to reflux for 8 h. The solution was then cooled to room temperature, and was then left stirring overnight. The nanoparticles were precipitated by adding ethyl ether (60 ml) and centrifuging at 2,683 g forces (5,000 rpm, Beckman Coulter Spinchron 15 Series, F0850 rotor) for 5 min. The supernatant was removed and the resulting pellet was left to dry at room temperature for 4 h. Finally, the PVP-stabilized nanoparticles were dispersed in deionized water (2 ml).

3.4.4. Cation exchange of PVP-stabilized β-$NaYF_4$:Er^{3+} nanoparticles

The cation exchange of the above-made PVP-stabilized nanoparticles was done following a previously used method in the group.[15] Ytterbium(III) chloride hexahydrate (11x the total amount of Er and Y) was dissolved in deionized water (1 ml) in a 50 ml single-neck round bottom flask. The PVP-stabilized nanoparticles in water were added, the solution was stirred at 75 °C for 1 h, and was allowed to return to room temperature. The solution was then dialyzed for 72 h in total, first for 24 h using regenerated cellulose dialysis membranes (Spectra/Por® 7, Spectrum Labs, MWCO 25 kDa) and then for an additional 48 h using dialyzer tubes (D-Tube™ Dialyzer Maxi, EMD-Novagen, MWCO 6-8 kDa). The nanoparticles were also precipitated by adding acetone (1.5 ml) to the nanoparticle solution (0.1 ml) and centrifuging at 2,683 g forces (5,000 rpm, Beckman Coulter Spinchron 15 Series, F0850 rotor) for 10 min. The supernatant was removed and the nanoparticles were dispersed in water (0.1 ml).

3.4.5. Transmission Electron Microscope (TEM) images

A JEOL JEM-1400 microscope was used for all TEM images. An operating voltage of 80 kV was used. In order to prepare a sample for imaging, a diluted solution of the nanoparticles was drop cast onto the TEM grid (formvar carbon film on 300 mesh copper grids, 3 mm in diameter, from Electron Microscopy Sciences). Grids were dried in air before imaging. The embedded scale bar was calibrated against nanoparticles of a known size. The size distribution of the nanoparticles was measured by counting 100 nanoparticles. Sizes were measured using ImageJ software (version 1.48).

3.4.6. X-ray Diffraction (XRD) measurements

XRD patterns were obtained using a Rigaku Miniflex X-ray diffractometer with a chromium source (K_α λ = 2.2890 Å) operating at 30 kV and 15 mA. A sampling width of 0.05 ° (2θ) and a scan speed of 1 °/minute were used.

3.4.7. Steady state measurements

Steady state measurements were done using an Edinburgh Instruments FLS920 fluorimeter. The excitation source for these measurements was a JDS Uniphase 2-pin SMA connectorized 980 nm diode laser (L4 series) coupled to a 100 µm core fiber. Spectra for measurements done from 1500-1600 nm were collected using a liquid nitrogen-cooled Hamamatsu R5509 photomultiplier tube (PMT) detector. A short band-pass filter (1025 nm) was used on the emission side in order to remove any excitation light that had been scattered. Spectra for measurements done from 400-800 nm were collected using a Peltier-cooled Hamamatsu R928 photomultiplier tube (PMT) detector. A long band-pass filter (HO900 nm) was used on the collecting side of the detector in order to remove any excitation light that had been scattered. All measurements were

collected using a 1 nm resolution. The incident photon flux was kept at 300 W/cm^2. Measurements for all solutions were done in a quartz cuvette with a path length of 1 cm. All data was collected using Edinburgh Instruments F900 software (version 6.41).

3.4.8. Inductively–Coupled Plasma Mass Spectrometry (ICP-MS)

Analysis was completed using a Thermo X-Series II (X7) quadrupole ICP-MS to determine the Y^{3+}, Yb^{3+}, and Er^{3+} ion concentrations in the nanoparticle solutions

Samples were prepared by pipetting an aliquot of PVP-stabilized nanoparticles (50 μl) into a pre-weighed Teflon vial along with nitric acid (1 ml, 16N environmental grade). The final weight was recorded and the solution was then heated to 125 °C for at least 24 h. The cooled solution was quantitatively transferred into a pre-weighed high-density polyethylene (HDPE) bottle which was then filled with deionized (DI) water. The solution was completely mixed by inversion and the final weight was recorded. An aliquot of this diluted solution (1 ml) was then pipetted into a tared autosampler vial and the weight was recorded. Finally, the solution was diluted with nitric acid (10 ml, 2%) and was mixed by inversion.

Each sample was spiked with indium and rhenium to a concentration of ~7 ppb each. This was the internal standard which allows for the correction of signal drift and matrix effects. A standard reference material (SLRS-5) was used to confirm the accuracy of the analysis.

Chapter 4: Synchrotron Single Nanoparticle Elemental Analysis Using X-ray Absorption Spectroscopy

4.1. Introduction

4.1.1. Elemental Analysis of Nanoparticles

Quantifying the exact elemental composition of a sample is necessary for detecting the presence of impurities or for confirming the ratios of different elements. This is especially true for doped nanoparticles, where small changes in the concentration of the doping elements can drastically change the properties of the nanoparticles, such as doping $NaYF_4$ nanoparticles with Yb^{3+} and Er^{3+} to achieve green emission via upconversion. There are many techniques that can be used to determine the elemental make-up of a sample of nanoparticles but most, including inductively coupled plasma mass spectrometry (ICP-MS), are ensemble measurements.[17a] A few techniques are available to study the elemental composition of single nanoparticles, such as energy-dispersive X-ray spectroscopy (EDX, also known as EDS) and electron energy-loss spectroscopy (EELS).[17b, 17c] These techniques can be performed using a scanning transmission electron microscope (STEM),[67] however samples must be stable enough to withstand damage caused by the electron beam.

One excellent technique for elemental analysis is inductively coupled plasma mass spectrometry (ICP-MS). This method ionizes the sample and can scan for many elements concurrently. Measurements are quite quick as it only takes approximately 5 minutes to run one sample. ICP-MS is advantageous for nanoparticles, especially for those with low concentrations of other elements doped in, because it has detection limits below parts per trillion.

Another elemental analysis technique is energy-dispersive X-ray spectroscopy (EDX) on a scanning transmission electron microscope (STEM). EDX can be used for single-particle analysis. In EDX, an electron beam or X-ray beam interacts with the sample (**Figure 4.1**). The electrons in the incident electron beam excite the core electrons in the atoms of the sample causing them to be ejected from the core. At this point, an electron from an outer shell relaxes back down to the core, thereby emitting an X-ray that is characteristic of that atom. It is also possible for an electron to be emitted, carrying the excess energy in a radiationless process known as the Auger process.

These emitted X-rays are collected by a detector. It is possible to plot an elemental analysis map of an entire area of the sample of nanoparticles or to perform a line scan along a desired spot on the sample. Depending on the type of microscope that is being used, it can be possible to get some single nanoparticle analysis. One challenge that can arise during these types of measurements is that, as the characteristic X-rays can be emitted in any direction, the X-rays may not be collected efficiently by the detector. This can lead to slow collection of the signal. Samples with rough surfaces can amplify the randomness of the direction in which the characteristic X-rays are emitted.[68] This can increase the acquisition time of the measurements as it will take longer for the detector to collect enough counts to achieve a good signal to noise ratio. A less significant disadvantage of EDX is that it is historically better for heavy elements[69] than it is for lighter elements.

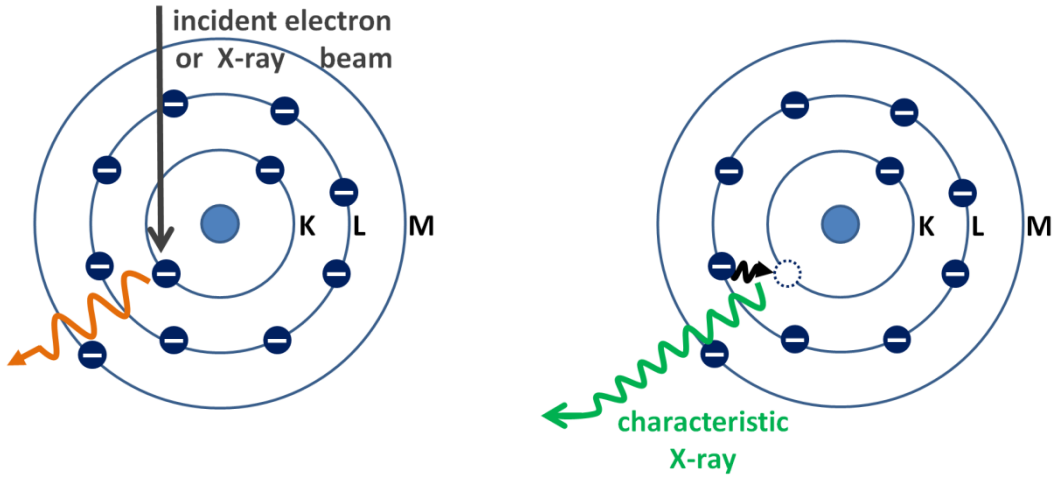

Figure 4.1—Energy dispersive X-ray spectroscopy (EDX). An incident beam of electrons or X-rays interacts with a core electron, thereby ejecting the core electron **(left)**. An electron from an outer shell in the ionized atom transitions into the empty core shell position (dashed circle), thereby emitting an X-ray characteristic of that element **(right)**.

Electron energy-loss spectroscopy (EELS) is another elemental analysis technique that can be done using a STEM. In EELS, the electron beam interacts with a sample, some electrons are inelastically scattered. The energy lost by these electrons directly corresponds to the characteristic absorption of the elements present in the sample. EELS is historically better for analyzing light elements.[69] In EELS, the peaks from the characteristic X-rays exhibit little peak overlap, whereas this can be quite severe in EDX.[70] It is possible to do EELS mapping and line scans. Perhaps the most important advantage is that EELS tends to have better spatial resolution than EDX[71] as EELS gives more intense peaks for different interfaces in the crystal structure. This allows for a more detailed characterization of nanoparticles.

While EDX and EELS both provide useful information about the chemical composition of nanoparticle samples, they require samples that can withstand damage from the electron beam. When the electron beam interacts with a sample, there is a transfer of

energy from the scattered electrons to the sample material.[72] If this energy is large enough, atomic nuclei in the sample can be displaced to, for instance, interstitial positions, leading to degradation of the crystalline structure. Hydrocarbon contamination can occur through a process called electron beam induced deposition.[72-73] Contaminants in the chamber are carried by the electron beam and deposited onto the sample, thereby obscuring the sample and distorting the image. Another type of damage especially relevant to the $NaLnF_4$ and LnF_3 nanoparticles is the radiolysis of the inorganic material in the sample. Alkali halides are very sensitive to radiation and the bombardment of the electron beam can lead to displacement of the halogen ions to create dislocations and eventual halogen loss.[74] It is also possible for the organic material, such as the ligands on the surface of the nanoparticles, to undergo radiolysis. Interactions with the electron beam can break bonds in the organic material or change its shape or position, leading to a loss of crystallinity which can appear as fading spots in the electron diffraction pattern.[75]

Previous EELS and EDX analysis done in our group involving $NaYF_4/NaGdF_4$ core/shell nanoparticles has shown substantial beam damage of the nanoparticles due to the long acquisition times required for performing gadolinium and yttrium line scans in EDX.[76] The beam damage caused by EELS was much less, however it was not possible to perform line scans for yttrium because the yttrium edge is too close to the gadolinium edge. High-angle annular dark-field (HAADF) measurements on the STEM have also shown significant beam damage for $NaYF_4/NaGdF_4$ core/shell nanoparticles at high magnification.[66c] This makes quantification of different elements challenging, as the beam can change the composition of the nanoparticles during the measurements, thereby changing the results.

There is yet to be a technique that provides highly accurate elemental analysis for single nanoparticles of a sensitive material. This is of interest because, even within the best samples of nanoparticles, a size distribution always exists. It has been reported that different lanthanides exhibit preferential shell growth on certain facets of the core nanoparticle surface.[29, 43, 76] Therefore, it is possible that the lanthanide dopant ions could preferentially order within the host material lattice. In order to answer this question, a technique that potentially exhibits high accuracy for single nanoparticle analysis without damaging the sample is necessary.

4.1.2. X-ray Absorption Spectroscopy (XAS)

X-ray absorption spectroscopy (XAS) is a technique that uses X-rays with tunable energies to excite the core electrons of a sample. Different edges are seen depending on which core electron is excited. For example, the K-edge corresponds to the excitation of the 1*s* electrons, the L-edge corresponds to the 2*s* and 2*p* electrons, and the M-edge corresponds to the 3*s* and 3*p* electrons. Each edge energy is characteristic of a particular element. Like in EDX and EELS, there can be some overlap of different peaks. However this is true of all elemental analysis techniques. Scanning transmission X-ray microscopy (STXM) is very similar to STEM, with the main difference being the use of an X-ray beam instead of an electron beam. This technique can give high spectral resolution and the spatial resolution is determined by the size of the X-ray beam.[77] Single-particle analysis could be possible if the diameter of the nanoparticles is larger than the best resolution of the beam. The beam damage from the X-ray beam is approximately two order of magnitude lower than the radiation caused by EELS.[78]

The three main regions of XAS (**Figure 4.2**) data are the X-ray Absorption Near-Edge Structure (XANES), Near-Edge X-ray Absorption Fine Structure (NEXAFS), and the Extended X-ray Absorption Fine Structure (EXAFS). XANES is typically used for elemental analysis, determining the formal oxidation state and coordination chemistry of the absorbing atom. NEXAFS and EXAFS give more useful information about the distances, coordination number, and species of the neighbours in the absorbing atom.

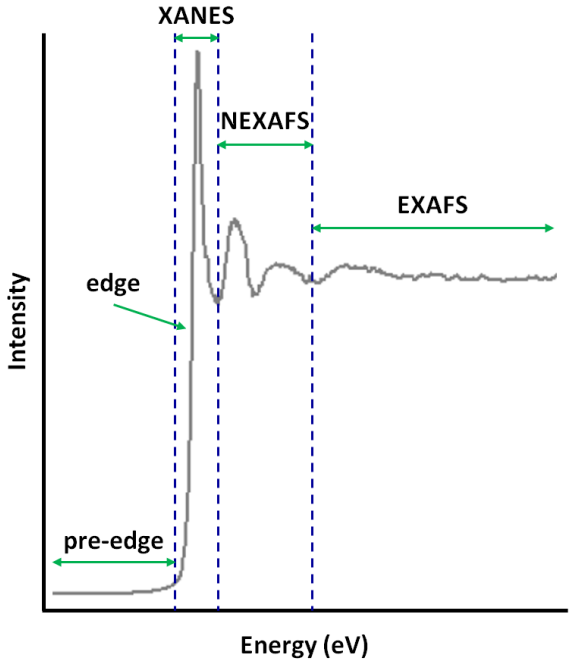

Figure 4.2—Example X-ray absorption spectroscopy (XAS) spectra illustrating the XANES, NEXAFS, and EXAFS regions.[79]

A synchrotron is needed to provide the necessary tunable X-ray beams to perform XAS measurements. A synchrotron is a cyclic particle accelerator. As a result of the high speed of the electrons moving around the synchrotron, every time the electrons change direction they emit energy, ranging from hard X-rays to far-infrared. These X-rays are

then directed down various beamlines to laboratory endstations equipped with different instruments for sample analysis at the atomic level.

Most of the world's synchrotrons can be found in Europe and Asia. There are also synchrotrons in the United States of America. Even closer to home, however, is a state of the art synchrotron in Canada, called the Canadian Light Source (CLS). The CLS is located in Saskatoon, Saskatchewan and was opened in 2005. The CLS has over 15 beamlines, several of which are equipped for XAS measurements.

X-ray absorption spectroscopy has been used for many different types of analysis in nanoparticles. There has been much in-situ studying of nanoparticle nucleation.[80] XAS has also been used to study the bonding of ruthenium in $RuCl_3$ nanoparticles[81] and to determine the coordination sphere of Au(III) in gold nanoparticles stabilized with glucosamine.[82] Scanning transmission X-ray microscopy (STXM) has been used to analyze many different types of nanoparticles. For example, ferric oxide nanoparticles that formed on chlorite surfaces were tested to determine whether they were homogeneous or heterogeneous,[83] and the structure of carbon nanotubes decorated with ruthenium nanoparticles was explored.[84] Most of the analysis of nanoparticles with XAS seems to involve ensemble measurements. To date, there has been little single-particle analysis using STXM or XAS[85].

4.1.3. Project Goals

There are two major requirements that must be met in order to analyze single nanoparticles using X-ray absorption spectroscopy. The first requirement is that the nanoparticles must be just larger than the best resolution of the X-ray beam being used for the measurements. As the best resolution of the X-ray beam at the CLS is ~25 nm,

nanoparticles must be larger than this, and ideally would be larger than 30 nm, to be able to be measured one nanoparticle at a time.

The second requirement is that the nanoparticles must be prepared for analysis in such a way that there is only a single layer of nanoparticles. This is necessary because the measured signal would otherwise not be representative of a single nanoparticle. If nanoparticles are stacked on top of each other, quantification would be impossible. This requirement can be achieved by drop casting the nanoparticle solution onto TEM grids and confirming the single layer using TEM.

4.2. Results and Discussion

4.2.1. Synthesis of oleate-stabilized β-$Na_{0.85}K_{0.15}YF_4$ and β-$NaYF_4$:Er^{3+} (50%) nanoparticles

Two different types of nanoparticles were chosen for analysis. $NaYF_4$ was chosen as it is one of the most common nanoparticles that we synthesize and it has been extensively characterized. This would be a suitable material to use as a calibration sample. The thickness of nanoparticles with only one lanthanide could be determined and then used as a comparison for samples with more than one lanthanide. Erbium was chosen as the dopant ion because the absorption peaks for erbium do not overlap with those from yttrium, allowing for clearer quantification. Once the undoped nanoparticles were measured, they could be used a reference against future doped samples. As the maximum uniform size that can be achieved for β-$NaYF_4$ nanoparticles is 18-20 nm, some potassium was added to the undoped nanoparticles as a way to stretch the lattice minimally[86] in order to achieve nanoparticles that are suitable in size for analysis at the CLS.

β-$Na_{0.85}K_{0.15}YF_4$ nanoparticles and β-$NaYF_4$:Er^{3+} (50%) nanoparticles were synthesized by dissolving the appropriate amounts of yttrium and erbium chloride salts in a mixture of oleic acid and 1-octadecene.[43] This solution was then mixed with a solution of sodium hydroxide (and potassium hydroxide in the case of the undoped nanoparticles) and ammonium fluoride in methanol and was then heated to 300 °C for 1 h. The resulting nanoparticles can be seen in **Figure 4.3**.

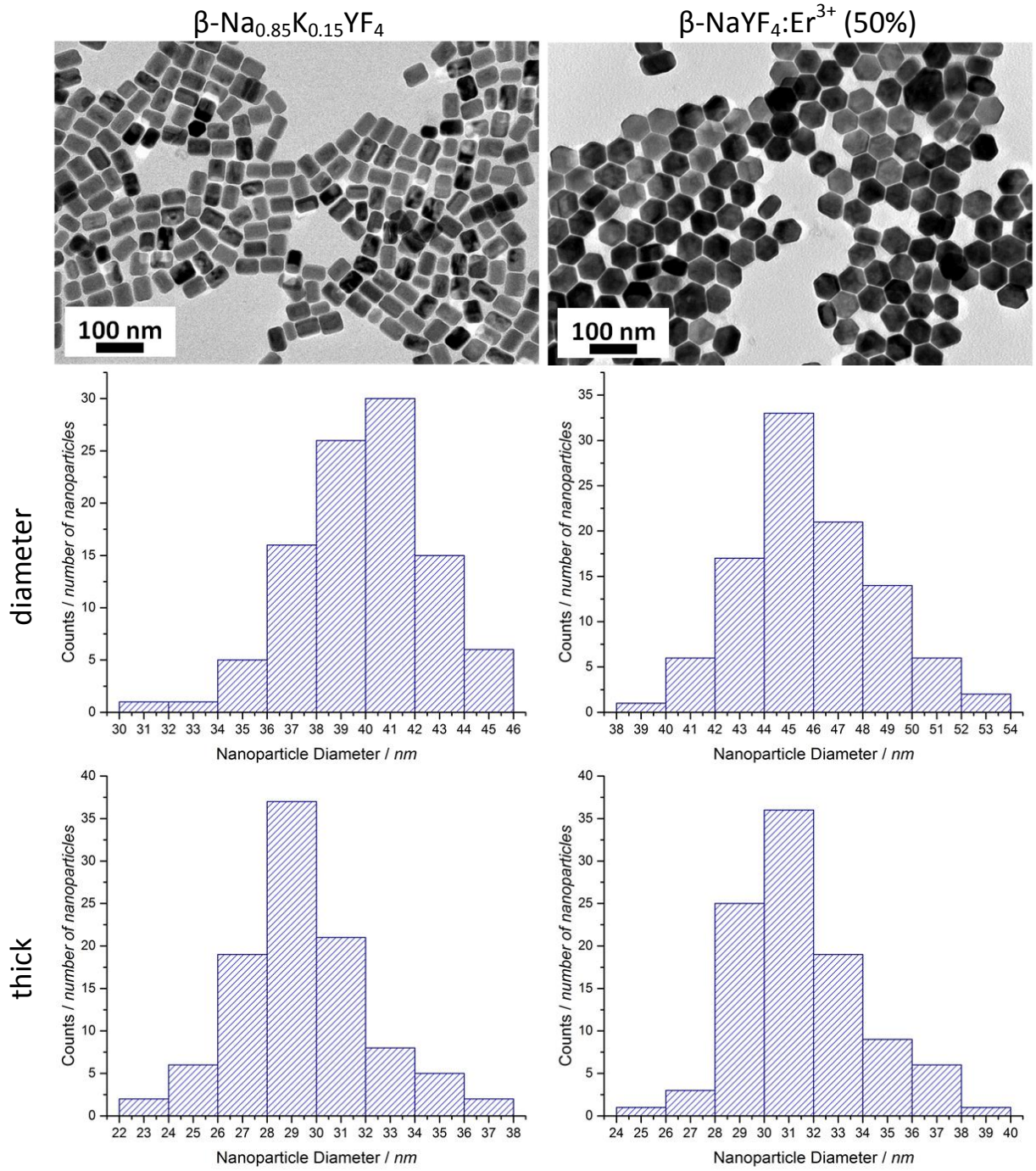

Figure 4.3—TEM images of β-$Na_{0.85}K_{0.15}YF_4$ nanoparticles and β-$NaYF_4$:Er^{3+} (50%) nanoparticles dispersed in hexanes. The size distributions show that the β-$Na_{0.85}K_{0.15}YF_4$ nanoparticles are ~40 nm in diameter and ~29 nm thick, while β-$NaYF_4$:Er^{3+} (50%) nanoparticles are ~45-46 nm in diameter and ~31 nm thick.

The average diameter of the β-$Na_{0.85}K_{0.15}YF_4$ nanoparticles in hexanes is 39.9 nm with a standard deviation of 2.7 nm and the average thickness is 29.4 nm with a standard

deviation of 2.7 nm. The average diameter of the β-$NaYF_4$:Er^{3+} (50%) nanoparticles in hexanes is 45.9 nm with a standard deviation of 2.7 nm and the average thickness is 31.5 nm with a standard deviation of 2.5 nm. The diameter of the hexagonal nanoparticles was measured between opposing flat edges.

The nanoparticles were also analyzed using powder X-ray diffraction (**Figure 4.4**). The peaks of both samples are in close agreement with the reference peaks for bulk β-$NaYF_4$ (JCPDS #00-016-0334), which confirms the formation of β-$NaYF_4$.

When the peaks widths of the β-$Na_{0.85}K_{0.15}YF_4$ nanoparticles and β-$NaYF_4$:Er^{3+} (50%) samples were analyzed, the average sizes of the nanoparticles were found to be between 25-40 nm for both samples. These results correspond with the sizes determined from the TEM images.

The peaks around 26 °, 46 °, 67 °, 81 °, 83 °, 84 °, 87 °, and 99 ° are slightly broader than those at 45 °, 52 °, 60 °, and 72 °. They are also broader than would be expected due to increasing 2θ values. This supports the presence of the ~40 nm x ~30 nm thick nanoparticles.

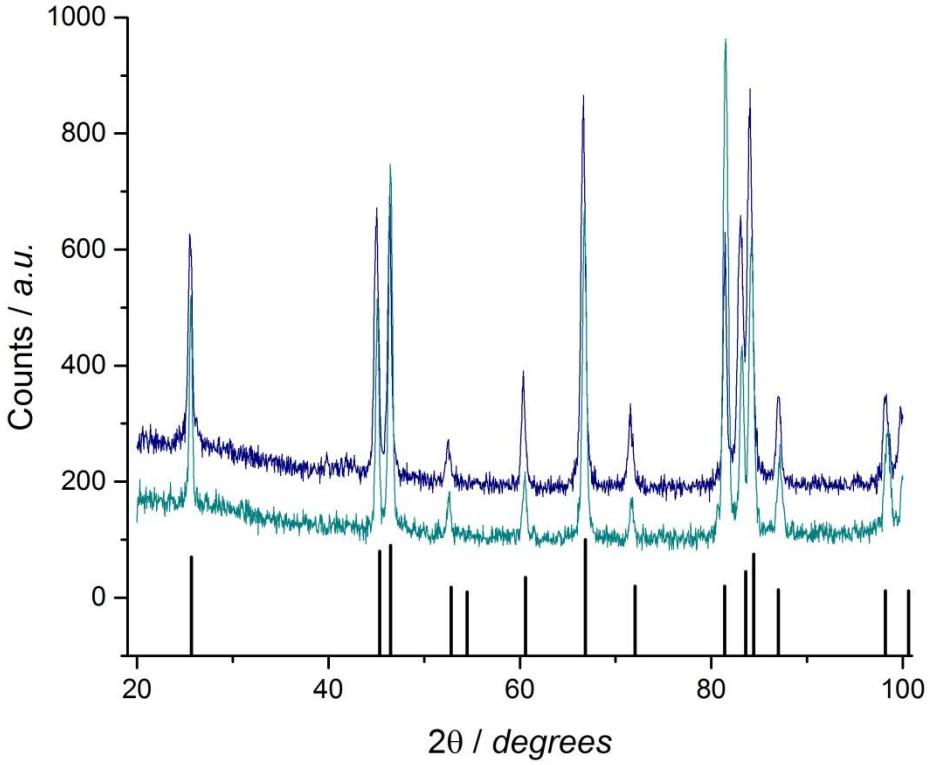

Figure 4.4—XRD of $Na_{0.85}K_{0.15}YF_4$ nanoparticles and $NaYF_4:Er^{3+}$ (50%) nanoparticles with reference β-$NaYF_4$ (reference #00-016-0334).

The samples were then transferred to water (**Figure 4.5**) in order to run ICP-MS to confirm the concentrations of lanthanides present. As was expected, there was found to be 100% yttrium in the β-$Na_{0.85}K_{0.15}YF_4$ nanoparticle sample and 53.9% yttrium and 46.1% erbium in $NaYF_4:Er^{3+}$ (50%) nanoparticle sample.

The average diameter of the β-$Na_{0.85}K_{0.15}YF_4$ nanoparticles in water is 40.3 nm with a standard deviation of 2.2 nm and the average thickness is 28.5 nm with a standard deviation of 2.4 nm. The average diameter of the β-$NaYF_4:Er^{3+}$ (50%) nanoparticles in water is 47.4 nm with a standard deviation of 2.6 nm and the average thickness is 33.2 nm with a standard deviation of 2.5 nm. These size distributions are very similar to those of the nanoparticles dispersed in hexanes.

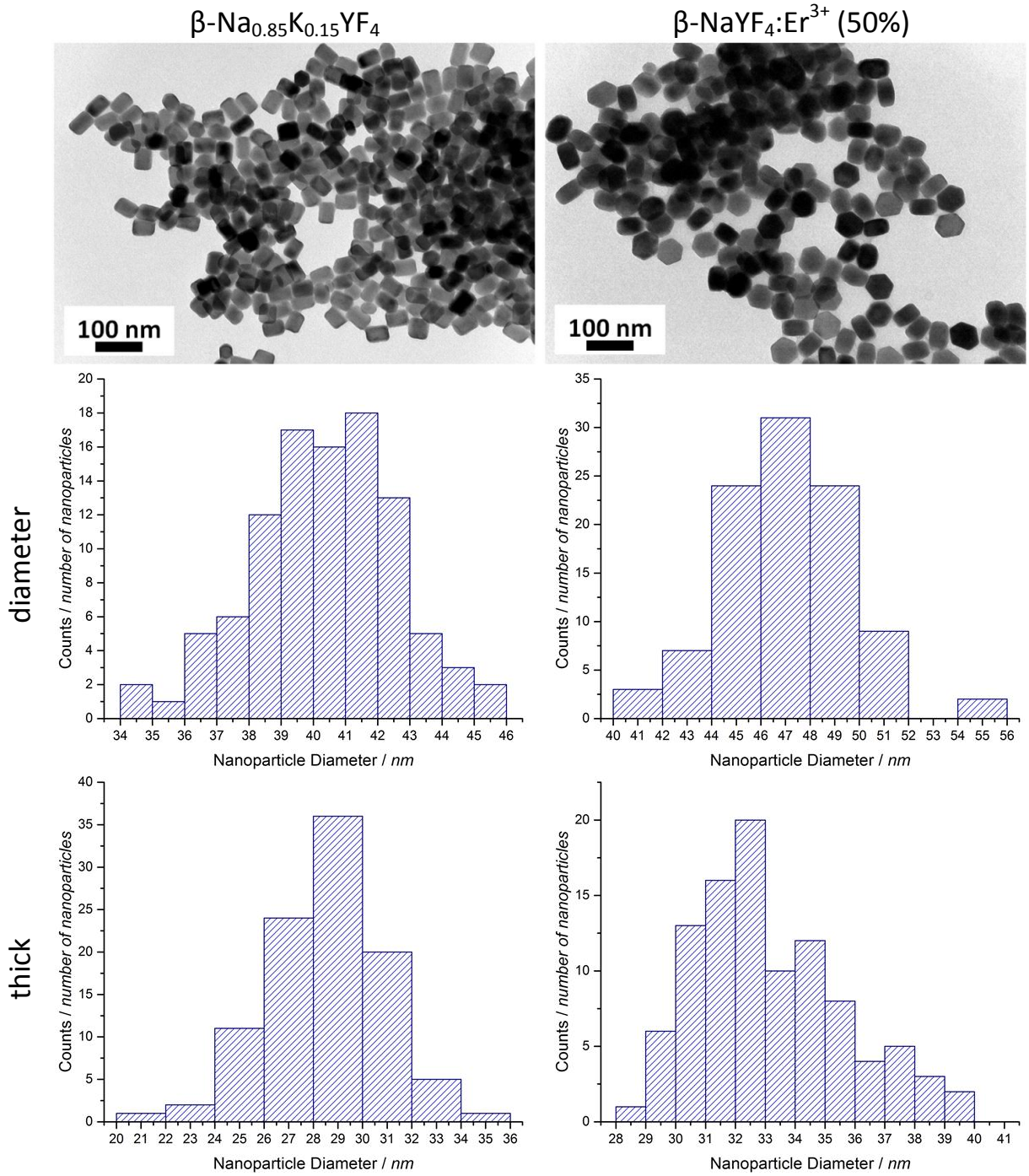

Figure 4.5—TEM images of $NaYF_4$ nanoparticles and $NaYF_4:Er^{3+}$ (50%) nanoparticles dispersed in water. The size distributions show that the $NaYF_4$ nanoparticles are ~41 nm in diameter and ~29 nm thick, while $NaYF_4:Er^{3+}$ (50%) nanoparticles are ~47 nm in diameter and ~32-33 nm thick.

4.2.2. XAS data for the β-$NaYF_4$:Er^{3+} (50%) nanoparticles

XAS measurements were run on the scanning transmission X-ray microscopy (STXM) endstation of the Spectromicroscopy (SM) beamline. Samples were prepared by drop-casting a diluted solution of nanoparticles onto a TEM grid. Once the presence of monolayers was confirmed using TEM, the same diluted solution was used to prepare fresh grids. These grids were shipped without being imaged using TEM to avoid any possible beam damage to the nanoparticles.

In order to interpret any data, the thickness of the sample must be known. This can be determined by measuring the sample twice, once "on-resonance" and then again "off-resonance" with respect to the desired edge. The two images are then combined to give a difference in absorption, which is directly related to the thickness of the sample. **Figure 4.6** shows the on- and off-resonance images for the F K-edge, as well as the F image difference map for a monolayer of nanoparticles.

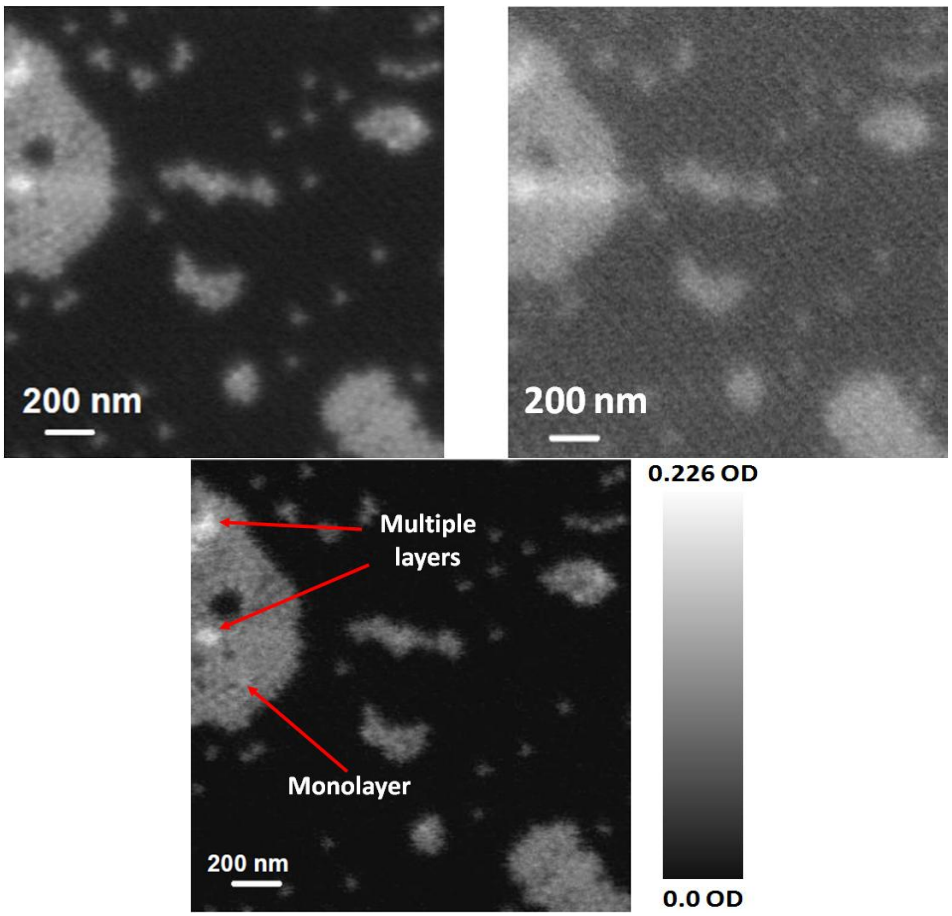

Figure 4.6—XAS image of the F 1s K-edge for β-$NaYF_4$:Er^{3+} (50%) nanoparticles. The "on-resonance" image was obtained by scanning at 690.5 eV **(top, left)**, the "off-resonance" image was obtained by scanning at 680 eV **(top, right)**. The F image difference map **(bottom)** can be seen along with the optical density (OD) gradient.

From the F image difference map of the β-$NaYF_4$:Er^{3+} (50%) nanoparticles (**Figure 4.6**), it is possible to resolve individual nanoparticles. These nanoparticles are approximately 40 nm in diameter, similar to what is observed in the TEM, and the hexagonal packing is indicative of a monolayer.

These images express thickness in terms of optical density (OD), which is simply the natural logarithm of the ratio of incident radiant power to transmitted radiant power. In order to determine the thickness of the sample from the image, the optical density needs

to be converted to thickness. This is done by applying a mask to the image that excludes any pixels in the image that are outside a certain optical density range. The areas of interest are the regions of the grid that appear to be a monolayer of nanoparticles. Pixels with an optical density greater than 0.15 were excluded as they were deemed to represent parts of the grid with more than a monolayer. Pixels with an optical density of less than 0.045 were also excluded as they were considered to be noise. The estimated thickness of the nanoparticles can then be divided by the mean optical density of the pixels to get a ratio of nanometers (thickness) to optical density. When this method was applied to the F K-edge image, a mean size of 31.1 nm with a standard deviation of 8.5 nm was measured. This is in excellent agreement with the measured thickness of 33.2 nm ± 2.5 nm using the TEM.

When this spectral fitting was applied to the data for the monolayer of β-$NaYF_4$:Er^{3+} (50%) nanoparticles, different thicknesses were calculated for the F K-edge and Er M_5-edge (**Figure 4.7**, **Table 4.1**).

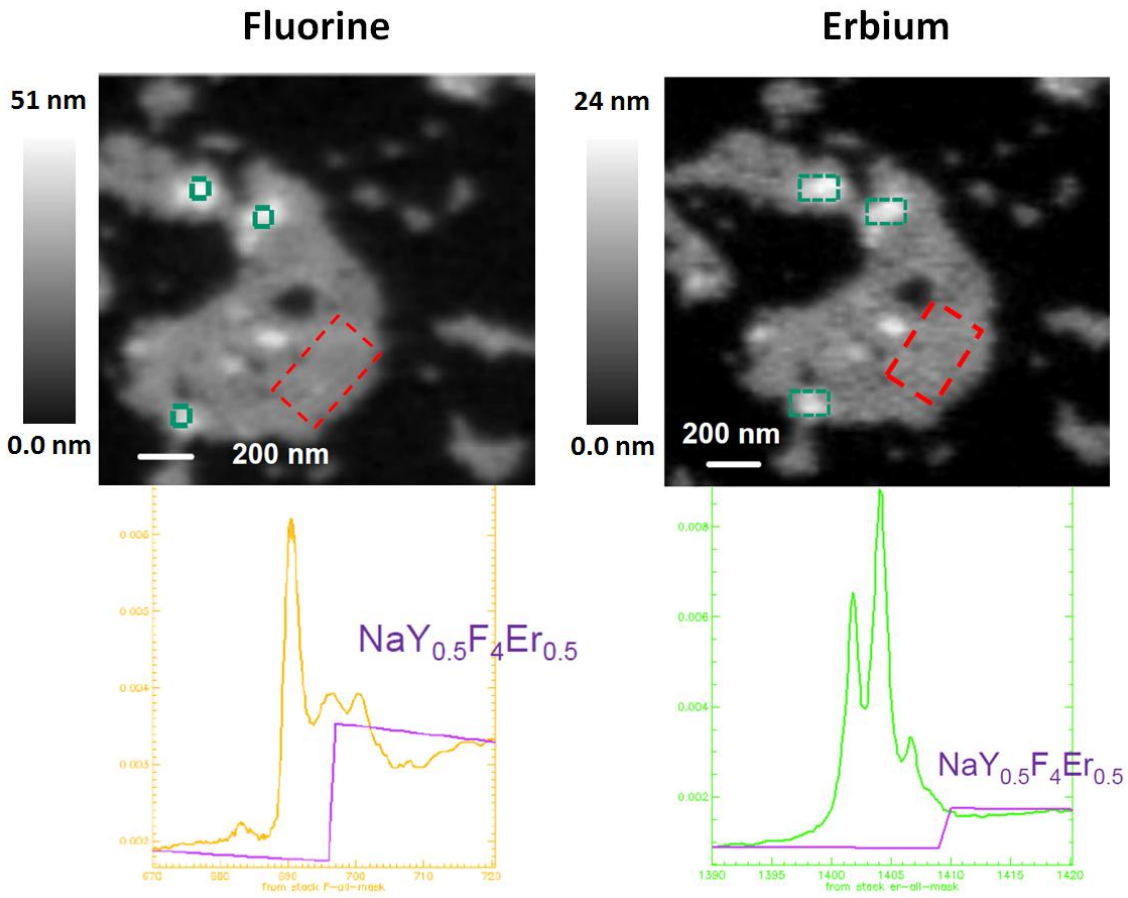

Figure 4.7—Difference maps **(top)** and XAS spectra (bottom) for the 1s K-edge of fluorine and the 3d M_5-edge of erbium in β-$NaYF_4$:Er^{3+} (50%) nanoparticles. The x-axis of the spectra is energy (eV) and the y-axis is optical density.

Table 4.1—Average thickness of the pixels in the monolayer region (red rectangle) for the K-edge of fluorine and the M_5-edge of erbium for β-$NaYF_4$:Er^{3+} (50%) nanoparticles, as corresponds to **Figure 4.7**.

K-edge	Area (pixels)	Average thickness (nm)	Standard deviation (nm)
F	115	25.7	1.50
Er	246	12.1	1.25

At first glance, the thickness of the nanoparticles appears to be different for the different elements. For the F K-edge, the monolayer thickness was found to be ~25 nm thick. This is similar to the ~30 nm thickness that was measured using the TEM. The Er M_5-edge was measured to be ~12 nm thick. As there is only 50% erbium in the nanoparticles, this values represents "half of the thickness" of the nanoparticles. Therefore, the measured thickness should be doubled to get the true thickness of the nanoparticles. This 24 nm is in good agreement with the measured thickness of 25 nm at the F K-edge.

The thicker regions presented in green in **Figure 4.7** could either be parts of the grid that had multiple layers stacked on top of each other or that had nanoparticles laying on their side. The lower half of **Figure 4.7** shows the experimental stack maps overlaid with the theoretical edge jump for the K- and M_5-edges. This theoretical edge jump is the amount of energy required to excite a core electron. The match between the theoretical and experimental pre- and post-edges is not very good for fluorine. This could be improved by collecting the spectra over a longer energy range to better extrapolate the data and achieve a better fit.

4.3. Conclusions

A potential new method for carrying out single nanoparticle elemental analysis on electron beam sensitive samples was explored. β-$Na_{0.85}K_{0.15}YF_4$ and β-$NaYF_4$:Er^{3+} (50%) nanoparticles that were larger than the best resolution of the X-ray beam were made and sent to the Canadian Light Source in Saskatoon for X-ray absorption spectroscopy. Using XAS, it is possible to resolve individual nanoparticles,

and their thickness was determined to be ~25 nm thick. This is very close to the measured thickness from the TEM. Overall, these results are extremely encouraging.

The most challenging aspect of this project is converting the optical density scale to a thickness scale using the pre- and post- K- and M_5-edge intensities. This could be improved by using longer acquisition times and by collecting the data over a longer energy range. This would also improve the match between the measured edges and the theoretical edge jump. Once the yttrium edge has been measured for the β-$NaYF_4$:Er^{3+} (50%) nanoparticles, the yttrium edge for the β-$Na_{0.85}K_{0.15}YF_4$ nanoparticles should be measured to determine the accuracy of the measurements for the β-$NaYF_4$:Er^{3+} (50%) nanoparticles. As these initial results are very promising, samples with lower percent doping should be synthesized, sent to the CLS, and analyzed to test the sensitivity of the technique.

4.4. Experimental Procedure

4.4.1. Chemicals

All lanthanide(III) chlorides ($YCl_3 \cdot 6H_2O$, $ErCl_3 \cdot 6H_2O$) (all ≥99.99%), oleic acid (technical grade, 90%), 1-octadecene (technical grade, 90%), ammonium fluoride (≥99.99%), polyvinylpyrrolidone (average molecular weight 10,000 g/mol), and hexanes (mixture of isomers, ≥98.5%) were purchased from Sigma-Aldrich. Sodium hydroxide and *N*,*N*-dimethylformamide (reagent grade) were purchased from Caledon. Methanol (HPLC grade) and dichloromethane (reagent grade) were purchased from EMD. Anhydrous ethyl alcohol was purchased from Commercial Alcohols. Ethyl ether was purchased from VWR. All chemicals were used as received.

4.4.2. Synthesis of oleate-stabilized β-$Na_{0.85}K_{0.15}YF_4$ and β-$NaYF_4$:Er^{3+} (50%) nanoparticles

The synthesis of the β-$Na_{0.85}K_{0.15}YF_4$ and β-$NaYF_4$:Er^{3+} (50%) nanoparticles were done as described in Chapters 2 and 3 with minimal changes. To a 100 ml 3-necked round bottom flask, 1 mmol of lanthanide chlorides (either 1 mmol $YCl_3 \cdot 6H_2O$ OR 0.50 mmol $YCl_3 \cdot 6H_2O$ and 0.50 mmol $YbCl_3 \cdot 6H_2O$) was added, along with oleic acid (6 ml) and 1-octadecene (17 ml). The solution was then heated to 140 °C under vacuum with constant magnetic stirring. This temperature was held for 1 h to fully dissolve the salts and achieve a homogeneous solution. The solution was then cooled to room temperature. For the nanoparticles without potassium, a solution of sodium hydroxide (2.5 mmol) and ammonium fluoride (4 mmol) was dissolved in methanol (10 ml). For the nanoparticles with potassium, the only deviation from the standard procedure was that the amount of sodium hydroxide (2.125 mmol) was reduced slightly and a small amount of potassium hydroxide (0.375 mmol) was added. This methanol solution was added to the 3-necked round bottom flask, and the mixture was stirred at room temperature for 1 h. The solution was then heated to 70 °C to allow the methanol to evaporate. A stream of argon was then introduced to the flask and the solution was heated to 300 °C. This temperature was held for 55 min. The solution was then cooled to room temperature. The nanoparticles were precipitated by adding anhydrous ethanol (23 ml) and centrifuging at 2,683 g forces (5,000 rpm, Beckman Coulter Spinchron 15 Series, F0850 rotor) for 5 min. The supernatant was removed and the resulting pellet was dispersed in a small volume of hexanes. Anhydrous ethanol (40 ml) was added, and the solution was centrifuged at the same settings as previously described. This washing step was repeated

so that the solution of nanoparticles were centrifuged a total of three times. Finally, the nanoparticles were dispersed in hexanes (10 ml).

4.4.3. Phase transfer of oleate-stabilized β-$NaYF_4$:Er^{3+} nanoparticles to water using polyvinylpyrrolidone (PVP)

The phase transfer of the above-made oleate-stabilized nanoparticles was done as described in Chapter 3. To a 50 ml single-neck round bottom flask, PVP (300 mg) was added and dissolved in dichloromethane (5 ml) and *N*,*N*-dimethylformamide (5 ml). An aliquot of the oleate-stabilized β-$NaYF_4$:Er^{3+} nanoparticles in hexanes (10 mg of nanoparticles) was added and the solution was magnetically stirred. The solution was heated to 80 °C and was allowed to reflux for 8 h. The solution was then cooled to room temperature, after which it was left stirring overnight. The nanoparticles were precipitated by adding ethyl ether (60 ml) and centrifuging at 2,683 g forces (5,000 rpm, Beckman Coulter Spinchron 15 Series, F0850 rotor) for 5 min. The supernatant was removed and the resulting pellet was left to dry at room temperature for 4 h. Finally, the PVP-stabilized nanoparticles were dispersed in deionized water (2 ml).

4.4.4. Transmission Electron Microscope (TEM) images

A JEOL JEM-1400 microscope was used for all TEM images. An operating voltage of 80 kV was used. In order to prepare a sample for imaging, a diluted solution of the nanoparticles was drop cast onto the TEM grid (formvar carbon film on 300 mesh copper grids, 3 mm in diameter, from Electron Microscopy Sciences). Grids were dried in air before imaging. The embedded scale bar was calibrated against nanoparticles of a known size. The size distribution of the nanoparticles was measured by counting 100 nanoparticles. Sizes were measured using ImageJ software (version 1.48).

4.4.5. X-ray Diffraction (XRD) measurements

XRD patterns were obtained using a Rigaku Miniflex X-ray diffractometer with a chromium source (K_α λ = 2.2890 Å) operating at 30 kV and 15 mA. A sampling width of 0.05 ° (2θ) and a scan speed of 1 °/minute were used.

4.4.6. Inductively–Coupled Plasma Mass Spectrometry (ICP-MS)

Analysis was completed using a Thermo X-Series II (X7) quadrupole ICP-MS to determine the Y^{3+} and Er^{3+} ion concentrations in the nanoparticle solutions

Samples were prepared by pipetting an aliquot of PVP-stabilized nanoparticles (50 µl) into a pre-weighed Teflon vial along with nitric acid (1 ml, 16N environmental grade). The final weight was recorded and the solution was then heated to 125 °C for at least 24 h. The cooled solution was quantitatively transferred into a pre-weighed high-density polyethylene (HDPE) bottle which was then filled with deionized (DI) water. The solution was completely mixed by inversion and the final weight was recorded. An aliquot of this diluted solution (1 ml) was then pipetted into a tared autosampler vial and the weight was recorded. Finally, the solution was diluted with nitric acid (10 ml, 2%) and was mixed by inversion.

Each sample was spiked with indium and rhenium to a concentration of ~7 ppb each. This was the internal standard which allows for the correction of signal drift and matrix effects. A standard reference material (SLRS-5) was used to confirm the accuracy of the analysis.

4.4.7. X-Ray Absorption Spectroscopy (XAS)

Measurements were done by Dr. J. Dynes, the Research Associate at the CLS for the SM beamline, using scanning transmission X-ray microscopy (STXM) on the

Spectromicroscopy (SM) (101D-1) beamline at the Canadian Light Source. Using the incident flux measured through regions of the TEM grid that had no sample, the as-measured images were converted to optical density (OD) images. Image difference maps were collected at the F K-edge and the Er M_5-edge for the same area of nanoparticles. For the F K-edge difference maps, the off-resonance image was collected at 690.5 eV and the on-resonance image was collected at 675.0 eV. For the Er M_5-edge, the off- and on-resonance images were collected at 1404.9 eV and 1395.5 eV, respectively. All image difference maps were collected at a pixel size of 5 x 5 nm^2 for either a 0.044 μm^2 (F K-edge) or 0.092 μm^2 (Er K-edge) area. All spectra were collected from low to high energy.

Chapter 5: Conclusions and Future Directions

In conclusion, this thesis presents two different potential applications and a possible new method, at the single nanoparticle level, of characterization for lanthanide-based nanoparticles. Each of these three experimental chapters starts from a colloidal synthesis point of view aiming at making monodisperse nanoparticles with varying properties.

Chapter 1 presents a brief overview of lanthanides and explores their ability to undergo luminescence and upconversion. Upconversion of Ln^{3+}-based (nano)materials is generally a non-linear multiphoton absorption process where two or more photons with lower energy are combined to form one photon with a higher energy. This luminescence and upconversion means that lanthanide nanoparticles can emit in the visible and NIR range, making them attractive for many different applications.

Chapter 2 explores the possibility of using β-LaF_3:Nd^{3+} (5%) nanoparticles in a colloidal laser to overcome the issues that solid state lasers face due to thermal effects. In an ideal colloidal laser, the nanoparticles dispersed in solution would be small enough to avoid scattering the laser beam. The emission wavelength of the colloidal laser would be equal to that of some solid state lasers so that it could be a suitable replacement, and the lifetime of that emission should be long enough to establish a population inversion in the lasing material. Finally, the nanoparticles could be dispersed in a liquid with a high boiling point so that the solution would not evaporate during the lasing process.

Neodymium in the form of Nd^{3+} is an appropriate choice for these nanoparticles as it emits at a wavelength of 1064 nm, the same as that used by many solid state lasers. The lanthanum fluoride nanoparticles are sufficiently small enough to avoid any unwanted scattering. The average lifetimes of the nanoparticles were ~97 μs, close to the 100 μs

goal. Finally, the nanoparticles were dispersed into 1-octadecene, a solvent with a high boiling point. This would allow for the dissipation of heat from the excited nanoparticles without evaporating the solution and compromising the stability of the liquid lasing material. Only the concentration of the dispersion remains a challenge. The dispersion would ideally be crystal clear to avoid any scattering yet have a high concentration of nanoparticles. However, while diluting the solution improves the clarity, the overall concentration of neodymium cations in the solution decreases, thereby decreasing the potency of the colloidal laser. This could be resolved by increasing the amount of neodymium loaded into each nanoparticle, however this could have the adverse effect of the neodymium ions quenching themselves through proximity quenching. The cloudy effect could also possibly be resolved by dispersing the nanoparticles in a different high boiling point liquid. While more research needs to be done, this seems to be a feasible route. Once the concentration of the lasing solution has been resolved, the nanoparticles should be tested by our collaborators in a colloidal lasing set up.

In Chapter 3, a cation exchange of ytterbium for yttrium and erbium in water-dispersible β-$NaYF_4$:Er^{3+} nanoparticles across a polyvinylpyrrolidone (PVP) surface coating was tested as a possible synthesis route for radioactive nanoparticles. The synthesis of water-dispersible nanoparticles that have been labeled with antibodies to make the nanoparticles cancer cell specific is a multi-step process. If the nanoparticles were made to be radioactive, they could theoretically be used as a radiative cancer therapy. Incorporating the radioactive material into nanoparticles at the very end of the synthesis would minimize the researchers contact with the radioactively “hot” materials. The idea of using upconverting nanoparticles was to have an optical indication of a

successful cation exchange. While no upconversion was observed in the post-cation exchange samples as compared to the pre-cation exchange samples, for which possible explanations have been given, ICP-MS confirms that ytterbium was present after the cation exchange. After 72 h of dialysis the nanoparticles still contained a similar ratio of ytterbium as before the dialysis. This suggests that the cation exchange was a success. The cation exchange could now be tried using non-radioactive, or "cold", isotopes of the desired radioactive lutetium and yttrium. It would be quite challenging to prove the exchange of yttrium in $NaYF_4$ nanoparticles for "cold" yttrium as they would appear identical through most analytical techniques, however the results from this chapter suggest that the newly added "cold" yttrium should exchange for the yttrium already in the nanoparticles. If the "cold" experiments are successful, the next step would be to move on to the "hot" materials: lutetium-177 and yttrium-90.

Finally, Chapter 4 presents the use of β-$Na_{0.85}K_{0.15}YF_4$ nanoparticles and β-$NaYF_4$:Er^{3+} (50%) nanoparticles for single-particle analysis using X-ray absorption spectroscopy (XAS) in order to better quantify the amount of different lanthanides in individual nanoparticles. An X-ray beam can be used to avoid the significant beam damage that can occur during the long acquisition times for some elemental analysis using an electron beam in a STEM. Nanoparticles that were larger than the best resolution of the XAS beam were made and were sent to the Canadian Light Source in Saskatoon. It is possible to resolve individual nanoparticles using the X-ray beam. The nanoparticles were determined to be ~25 nm thick, which is in good agreement to the measured 30 nm in the TEM. The signal to noise ratio was a little high which made the conversion from the optical density of the sample to thickness somewhat challenging.

This could be improved by collecting data over a longer energy range and by measuring during longer acquisition times. Samples with lower percent doping should be synthesized to test the sensitivity limits of XAS for small concentrations of doped lanthanides.

Bibliography

1. Moeller, T., *The Chemistry of the Lanthanides*. Reinhold Publishing Corp: New York, 1963.

2. Cotton, S., *Lanthanides and Actinides*. 1st ed.; Macmillan Education Ltd: Basingstoke, 1991.

3. Hughes, I. D.; Däne, M.; Ernst, A.; Hergert, W.; Luders, M.; Poulter, J.; Staunton, J. B.; Svane, A.; Szotek, Z.; Temmerman, W. M., Lanthanide Contraction and Magnetism in the Heavy Rare Earth Elements. *Nature* **2007,** *446* (7136), 650-653.

4. Haynes, W. M.; Bruno, T. J.; Lide, D. R., *CRC handbook of chemistry and physics*. 95th, Internet version ed.; CRC Press: Boca Raton, Florida, 2014.

5. Chakhmouradian, A. R.; Wall, F., Rare Earth Elements: Minerals, Mines, Magnets (and More). *Elements* **2012,** *8* (5), 333-340.

6. (a) Aime, S.; Castelli, D. D.; Crich, S. G.; Gianolio, E.; Terreno, E., Pushing the Sensitivity Envelope of Lanthanide-Based Magnetic Resonance Imaging (MRI) Contrast Agents for Molecular Imaging Applications. *Accounts of Chemical Research* **2009,** *42* (7), 822-831; (b) Kilbourn, B. T., The Role of the Lanthanides in Applied Catalysis. *Journal of the Less-Common Metals* **1986,** *126*, 101-106.

7. Stein, G.; Würzberg, E., Energy Gap Law in the Solvent Isotope Effect on Radiationless Transitions of Rare Earth Ions. *The Journal of Chemical Physics* **1975,** *62* (1), 208-213.

8. Turro, C.; Fu, P. K.-L.; Bradley, P. M., Lanthanide Ions as Luminescent Probes of Proteins and Nucleic Acids. *Metal ions in biological systems* **2003,** *40*, 323-354.

9. Lackowicz, J. R., *Principles of Fluorescence Spectroscopy*. Third ed.; Springer: Baltimore, MD, 2006.

10. Sivakumar, S. Lanthanide-Doped Nanoparticles in Sol-Gel Matrices: Improved Optical Properties and New Opportunities. University of Victoria, 2006.

11. Chen, H. J.; Huang, H.; Huang, X. W.; Clifrord, J. N.; Forneli, A.; Palomares, E.; Zheng, X. Y.; Zheng, L. P.; Wang, X. Y.; Shen, P.; Zhao, B.; Tan, S. T., High Molar Extinction Coefficient Branchlike Organic Dyes Containing Di(p-tolyl)phenylamine

Donor for Dye-Sensitized Solar Cells Applications. *Journal of Physical Chemistry C* **2010,** *114* (7), 3280-3286.

12. Nd:YAG Rods. http://directedlight.com/laser-components/catalog/nd-yag-rods/ (accessed September 4, 2015).

13. Krupke, W. F., Radiative Transition Probabilities Within the 4f Ground Configuration of Nd: YAG. *Quantum Electronics, IEEE Journal of* **1971,** *7* (4), 153-159.

14. Dong, C. H.; van Veggel, F. C. J. M., Cation Exchange in Lanthanide Fluoride Nanoparticles. *ACS Nano* **2009,** *3* (1), 123-130.

15. Dong, C.; Korinek, A.; Blasiak, B.; Tomanek, B.; van Veggel, F. C. J. M., Cation Exchange: A Facile Method to Make $NaYF_4$:Yb,Tm-$NaGdF_4$ Core–Shell Nanoparticles with a Thin, Tunable, and Uniform Shell. *Chemistry of Materials* **2012,** *24* (7), 1297-1305.

16. Johnson, N. J. J.; van Veggel, F. C. J. M., Lanthanide-Based Heteroepitaxial Core-Shell Nanostructures: Compressive versus Tensile Strain Asymmetry. *ACS Nano* **2014,** *8* (10), 10517-10527.

17. (a) Matczuk, M.; Anecka, K.; Scaletti, F.; Messori, L.; Keppler, B. K.; Timerbaev, A. R.; Jarosz, M., Speciation of Metal-Based Nanomaterials in Human Serum Characterized by Capillary Electrophoresis Coupled to ICP-MS: A Case Study of Gold Nanoparticles. *Metallomics* **2015,** *7* (9), 1364-1370; (b) Colavita, E.; Decrescenzi, M.; Papagno, L.; Scarmozzino, R.; Caputi, L. S.; Rosei, R.; Tosatti, E., Single-Particle and Collective Excitations in Ferromagnetic Iron From Electron-Energy-Loss Spectroscopy *Physical Review B* **1982,** *25* (4), 2490-2502; (c) Matassoni, L.; Pratesi, G.; Centioli, D.; Cadoni, F.; Lucarelli, F.; Nava, S.; Malesani, P., Saharan Dust Contribution to PM_{10}, $PM_{2.5}$ and PM_1 in Urban and Suburban Areas of Rome: A Comparison Between Single-Particle SEM-EDS Analysis and Whole-Sample PIXE Analysis. *Journal of Environmental Monitoring* **2011,** *13* (3), 732-742.

18. Auffan, M.; Rose, J.; Bottero, J. Y.; Lowry, G. V.; Jolivet, J. P.; Wiesner, M. R., Towards a Definition of Inorganic Nanoparticles from an Environmental, Health and Safety Perspective. *Nature Nanotechnology* **2009,** *4* (10), 634-641.

19. Horikoshi, S.; Serpone, N., *Introduction to Nanoparticles*. 2013.

20. Nagarajan, R., Nanoparticles: Building Blocks for Nanotechnology. *Nanoparticles: Synthesis, Stabilization, Passivation, and Functionalization* **2008,** *996*, 2-14.

21. (a) Heiligtag, F. J.; Niederberger, M., The Fascinating World of Nanoparticle Research. *Mater. Today* **2013,** *16* (7-8), 262-271; (b) Lead, J. R.; Wilkinson, K. J., Aquatic Colloids and Nanoparticles: Current Knowledge and Future Trends. *Environmental Chemistry* **2006,** *3* (3), 159-171; (c) Buzea, C.; Pacheco, I. I.; Robbie, K., Nanomaterials and Nanoparticles: Sources and Toxicity. *Biointerphases* **2007,** *2* (4), MR17-MR71.

22. Jin, R. C.; Cao, Y. W.; Mirkin, C. A.; Kelly, K. L.; Schatz, G. C.; Zheng, J. G., Photoinduced Conversion of Silver Nanospheres to Nanoprisms. *Science* **2001,** *294* (5548), 1901-1903.

23. Faraday, M., The Bakerian Lecture: Experimental Relations of Gold (and Other Metals) to Light. *Philosophical Transactions of the Royal Society of London* **1857,** *147*, 145-181.

24. (a) Kalyanasundaram, K.; Borgarello, E.; Duonghong, D.; Gratzel, M., Cleavage of Water by Visible-Light Irradiation of Colloidal CdS Solutions - Inhibition of Photocorrosion by RuO_2. *Angewandte Chemie-International Edition in English* **1981,** *20* (11), 987-988; (b) Henglein, A., Photo-Degradation and Fluorescence of Colloidal-Cadmium Sulfide in Aqueous-Solution. *Berichte der Bunsengesellschaft für Physikalische Chemie* **1982,** *86* (4), 301-305.

25. Rossetti, R.; Ellison, J. L.; Gibson, J. M.; Brus, L. E., Size Effects in the Excited Electronic States of Small Colloidal CdS Crystallites. *Journal of Chemical Physics* **1984,** *80* (9), 4464-4469.

26. (a) Burda, C.; Chen, X. B.; Narayanan, R.; El-Sayed, M. A., Chemistry and Properties of Nanocrystals of Different Shapes. *Chemical Reviews* **2005,** *105* (4), 1025-1102; (b) Alivisatos, A. P., Perspectives on the Physical Chemistry of Semiconductor Nanocrystals. *Journal of Physical Chemistry* **1996,** *100* (31), 13226-13239; (c) Henglein, A., Small-Particle Research - Physicochemical Properties of Extremely Small Colloidal Metal and Semiconductor Particles. *Chemical Reviews* **1989,** *89* (8), 1861-1873.

27. Chen, X.; Liu, Y.; Tu, D., *Lanthanide-Doped Luminescent Nanomaterials*. Springer: 2014.

28. Menyuk, N.; Dwight, K.; Pierce, J. W., $NaYF_4$: Yb,Er — An Efficient Upconversion Phosphor. *Applied Physics Letters* **1972,** *21* (4), 159-161.

29. Mai, H. X.; Zhang, Y. W.; Si, R.; Yan, Z. G.; Sun, L. D.; You, L. P.; Yan, C. H., High-Quality Sodium Rare-Earth Fluoride Nanocrystals: Controlled Synthesis and Optical Properties. *Journal of the American Chemical Society* **2006,** *128* (19), 6426-6436.

30. Boyer, J. C.; Cuccia, L. A.; Capobianco, J. A., Synthesis of Colloidal Upconverting $NaYF_4$: Er^{3+}/Yb^{3+} and Tm^{3+}/Yb^{3+} Monodisperse Nanocrystals. *Nano Letters* **2007,** *7* (3), 847-852.

31. Hecht, J., Short History of Laser Development. *Optical Engineering* **2010,** *49* (9).

32. Gross, A. J.; Herrmann, T. R. W., History of Lasers. *World Journal of Urology* **2007,** *25* (3), 217-220.

33. Paschotta, R., *Field Guide to Lasers*. SPIE Press: 2008; Vol. 12.

34. Weber, R.; Neuenschwander, B.; Weber, H. P., Thermal Effects in Solid-State Laser Materials. *Optical Materials* **1999,** *11* (2-3), 245-254.

35. Stouwdam, J. W.; van Veggel, F. C. J. M., Near-Infrared Emission of Redispersible Er^{3+}, Nd^{3+}, and Ho^{3+} Doped LaF_3 Nanoparticles. *Nano Letters* **2002,** *2* (7), 733-737.

36. Bensalah, A.; Mortier, M.; Patriarche, G.; Gredin, P.; Vivien, D., Synthesis and Optical Characterizations of Undoped and Rare-Earth-Doped CaF_2 Nanoparticles. *Journal of Solid State Chemistry* **2006,** *179* (8), 2636-2644.

37. Grzyb, T.; Lis, S., Structural and Spectroscopic Properties of LaOF:Eu^{3+} Nanocrystals Prepared by the Sol-Gel Pechini Method. *Inorganic Chemistry* **2011,** *50* (17), 8112-8120.

38. Blood, P., *Quantum Confined Laser Devices: Optical Gain and Recombination in Semiconductors*. OUP Oxford: 2015.

39. (a) Liu, X.; Chi, Y.; Dong, G.; Wu, E.; Qiao, Y.; Zeng, H.; Qiu, J., Optical Gain at 1550 nm from Colloidal Solution of Er^{3+}-Yb^{3+} Codoped $NaYF_4$ Nanocubes. *Optics Express* **2009,** *17* (7), 5885-5890; (b) Xu, L.; Zhang, S. Y.; Xu, J. Q., Optical Amplification in $NaYF_4$:Nd Nanoparticle Dispersed Solution with Gain. *Laser Physics Letters* **2010,** *7* (4), 303-306.

40. Tzuk, Y.; Goren, C.; Raanan, D.; Strum, G., Nanoparticle Dispersion Laser. *Optics Letters* **2012,** *37* (5), 939-941.

41. Tzuk, Y.; Goren, C.; Sturm, G.; Greenblatt, J.; Raanan, D., Flashlamp-Pumped Nanoparticle Dispersion Laser. *Applied Optics* **2015,** *54* (5), 1157-1160.

42. Stręk, W.; Szafrański, C.; Łukowiak, E.; Mazurak, Z.; Jeżowska-Trzebiatowska, B., Fluorescence Quenching in Neodymium Pentaphosphate. *Physica Status Solidi (a)* **1977,** *41* (2), 547-553.

43. Li, Z.; Zhang, Y., An Efficient and User-Friendly Method for the Synthesis of Hexagonal-Phase $NaYF_4$:Yb, Er/Tm Nanocrystals with Controllable Shape and Upconversion Fluorescence. *Nanotechnology* **2008,** *19* (34), 345606.

44. (a) Langford, J. I.; Wilson, A. J. C., Scherrer After Sixty Years: A Survey and Some New Results in the Determination of Crystallite Size. *Journal of Applied Crystallography* **1978,** *11* (2), 102-113; (b) Monshi, A.; Foroughi, M. R.; Monshi, M. R., Modified Scherrer Equation to Estimate More Accurately Nano-Crystallite Size Using XRD. *World Journal of Nano Science and Engineering* **2012,** *2* (03), 154.

45. Dong, A. G.; Ye, X. C.; Chen, J.; Kang, Y. J.; Gordon, T.; Kikkawa, J. M.; Murray, C. B., A Generalized Ligand-Exchange Strategy Enabling Sequential Surface Functionalization of Colloidal Nanocrystals. *Journal of the American Chemical Society* **2011,** *133* (4), 998-1006.

46. Derer, A.; Deloch, L.; Rubner, Y.; Fietkau, R.; Frey, B.; Gaipl, U. S., Radio-Immunotherapy-Induced Immunogenic Cancer Cells as Basis for Induction of Systemic Anti-Tumor Immune Responses - Pre-Clinical Evidence and Ongoing Clinical Applications. *Frontiers in Immunology* **2015,** *6*.

47. (a) Deutsch, I.; Zelefsky, M. J.; Zhang, Z. G.; Mo, Q. X.; Zaider, M.; Cohen, G.; Cahlon, O.; Yamada, Y., Comparison of PSA Relapse-Free Survival in Patients Treated with Ultra-High-Dose IMRT versus Combination HDR Brachytherapy and IMRT. *Brachytherapy* **2010,** *9* (4), 313-318; (b) Seiwert, T. Y.; Salama, J. K.; Vokes, E. E., The Chemoradiation Paradigm in Head and Neck Cancer. *Nature Clinical Practice Oncology* **2007,** *4* (3), 156-171.

48. Baskar, R.; Dai, J.; Wenlong, N.; Yeo, R.; Yeoh, K.-W., Biological Response of Cancer Cells to Radiation Treatment. *Frontiers in molecular biosciences* **2014,** *1*, 24-24.

49. Patient's Guide to Prostate Cancer: Treatments. http://www.ucsfhealth.org/education/patients_guide_to_prostate_cancer/treatments/ (accessed September 21, 2015).

50. Guedea, F., Recent Developments in Brachytherapy. *Reports of Practical Oncology and Radiotherapy* **2011,** *16* (6), 203.

51. (a) Gao, M.; Wang, J. Z.; Nag, S.; Gupta, N., Effects of Seed Migration on Post-Implant Dosimetry of Prostate Brachytherapy. *Medical Physics* **2007,** *34* (2), 471-480; (b) Fuller, D. B.; Koziol, J. A.; Feng, A. C., Prostate Brachytherapy Seed Migration and

Dosimetry: Analysis of Stranded Sources and Other Potential Predictive Factors. *Brachytherapy* **2004,** *3* (1), 10-19.

52. Waterman, F. M.; Yue, N.; Corn, B. W.; Dicker, A. P., Edema Associated with I-125 or Pd-103 Prostate Brachytherapy and its Impact on Post-Implant Dosimetry: An Analysis Based on Serial CT Acquisition. *International Journal of Radiation Oncology Biology Physics* **1998,** *41* (5), 1069-1077.

53. Prostate Cancer Treatment Guide. http://www.prostate-cancer.com/brachytherapy/treatment-description/prostate-brachytherapy.html (accessed September 21, 2015).

54. Jani, A. B.; Feinstein, J. M.; Pasciak, R.; Krengel, S.; Weichselbaum, R. R., Role of External Beam Radiotherapy with Low-Dose-Rate Brachytherapy in Treatment of Prostate Cancer. *Urology* **2006,** *67* (5), 1007-1011.

55. Esposito, C.; Crema, A.; Ponzetto, A.; Murtas, G.; Carloni, G., Multifunctional Anti-Cancer Nano-Platforms are Moving to Clinical Trials. *Current Drug Metabolism* **2013,** *14* (5), 583-604.

56. (a) Hossain, M. K.; Cho, H.-Y.; Kim, K.-J.; Choi, J.-W., In-Situ Monitoring of Doxorubicin Release from Biohybrid Nanoparticles Modified with Antibody and Cell-Penetrating Peptides in Breast Cancer Cells Using Surface-Enhanced Raman Spectroscopy. *Biosensors & Bioelectronics* **2015,** *71*, 300-305; (b) Narayanan, N.; Karunakaran, V.; Paul, W.; Venugopal, K.; Sujathan, K.; Maiti, K. K., Aggregation Induced Raman Scattering of Squaraine Dye: Implementation in Diagnosis of Cervical Cancer Dysplasia by SERS Imaging. *Biosensors & Bioelectronics* **2015,** *70*, 145-152.

57. Paik, T.; Chacko, A. M.; Mikitsh, J. L.; Friedberg, J. S.; Pryma, D. A.; Murray, C. B., Shape-Controlled Synthesis of Isotopic Yttrium-90-Labeled Rare Earth Fluoride Nanocrystals for Multimodal Imaging. *ACS Nano* **2015,** *9* (9), 8718-8728.

58. Wester, D. W.; Steele, R. T.; Rinehart, D. E.; DesChane, J. R.; Carson, K. J.; Rapko, B. M.; Tenforde, T. S., Large-Scale Purification of ^{90}Sr From Nuclear Waste Materials for Production of ^{90}Y, a Therapeutic Medical Radioisotope. *Applied Radiation and Isotopes* **2003,** *59* (1), 35-41.

59. Banerjee, S.; Pillai, M.; Knapp, F., Lutetium-177 Therapeutic Radiopharmaceuticals: Linking Chemistry, Radiochemistry, and Practical Applications. *Chemical reviews* **2015,** *115* (8), 2934-2974.

60. (a) Wu, H.; Engelhard, M. H.; Wang, J.; Fisher, D. R.; Lin, Y. H., Synthesis of Lutetium Phosphate-Apoferritin Core-Shell Nanoparticles for Potential Applications in Radioimmunoimaging and Radioimmunotherapy of Cancers. *Journal of Materials*

Chemistry **2008,** *18* (15), 1779-1783; (b) Radović, M.; Vranješ-Đurić, S.; Nikolić, N.; Janković, D.; Goya, G. F.; Torres, T. E.; Calatayud, M. P.; Bruvera, I. J.; Ibarra, M. R.; Spasojević, V.; Jančare, B.; Antić, B., Development and Evaluation of ^{90}Y-Labeled Albumin Microspheres Loaded with Magnetite Nanoparticles for Possible Applications in Cancer Therapy. *Journal of Materials Chemistry* **2012,** *22* (45), 24017-24025.

61. Son, D. H.; Hughes, S. M.; Yin, Y. D.; Alivisatos, A. P., Cation Exchange Reactions in Ionic Nanocrystals. *Science* **2004,** *306* (5698), 1009-1012.

62. Zhang, D. D.; Wong, A. B.; Yu, Y.; Brittman, S.; Sun, J. W.; Fu, A.; Beberwyck, B.; Alivisatos, A. P.; Yang, P. D., Phase-Selective Cation-Exchange Chemistry in Sulfide Nanowire Systems. *Journal of the American Chemical Society* **2014,** *136* (50), 17430-17433.

63. (a) Jeong, U. Y.; Xia, Y. N., Synthesis and Crystallization of Monodisperse Spherical Colloids of Amorphous Selenium. *Advanced Materials* **2005,** *17* (1), 102-+; (b) Camargo, P. H. C.; Lee, Y. H.; Jeong, U.; Zou, Z. Q.; Xia, Y. N., Cation Exchange: A Simple and Versatile Route to Inorganic Colloidal Spheres with the Same Size but Different Compositions and Properties. *Langmuir* **2007,** *23* (6), 2985-2992.

64. Pietryga, J. M.; Werder, D. J.; Williams, D. J.; Casson, J. L.; Schaller, R. D.; Klimov, V. I.; Hollingsworth, J. A., Utilizing the Lability of Lead Selenide to Produce Heterostructured Nanocrystals with Bright, Stable Infrared Emission. *Journal of the American Chemical Society* **2008,** *130* (14), 4879-4885.

65. (a) Anderson, R. B.; Smith, S. J.; May, P. S.; Berry, M. T., Revisiting the NIR-to-Visible Upconversion Mechanism in β-$NaYF_4$:Yb^{3+},Er^{3+}. *Journal of Physical Chemistry Letters* **2014,** *5* (1), 36-42; (b) Berry, M. T.; May, P. S., Disputed Mechanism for NIR-to-Red Upconversion Luminescence in $NaYF_4$:Yb^{3+},Er^{3+}. *Journal of Physical Chemistry A* **2015,** *119* (38), 9805-9811.

66. (a) Yi, G. S.; Chow, G. M., Synthesis of Hexagonal-Phase $NaYF_4$: Yb,Er and NaYF4 : Yb,Tm Nanocrystals with Efficient Up-Conversion Fluorescence. *Advanced Functional Materials* **2006,** *16* (18), 2324-2329; (b) Wang, F.; Han, Y.; Lim, C. S.; Lu, Y. H.; Wang, J.; Xu, J.; Chen, H. Y.; Zhang, C.; Hong, M. H.; Liu, X. G., Simultaneous Phase and Size Control of Upconversion Nanocrystals Through Lanthanide Doping. *Nature* **2010,** *463* (7284), 1061-1065; (c) Johnson, N. J. J.; Korinek, A.; Dong, C. H.; van Veggel, F. C. J. M., Self-Focusing by Ostwald Ripening: A Strategy for Layer-by-Layer Epitaxial Growth on Upconverting Nanocrystals. *Journal of the American Chemical Society* **2012,** *134* (27), 11068-11071.

67. Ishimaru, M.; Dickerson, R. M.; Sickafus, K. E., Scanning Ttransmission Electron Microscopy-Energy Dispersive X-ray/Electron Energy Loss Spectroscopy Studies on

SiC-on-Insulator Structures. *Journal of the Electrochemical Society* **2000,** *147* (5), 1979-1981.

68. Pornwilard, M. M.; Weiskirchen, R.; Gassler, N.; Bosserhoff, A. K.; Becker, J. S., Novel Bioimaging Techniques of Metals by Laser Ablation Inductively Coupled Plasma Mass Spectrometry for Diagnosis Of Fibrotic and Cirrhotic Liver Disorders. *PLoS One* **2013,** *8* (3), 12.

69. von Harrach, H.; Klenov, D.; Freitag, B.; Schlossmacher, P.; Collins, P.; Fraser, H., Comparison of the Detection Limits of EDS and EELS in S/TEM. *Microscopy and Microanalysis* **2010,** *16* (SupplementS2), 1312-1313.

70. Müllejans, H.; Bruley, J., Electron Energy-Loss Spectroscopy (EELS) - Comparison with X-ray Analysis. *Journal De Physique IV* **1993,** *3* (C7), 2083-2092.

71. Vatter, I. A.; Titchmarsh, J. M., Measurement of Grain-Boundary Segregation by STEM-EDX Analysis. *Ultramicroscopy* **1989,** *28* (1-4), 236-239.

72. Egerton, R. F.; Li, P.; Malac, M., Radiation Damage in the TEM and SEM. *Micron* **2004,** *35* (6), 399-409.

73. Soong, C.; Woo, P.; Hoyle, D., Contamination Cleaning of TEM/SEM Samples with the ZONE Cleaner. *Microscopy Today* **2012,** *20* (06), 44-48.

74. Egerton, R. F.; Crozier, P. A.; Rice, P., Electron Energy-Loss Spectroscopy and Chemical-Change. *Ultramicroscopy* **1987,** *23* (3-4), 305-312.

75. Henderson, R.; Glaeser, R. M., Quantitative-Analysis of Image-Contrast in Electron-Micrographs of Beam-Sensitive Crystals. *Ultramicroscopy* **1985,** *16* (2), 139-150.

76. Abel, K. A.; Boyer, J.-C.; Andrei, C. M.; van Veggel, F. C. J. M., Analysis of the Shell Thickness Distribution on $NaYF_4$/$NaGdF_4$ Core/Shell Nanocrystals by EELS and EDS. *Journal of Physical Chemistry Letters* **2011,** *2* (3), 185-189.

77. Warwick, T.; Franck, K.; Kortright, J. B.; Meigs, G.; Moronne, M.; Myneni, S.; Rotenberg, E.; Seal, S.; Steele, W. F.; Ade, H.; Garcia, A.; Cerasari, S.; Delinger, J.; Hayakawa, S.; Hitchcock, A. P.; Tyliszczak, T.; Kikuma, J.; Rightor, E. G.; Shin, H. J.; Tonner, B. P., A scanning transmission X-ray microscope for materials science spectromicroscopy at the advanced light source. *Review of Scientific Instruments* **1998,** *69* (8), 2964-2973.

78. Rightor, E. G.; Hitchcock, A. P.; Ade, H.; Leapman, R. D.; Urquhart, S. G.; Smith, A. P.; Mitchell, G.; Fischer, D.; Shin, H. J.; Warwick, T., Spectromicroscopy of Poly(ethylene terephthalate): Comparison of Spectra and Radiation Damage Rates in X-ray Absorption and Electron Energy Loss. *Journal of Physical Chemistry B* **1997,** *101* (11), 1950-1960.

79. Calvin, S., *XAFS for Everyone*. CRC Press: 2013; p 427.

80. (a) Filez, M.; Poelman, H.; Ramachandran, R. K.; Dendooven, J.; Devloo-Casier, K.; Fonda, E.; Detavernier, C.; Marin, G. B., In-Situ XAS and XRF Study of Nanoparticle Nucleation During O_3-Based Pt Deposition. *Catalysis Today* **2014,** *229*, 2-13; (b) Boita, J.; Castegnaro, M. V.; Alves, M. D. M.; Morais, J., A Dispenser-Reactor Apparatus Applied for In-Situ XAS Monitoring of Pt Nanoparticle Formation. *Journal of Synchrotron Radiation* **2015,** *22*, 736-744; (c) Meneses, C. T.; Flores, W. H.; Sotero, A. P.; Tamura, E.; Garcia, F.; Sasaki, J. M., In-Situ System for X-ray Absorption Spectroscopy Experiments to Investigate Nanoparticle Crystallization. *Journal of Synchrotron Radiation* **2006,** *13*, 468-470.

81. Chakroune, N.; Viau, G.; Ammar, S.; Poul, L.; Veautier, D.; Chehimi, M. M.; Mangeney, C.; Villain, F.; Fiévet, F., Acetate- and Thiol-Capped Monodisperse Ruthenium Nanoparticles: XPS, XAS, and HRTEM Studies. *Langmuir* **2005,** *21* (15), 6788-6796.

82. Vo, K. D. N.; Guillon, E.; Dupont, L.; Kowandy, C.; Coqueret, X., Influence of Au(III) Interactions with Chitosan on Gold Nanoparticle Formation. *Journal of Physical Chemistry C* **2014,** *118* (8), 4465-4474.

83. Brandt, F.; Schäfer, T.; Claret, F.; Bosbach, D., Heterogeneous Formation of Ferric Oxide Nanoparticles on Chlorite Surfaces Studied by X-ray Absorption Spectromicroscopy (STXM). *Chemical Geology* **2012,** *329*, 42-52.

84. Li, M.; Gao, J.; Bai, L. L.; Pu, A. W.; Liu, J. Y.; Zhao, G. Q.; Sun, X. H.; Zhong, J., Probing Carbon Coatings on Nanoparticle Decorated Carbon Nanotubes by Scanning Transmission X-ray Microscopy. *Applied Surface Science* **2013,** *285*, 874-878.

85. (a) Oakes, M.; Weber, R. J.; Lai, B.; Russell, A.; Ingall, E. D., Characterization of Iron Speciation in Urban and Rural Single Particles Using XANES Spectroscopy and Micro X-ray Fluorescence Measurements: Investigating the Relationship Between Speciation and Fractional Iron Solubility. *Atmospheric Chemistry and Physics* **2012,** *12* (2), 745-756; (b) Rodríguez, A. F.; Kleibert, A.; Bansmann, J.; Nolting, F., Probing Single Magnetic Nanoparticles by Polarization-Dependent Soft X-ray Absorption Spectromicroscopy. *Journal of Physics D-Applied Physics* **2010,** *43* (47), 8; (c) Vereda, F.; de Vicente, J.; Morales, M. D. P.; Rull, F.; Hidalgo-Álvarez, R., Synthesis and Characterization of Single-Domain Monocrystalline Magnetite Particles by Oxidative

Aging of $Fe(OH)_2$. *Journal of Physical Chemistry C* **2008,** *112* (15), 5843-5849; (d) Vernooij, M. G. C.; Mohr, M.; Tzvetkov, G.; Zelenay, V.; Huthwelker, T.; Kaegi, R.; Gehrig, R.; Grobéty, B., On Source Identification and Alteration of Single Diesel and Wood Smoke Soot Particles in the Atmosphere; An X-Ray Microspectroscopy Study. *Environmental Science & Technology* **2009,** *43* (14), 5339-5344.

86. Liang, Z. Q.; Cui, Y.; Zhao, S. L.; Tian, L. J.; Zhang, J. J.; Xu, Z., The Enhanced Upconversion Fluorescence and Almost Unchanged Particle Size of β-$NaYF_4$:Yb^{3+}, Er^{3+} Nanoparticles by Codoping with K^+ Ions. *Journal of Alloys and Compounds* **2014,** *610*, 432-437.